inorganics

MDPI

Review

Beyond Reinforcement Selection: Interface-Driven Process–Structure–Property Relationships in Powder-Metallurgy Metal Matrix Composites and Functional Coatings

Cevher Kürşat Macit [1,*], Merve Ayık [2], Bünyamin Aksakal [1], Faruk Karaca [3] and Yakup Say [4]

[1] School of Aviation, Aircraft Airframe-Engine Maintenance, Firat University, 23119 Elazig, Turkey; baksakal@firat.edu.tr
[2] Aisin Automotive Parts Industry and Trade Inc., 34953 Tuzla, İstanbul, Turkey; mervehorlu@gmail.com
[3] Department of Mechanical Engineering, Faculty of Technology, Firat University, 23119 Elazig, Turkey; fkaraca@firat.edu.tr
[4] Rare Earth Elements Application and Research Center, Munzur University, 62000 Tunceli, Turkey; yakupsay@munzur.edu.tr
* Correspondence: ckmacit@firat.edu.tr

Abstract

Powder metallurgy (PM) and surface engineering offer complementary routes to multifunctional metal matrix composites (MMCs), but constituent properties alone do not determine component performance. Reinforcement geometry, consolidation, reaction-layer development, and interfacial connectivity regulate the transfer of stress, heat, and charge while controlling the initiation of wear and environmental damage. This review integrates Al-, Cu-, Mg-, Ti-, Fe/316L-, and Ni-based systems within an interface-centered process–structure–property framework. Comparative analysis combines quantitative interface measurements with mechanical, tribological, thermal, electrical, and corrosion data, retaining the processing state and test conditions associated with each result. Within-study hardness ratios reach 1.69 for B_4C/Cu and 2.10 for graphene-oxide/Cu, while an AZ91D–Ni/graphene series exhibits a specific-wear-rate ratio of 0.739 relative to its corresponding control. These benchmarks reveal distinct routes to improved performance rather than a common ranking of reinforcements. Direct nanotube pull-out, in situ dislocation observations, and thermal-boundary measurements connect nanoscale interactions to macroscopic response. Hierarchical Al and Mg architectures and network-reinforced Ti demonstrate how spatial design can balance strengthening and deformation; fatigue and fracture evidence further delineates the limits of selection based on hardness or tensile strength. Coating comparisons relate deposition conditions to retained phases, cohesion, substrate support, connected defects, and protection during service. The optimum reinforcement window consequently emerges as a matrix-, geometry-, processing-, and application-dependent region. The synthesis establishes quantitative comparison principles and engineering criteria for interfaces that retain their mechanical and functional roles under coupled loading and environmental exposure.

Keywords: powder metallurgy; metal matrix composites; hybrid reinforcement; tribology; microstructure; functional coatings; high-velocity oxy-fuel spraying; interface engineering; process–structure–property relationships

Academic Editors: Chunyang Xu, Xianhua Huan and Huanhuan Liu

Received: 19 October 2026
Revised: 8 November 2026
Accepted: 27 November 2026
Published: 28 November 2026

Copyright: © 2026 by the authors. Licensee MDPI, Basel, Switzerland. This article is an open access article distributed under the terms and conditions of the Creative Commons Attribution (CC BY) license.

1. Introduction

Powder metallurgy (PM) offers a versatile route to metal matrix composites (MMCs) through the controlled combination of powder preparation, reinforcement dispersion, compaction, and consolidation. Its design space extends beyond choosing a constituent with high intrinsic hardness or conductivity. The processing history establishes metal–metal contacts, matrix continuity, residual porosity, and the physical and chemical state of matrix–reinforcement interfaces. These intermediate features determine whether a nominal addition becomes an effective load-bearing or functional phase [1–5]. The governing sequence extends from powder processing to interface formation, microstructural evolution, and service response. Particle surface condition regulates packing and oxide disruption, milling controls dispersion and reinforcement integrity, and pressure–temperature–time history governs densification and reaction. Composites of identical nominal composition can consequently develop different properties, whereas chemically different reinforcements can produce similar hardness through distinct combinations of matrix refinement, local constraint, and pore elimination [6–8]. Common hard phases include silicon carbide (SiC), alumina (Al_2O_3), boron carbide (B_4C), titanium carbide (TiC), titanium diboride (TiB_2), tungsten carbide (WC), and zirconia (ZrO_2). Graphite, graphene, graphene oxide (GO), reduced graphene oxide (rGO), and carbon nanotubes (CNTs) introduce additional lubrication and transport possibilities. Hexagonal boron nitride (hBN) is a lamellar ceramic solid lubricant, not a carbonaceous reinforcement. Hybrid systems combine functions, but their benefit depends on the spatial arrangement and integration of the individual phases [1,6,9,10]. Matrix selection defines the engineering constraint. Aluminum systems emphasize specific mechanical performance; Cu systems must retain useful thermal and electrical transport; Mg introduces stringent oxidation and corrosion requirements; and Ti-, Fe/316L-, and Ni-based systems emphasize reaction control, damage tolerance, or temperature-dependent stability. The same percentage hardness gain therefore has a different practical meaning in each matrix [3,5,6,11].

Strengthening mechanisms also require different evidence. Load transfer requires effective stress transmission; grain-boundary strengthening requires a measured matrix grain-size change; and thermal-expansion mismatch requires dislocations that are generated and retained after processing. Orowan bypassing is relevant to suitably spaced, nonshearable nanoscale obstacles and should not be assigned as the dominant mechanism for ordinary micrometer-scale particles without an appropriate magnitude estimate [8,12].

Tribology introduces an evolving contact interface. A tribofilm is a mechanically or chemically transformed layer generated on a worn surface; a transfer film is material deposited from one contacting body on the counterface. Their formation can be coupled but cannot be inferred interchangeably from a reduced coefficient of friction (COF). Friction, material loss, debris, and the condition of both contacting surfaces must be considered together [13,14].

Surface engineering is complementary when the required modification is localized. High-velocity oxy-fuel (HVOF) spraying, physical vapor deposition (PVD), chemical vapor deposition (CVD), electrophoretic deposition (EPD), sol–gel processing, and laser cladding differ in functional depth, thermal exposure, and interface formation. Comparison with bulk MMCs requires a common focus on adhesion, substrate support, current/heat paths, and the location of the dominant failure mechanism [15–21].

The literature has established detailed accounts of reinforcement families, fabrication technologies, and interfacial modification [1,6,8,9,11,22,23]. Their integration across structural and functional requirements remains essential because a processing intervention can improve one response while compromising another. The present review connects measured interface characteristics to application-specific selection, combining within-study normalization with cross-matrix analysis of strengthening, transport, corrosion, and

https://doi.org/10.3390/inorganics14120303

coating failure. Its central contribution is a common interpretation of bulk and surface architectures in terms of the interfaces that transmit load and transport fluxes and the defects that interrupt these functions.

Apparently conflicting results can expose different constraints. Increasing reinforcement may raise hardness while reducing compressibility, or improve dry wear while worsening corrosion. Such results need not be contradictory because the responses probe different mechanisms and environments. Separating these property-dependent trade-offs from genuinely incompatible observations is central to the synthesis [24–28].

Scanning electron microscopy (SEM), energy-dispersive X-ray spectroscopy (EDS), X-ray diffraction (XRD), density, mechanical testing, and functional characterization provide complementary evidence. Higher-resolution techniques are needed when an explanation depends on reaction-layer dimensions, local chemistry, crystallography, or an interface-specific mechanical or transport parameter. A morphological association is therefore distinguished from direct demonstration of its proposed mechanism [8,29–31].

The interface-centered viewpoint becomes particularly useful when the same intervention affects several functions in opposite directions. Increasing contact area may improve mechanical constraint while increasing thermal boundary scattering; an electrically conducting reinforcement may support current but also enlarge an electrochemically active cathodic network. Architectural control can sometimes reconcile these objectives without simply reducing reinforcement content. Network-reinforced Ti and chemically modified graphene–metal boundaries provide complementary examples of spatial and chemical design. They motivate comparison at the level of measured interface descriptors and service requirements, rather than a catalogue of nominal formulations [30,32,33].

The analysis addresses five connected questions: how processing establishes the operative interface; which microstructural descriptors explain the measured response; how reinforcement geometry and matrix chemistry shift the preferred composition; how mechanical gains interact with transport and environmental performance; and when a surface architecture is more effective than bulk modification. Processing and matrix-specific behavior are examined first, followed by interface engineering, comparative properties, and mechanism-resolving characterization. The final sections integrate coating selection, component-level requirements, and research priorities.

2. Scope, Literature Selection, and Comparative Framework

The review examines PM-derived MMCs and surface-engineered metallic systems through a critical synthesis of experimental process–structure–property relationships. Coverage includes Al-, Cu-, Mg-, Ti-, Fe/316L-, and Ni-based matrices, ceramic and carbonaceous reinforcements, hybrid architectures, and the principal consolidation and coating technologies. Foundational studies establish the physical basis of sintering, strengthening, friction, and interface transport, while contemporary investigations extend the analysis to hierarchical architectures and multifunctional performance.

Literature selection follows a question-led, thematic approach. Journal articles were identified using combinations of matrix and reinforcement names with processing and performance terms, and the reference lists of pertinent publications were examined for complementary primary studies. The publication span extends from foundational work in 1953 to material-specific studies published in 2026. Emphasis is placed on studies that relate a defined processing or architectural change to characterized microstructure and measured properties.

The principal keyword groups combined “powder metallurgy”, “hot pressing”, “spark plasma sintering”, and “interface” with matrix-specific terms and responses such as “particle size”, “fatigue”, “thermal conductivity”, and “corrosion”. Coating-related combinations included “HVOF”, “HVAF”, “electrophoretic deposition”, “cold spray”,

"adhesion", and "wear". High-velocity air-fuel (HVAF) spraying is distinguished from high-velocity oxy-fuel spraying because their particle thermal histories can lead to different retained phases and coating responses. The selected literature spans both direct interface experiments and studies linking bulk or coating properties to their processing histories.

Primary experimental studies provide the basis for material-specific numerical comparisons. Eligible studies identify the matrix, reinforcement, processing route, and measured response sufficiently to associate each property with a defined material state. Unreinforced matrices processed under comparable conditions and uncoated substrates provide the preferred reference states. Melt-processed materials are included selectively to clarify route-dependent behavior; stir-cast Al7075–B_4C and arc-induction-melted rGO/Cu are therefore treated as complementary fabrication systems rather than PM materials [34,35].

Comparison variables comprise matrix composition, reinforcement mass or volume fraction (wt.% or vol.%), particle dimensions and morphology, dispersion method, consolidation history, density, test configuration, and measurement uncertainty. Quantitative synthesis requires an identifiable connection between these variables and the reported endpoint. Studies with incomplete comparison parameters can still contribute to qualitative mechanistic analysis, but their numerical results are retained in their original experimental context. In the tables, NR indicates that a parameter is unavailable for the stated comparison.

Duplicate publications, unrelated material systems, and results without an identifiable material–property correspondence are excluded from numerical synthesis. Reviews and monographs support the discussion of underlying principles, whereas primary articles support experimental benchmarks. Selection across matrix families and coating routes is guided by distinct physical constraints, including oxidation-sensitive processing, reactive interfaces, conductive continuity, damage tolerance, and substrate-supported protection.

Three forms of evidence inform the interpretation. Direct measurements resolve the proposed descriptor or event, such as interface-sensitive strength, reaction-layer dimensions, or dislocation generation. Correlations establish concurrent changes in microstructure and properties, with their interpretation conditioned by other evolving variables. Mechanistic models connect these observations through physical relationships and identify the conditions under which an explanation remains applicable. This distinction allows quantitative conclusions to reflect the spatial resolution and specificity of the supporting experiment.

Property comparisons are organized by matrix state, fabrication route, and testing configuration. Hardness values retain the indentation scale and load; wear comparisons retain the loss metric, normal load, sliding distance and speed, counterface, and environment. Thermal and electrical results retain temperature and measurement direction, while corrosion comparisons retain exposure conditions and the measured electrochemical or degradation endpoint. Ratios relative to the corresponding processed reference express the magnitude of a change without suppressing these experimental distinctions.

Uncertainty is interpreted according to the experimental unit. Independently fabricated specimens, repeated wear tracks, and multiple indentations quantify different sources of variability. Standard deviation (SD), standard error (SE), and confidence interval (CI) are distinguished where their definitions are available. Within-study property ratios are used descriptively; inferential comparisons require compatible endpoints and independently supported uncertainty estimates.

The resulting comparisons emphasize physical transferability. A favorable response is related to the matrix, reinforcement architecture, interface state, and environment in

which it was observed. Differences in these conditions are used to explain divergent trends rather than averaged into a common material ranking. This approach preserves quantitative benchmarks while identifying the combinations of properties that govern engineering selection.

Table 1 summarizes the material coverage and the principal role of each evidence group. Controlled size and composition series establish processing sensitivity, direct interface experiments constrain mechanistic interpretation, and thermal, corrosion, fatigue, and coating studies connect microstructural design to the relevant operating requirement.

Table 1. Material coverage and principal experimental contributions to the comparative analysis. SPS: spark plasma sintering; HIP: hot isostatic pressing.

Material or Route	Representative Evidence	Comparison Role/Principal Constraint
Al/ceramic and carbon	PM size series; SPS and hybrid studies; casting comparator [8,10,27,28,34,36–42]. Size-dependent fatigue and high-fraction consolidation [43,44]. Hierarchical laminates and ceramic–carbon interlocking [45,46].	Geometry, consolidation, and phase state; hardness versus damage tolerance. Non-PM comparisons are identified explicitly.
Cu/ceramic and graphene-related	Fixed-loading PM, precursor, blending, aligned-network, and melt-route studies [11,13,14,23,24,35,47–54]. Direct boundary transport, Ni-decorated graphene, and diamond interlayers [33,55,56]. Microwave consolidation with coupled transport measurements [57].	Wear versus charge/heat transport; independent research groups and processing strategies.
Mg	Hot-pressed TiB_2/AZ91; semi-PM Mg/graphene; PM AZ92/SiC [5,25,26,58,59]. Independent SPS, graphene-chemistry, and biodegradable-material studies [60–64]. Reactive heterogeneous architecture [65].	Specific mechanical performance versus environment-sensitive durability.
Ti	HIP TiB architecture; carbon-fiber interface evolution; hot-corrosion study [3,29,66,67]. Designed TiB network architecture [32]. Tensile, fracture, and fatigue coupling [68].	Reaction extent, residual reinforcement geometry, and service temperature.
Fe/316L and Ni	PM B/Al_2O_3–316L; non-PM Fe–TiC comparator; carbon/Ni consolidation [69–71]. Polymer-derived steel reinforcement and chemically identified Ni tribofilms [72,73]. TiC–316L and temperature-dependent or high-pressure-torsion (HPT)-consolidated Ni systems [74–76].	Hard-phase distribution, damage tolerance, and lubricating-phase retention.
Coatings	Thermal spraying; PVD/CVD; EPD; sol–gel particle treatment; laser cladding [15–21,77–81]. HVOF/HVAF, Ti–Al–N evolution, GO barriers, laser cladding, and cold-spray contrasts [82–87]. Lightweight-substrate protection and quantified EPD growth [88,89].	Functional depth, adhesion/cohesion, substrate support, and processing exposure.
Methods and mechanism models	Sintering, dislocation bypass, thermal interface modeling, indentation [7,12,30,31,90–97]. Direct pull-out, in situ tensile, Raman, diffraction, and transport metrology [98–103]. In situ mismatch dislocations and carbide/diamond boundary conductance [104–106].	Measurement capability and model assumptions; not substitutes for material-specific experimental datasets.

3. Processing–Microstructure Relationships in PM-Derived MMCs

Powder processing transforms the initial particle population into a network of metallic contacts, reinforcing phases, pores, and interfaces. Mixing energy, contamination, thermal gradients, and heating/cooling history act together with nominal pressure and temperature. Figure 1 summarizes the connections between these variables and the resulting properties. The operative structural quantities are contact area, residual pore topology, grain structure, and the chemistry and continuity of the matrix–reinforcement boundary [4,7,90,91,96].

The strongest comparisons hold composition, route, or geometry constant while systematically varying another factor. Same-composition route studies, controlled composition series, and size-controlled reinforcement experiments separate processing sensitivity from chemistry and morphology more effectively than comparisons of unrelated best-performing specimens [27,37,53].

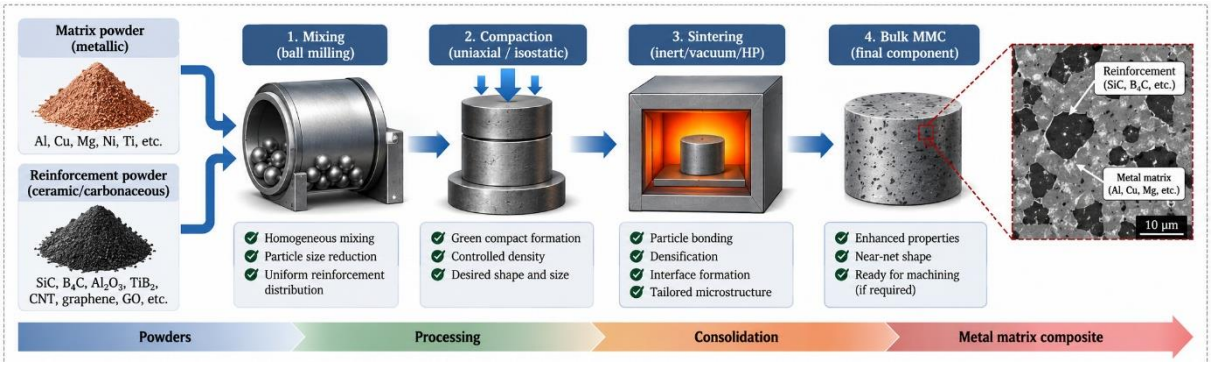

Figure 1. Conceptual process–structure–property framework for PM-derived MMCs, linking powder preparation and consolidation to interface formation, microstructural evolution, and engineering performance.

3.1. Powder Characteristics and Reinforcement Dispersion

Powder size distribution, shape, surface condition, and reinforcement geometry determine packing and the subsequent contact network. A primary particle diameter, an agglomerate diameter, a platelet thickness/lateral dimension, and a fiber length are different quantities. Reporting only "nanoscale" or "microscale" obscures the feature actually interacting with the matrix [7,8,27,97].

For an ideal monodisperse population of spherical particles, the interfacial area per unit composite volume is $A_v = 6f/d$, where f is reinforcement volume fraction and d is particle diameter. At fixed f, reducing d by one order of magnitude increases the geometric interface area tenfold. This simultaneously enlarges the potential load-transfer area and the amount of surface susceptible to contamination or reaction. The effective bonded area remains dependent on wetting, contact formation, and porosity. Platelets and fibers additionally require thickness, aspect ratio, and orientation to describe their contact architecture [12,30].

Mechanical alloying involves repeated deformation, cold welding, fracture, and rewelding. It can distribute reinforcement but can also introduce contamination, work hardening, oxidation, or reinforcement damage. Milling time, speed, ball-to-powder ratio, media, process-control agent, and atmosphere are therefore necessary comparison variables [7,97]. Wet blending, ultrasonication, and precursor-based synthesis offer alternative contact pathways, but their success is determined by the final structure rather than their process names [53,54].

Representative dispersion assessment should distinguish reinforcement-rich clusters from depleted matrix. Cluster fraction, nearest-neighbor spacing, and the distribution of

agglomerate dimensions describe different forms of heterogeneity. Varol and Canakci examined Al2024 with 0–20 wt.% B_4C and median particle diameters (d_{50}) of 5 and 49 μm, showing the coupled role of size, content, and milling history. Hardness increased over the tested fraction range while density decreased; an obligatory interior hardness optimum was not established [27].

For anisotropic reinforcements, one size parameter is insufficient. A platelet has a lateral dimension, thickness, and orientation distribution; a nanotube or whisker additionally has an embedded length and an aspect ratio. Milling can decrease cluster size and reinforcement length simultaneously. This creates a genuine trade-off: improved spatial uniformity may be accompanied by reduced stress-transfer length or interrupted conductive pathways. A useful powder specification therefore reports both the feedstock distribution and the retained post-processing geometry. The relevant comparison is the fraction of individually incorporated reinforcement and the distribution of matrix ligament widths, rather than an isolated representative particle image [7,38,40,100].

Particle geometry also influences the continuity of the metallic skeleton before sintering. Fine reinforcement distributed over large metal particles can form a nearly continuous interparticle layer even at a small overall mass fraction. Such coverage can promote homogeneous incorporation but may obstruct metal–metal neck formation when the coating is thick or poorly displaced during compaction. By contrast, reinforcement embedded within flattened metal particles is less exposed at particle boundaries but may experience substantial milling damage. These alternatives explain why nominally identical graphene or ceramic additions can show different density–strength relationships after dry milling, wet blending, or precursor-assisted processing [7,38,53,54].

Raman spectroscopy can track carbon structural changes, provided that excitation energy, fitting method, and defect regime are retained. The D-to-G intensity ratio is not a universal linear measure of damage: its calibration depends on excitation and on the stage of disorder. Cançado et al. established the excitation-energy dependence for point-defect quantification in graphene. Applied to MMC processing, this supports comparing like-for-like spectra before and after mixing/consolidation, alongside platelet dimensions and oxygen chemistry, rather than translating every increase in the D band directly into a proportional loss of reinforcement efficiency [101]. Figure 2 places these geometry and dispersion effects within the powder-processing sequence.

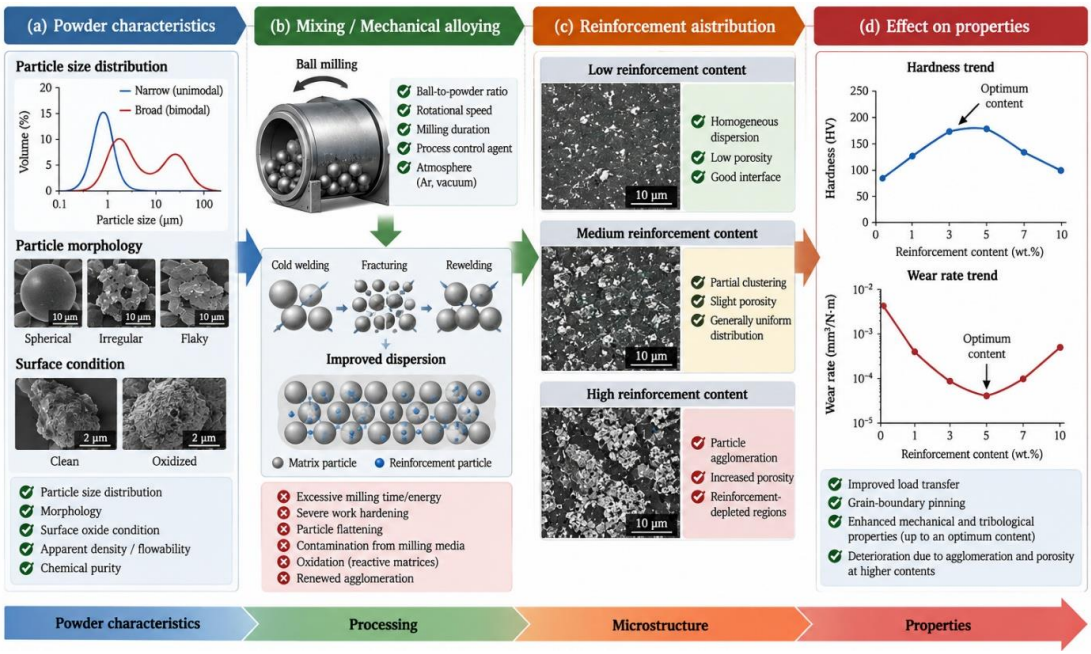

https://doi.org/10.3390/inorganics14120303

Figure 2. Schematic effects of powder characteristics and dispersion quality on reinforcement distribution, agglomeration, porosity, and property development. A homogeneous-looking field is a qualitative observation; representative sampling is needed for a quantitative dispersion claim.

3.2. Compaction Pressure, Green Density, and Porosity Evolution

Compaction develops a load-bearing green contact network, but the response depends on powder deformability, friction, size distribution, reinforcement shape, and die geometry. Hard particles can restrict metal deformation even when they later improve consolidated hardness. Green density and final relative density must therefore be evaluated separately [90–92].

The approximation $P \approx 1 - \varrho bulk/\varrho_{th}$ represents porosity only when final-phase changes and measurement assumptions are addressed. Open, connected, and isolated pores have different consequences for consolidation, fatigue, and fluid ingress. Pore topology therefore complements average density when compaction conditions are compared [27,90,91].

Chand et al. varied compaction from 200 to 800 MPa and sintering from 400 to 600 °C in Al6061 containing 2–8 wt.% B_4C plus 2 wt.% BN. Increased hard-phase content reduced compressibility and sinterability even though the highest tested pressure, temperature, and content produced the highest mechanical endpoints. Manufacturing ease and final performance are therefore distinct objectives [28].

Figure 3 connects the compact's starting condition to the subsequent sintering response. Its temperature coordinate emphasizes that improved green packing and thermally activated densification are related but distinct steps; pore closure, grain growth, and interface development must be interpreted together.

Compaction pressure and temperature influence different parts of the deformation response. Increasing pressure enlarges contact areas, whereas warm compaction can lower matrix flow resistance and alter particle rearrangement around rigid inclusions. Lin and Xiong examined TiC–316L composites produced by warm compaction and microwave sintering, linking their microstructure to abrasive response [76]. This route illustrates the coupling between the initial contact network and subsequent consolidation. The relevant comparison is consequently not pressure alone but the distribution of metal contacts and reinforcement-rich regions that survives into the sintered material.

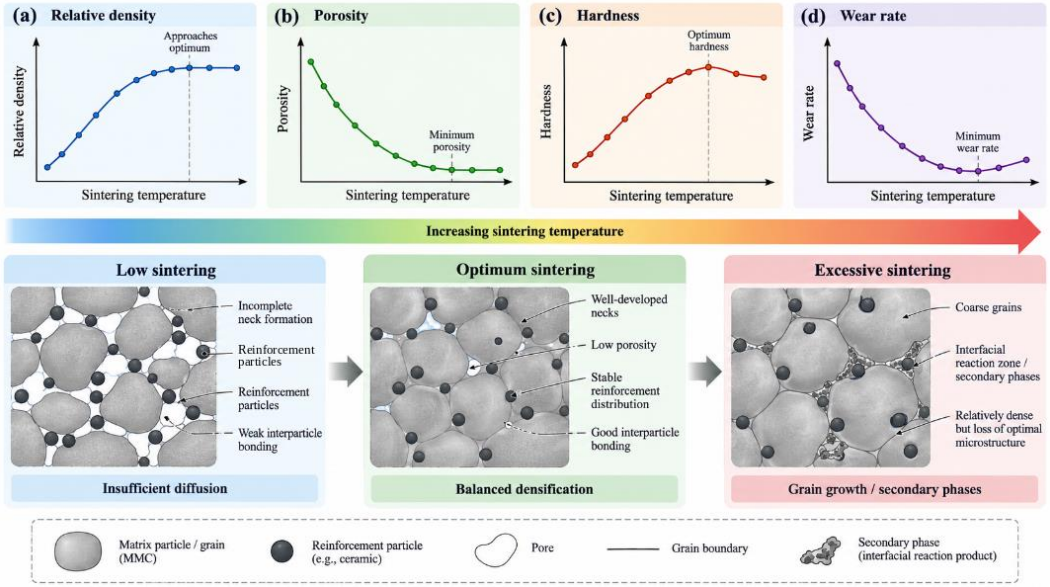

Figure 3. Conceptual relationships between sintering temperature, densification, microstructure, and mechanical/tribological response. The process coordinate is sintering temperature, not

compaction pressure. Filled inclusions in the lower diagrams denote reinforcement particles, whereas unfilled interparticle regions denote pores. The curves are qualitative rather than universally measured response functions.

Relative density should be calculated against a composition-appropriate theoretical density, rather than the density of the unreinforced matrix. For non-reacting constituents with mass fractions w_i and densities ϱ_i, $\varrho_{th} = 1/\Sigma(w_i/\varrho_i)$, and relative density is $\varrho bulk/\varrho_{th}$. This construction separates a low-density reinforcement contribution from a true pore contribution. In a reactive system, the final phase assemblage, rather than the starting powder mixture, determines the appropriate reference. Archimedes-type measurements, geometrical density, and gas-pycnometry results also probe different accessible volumes; connected pores and surface sealing must be considered when these methods are compared [4,90,91].

The addition of a more deformable metallic powder provides a processing lever distinct from increasing pressure. Cao et al. combined 2024 alloy powder with pure Al and SiC to improve compactability. Their work illustrates how powder-matrix deformability and ceramic obstruction jointly govern the green contact network. The implication for high-ceramic-fraction MMCs is that compaction should be optimized together with feedstock architecture: stronger alloy powder can retain shape but resist plastic accommodation around rigid particles. Spatial density uniformity and ejection damage are therefore meaningful acceptance criteria alongside the average green density [44].

3.3. Sintering Temperature and Holding Time

Temperature and dwell time determine the competition among bonding, pore elimination, grain growth, and interfacial reaction. The useful window is bounded by insufficient consolidation on one side and excessive coarsening, reaction, or matrix degradation on the other. Its location depends on chemistry, particle size, pressure, and atmosphere; a temperature cannot be judged independently of those variables [90,91,94].

The complete thermal cycle includes heating, dwelling, and cooling, with local gradients influenced by die geometry and the position of temperature measurement. Rapid pressure-assisted routes can limit grain growth, but their nominal setpoint and dwell do not fully describe specimen exposure. The final density, phase distribution, and grain structure reflect this integrated thermal history [93,96].

Liquid-phase formation accelerates particle rearrangement and pore removal while introducing dissolution, segregation, and interfacial reaction. The liquid fraction and its distribution determine whether improved contact is accompanied by uniform consolidation or by local enrichment and coarsening. Densification and phase evolution therefore define interacting trajectories, with the useful processing interval bounded by both pore closure and acceptable microstructural stability [91,94].

A useful sintering window can be established by measuring density and strength along the same temperature–time series. In the Al–SiC study of Cao et al., pressureless sintering of the investigated 35 wt.% SiC mixture was examined over 460–640 °C and 5–120 min. The favorable condition was 600 °C for 30 min; subsequent hot pressing produced a maximum tensile strength of 343 MPa, more than 70% above the sintered-only state. This result separates thermal bonding from pressure-assisted pore closure and shows that the best pre-sintering schedule need not itself deliver the best final mechanical state [44].

A useful distinction separates densification from chemical equilibration. Metal–metal neck growth may close pores before a reinforcement–matrix boundary reaches its final reaction state; conversely, a rapid interfacial reaction can form a rigid shell while the surrounding powder compact remains porous. The corresponding processing window is

bounded by insufficient contact at short exposure and excessive coarsening or reaction at prolonged exposure. Optimizing the thermal cycle therefore requires the relative rates of pore closure, matrix grain growth, and reaction-layer development to be considered together. Density alone identifies the extent of consolidation but not the chemical stability of the interface [29,90,91,94].

The thermal history also determines how much reinforcement is retained as the original phase. A conceptual diffusion-controlled reaction thickness scales with the square root of accumulated thermal exposure, but the proportionality and activation energy are interface-specific. Heating and cooling segments, intermediate holds, and later coating or heat-treatment steps can therefore contribute to reaction progress. This is especially important for carbon-containing Ti and Al systems: a short consolidation dwell cannot by itself establish limited reaction if the component subsequently undergoes a long thermal treatment. Reaction kinetics and densification kinetics must be evaluated as separate, interacting trajectories [8,29,91].

3.4. Sintering Atmosphere and Interfacial Stability

Atmosphere controls the chemical potential of oxygen and other reactive species at powder surfaces. Gas purity, pressure, flow, and moisture affect oxide growth and removal, while the stability of an existing surface oxide depends on matrix chemistry. An inert atmosphere mainly limits additional oxidation; its effect differs from chemical reduction of an oxide-bearing contact [3,90,91].

Mechanical oxide disruption, chemical reduction, diffusion, and liquid-phase-assisted contact are distinct pathways. Their relevance changes between Cu and reactive Al, Mg, or Ti powders. Carbon-containing systems additionally require attention to residual oxygen, reinforcement transformation, and matrix–carbon reaction. Atmosphere selection should therefore be justified by the intended final interface, not only by a generic preference for protection from air [3,7,8,23].

Atmosphere selection requires chemical specificity. An inert atmosphere can suppress additional oxidation without removing an existing stable oxide; hydrogen-containing gas does not reduce all metal oxides equally. Residual moisture, oxygen activity, graphite tooling, lubricants, and process-control agents can each alter the final interface chemistry. Accordingly, nominal gas identity should be accompanied by purity, flow or pressure, and the route used to remove organic residues. In carbon-reinforced composites, oxygen functionality may assist initial dispersion yet later evolve into gaseous products or interfacial species. Processing should preserve useful bonding while preventing trapped gas and uncontrolled oxidation [4,7,90,96].

3.5. Advanced and Pressure-Assisted Consolidation

Hot pressing, hot isostatic pressing (HIP), and field-assisted sintering technology (FAST) introduce additional driving forces for consolidation. Spark plasma sintering (SPS) is the commonly used designation for a pressure-assisted FAST configuration employing electrical heating. Throughout this review, SPS identifies that specific processing configuration, whereas FAST denotes the broader family. Its rapid thermal cycle can limit coarsening and reaction, although local temperature and current paths depend on tooling, contact resistance, and specimen geometry [93–96,107].

In SPS, current path, tooling, compact conductivity, and pressure affect heating and densification. Rapid heating can reduce exposure time, but specimen–die temperature differences and spatial gradients remain relevant. The route must therefore be assessed through measured density, phase constitution, and grain structure. In mechanically milled Al–SiC, Saheb et al. reported retention of a refined crystallite structure and a

Vickers hardness (HV) of 171.53 at 10 wt.% SiC; crystallite size is not automatically a metallographic grain-size statistic [41,96].

HIP requires appropriate encapsulation or closed-pore conditions to exploit pressure for internal pore closure. Microwave processing adds dielectric/electromagnetic coupling and thermal-distribution considerations rather than guaranteeing homogeneous heating. Route selection balances achievable structure, component geometry, repeatability, and cost; conventional sintering can remain appropriate where powder chemistry and geometry accommodate its cycle [91,93,95].

Electrical and thermal fields in SPS are coupled to the evolving contact network. Tooling geometry, powder conductivity, pressure, and temperature measurement position influence the actual specimen thermal history. Consequently, short nominal dwell time is most informative when accompanied by final density, phase constitution, and retained reinforcement geometry. The mechanistic interpretation rests on Joule heating and pressure-assisted consolidation unless an additional field-related process is independently demonstrated [96,107].

Pressure-assisted routes also differ in the defects they can close. Uniaxial hot pressing may introduce preferred reinforcement orientation, whereas HIP provides a different stress state and depends on whether pores are open, closed, or isolated by encapsulation. Rapid heating can help preserve fine structures, but specimen dimensions and tooling affect gradients and reproducibility. Comparisons of SPS, hot pressing, and HIP are strongest when final density, grain size, phase content, and reinforcement orientation are reported together. The engineering advantage is a controlled final state, not the processing acronym itself [66,93,96].

3.6. Processing-Induced Microstructure and Property Development

The descriptor set should include reinforcement distribution, matrix grain/crystallite scale, connected and isolated porosity, phase constitution, and interface integrity. These need not move favorably together. Better dispersion can coexist with carbon damage, and higher density can coexist with a thicker resistive or brittle interlayer. A property change should be interpreted against the complete measured state [8,23,29,41].

The distinction between matrix refinement and interface modification is particularly important when processing improves several properties simultaneously. Lower porosity and smaller grains can raise hardness without changing intrinsic boundary strength, whereas a chemically modified interface can improve transport even when density changes little. Relating these responses to separately measured descriptors reveals which aspect of processing controls the final property balance [30,33,41,53].

Post-consolidation deformation adds a further architectural variable. Rolling, extrusion, or severe plastic deformation can align platelets, break residual clusters, close pores, and refine the matrix simultaneously. The final material may therefore exhibit directional strength and conductivity even when the starting powder blend was isotropic. A reinforcement fraction established before deformation remains chemically relevant, but the operative spacing and orientation must be associated with the final tested state. This distinction is especially important for graphene/Cu and layered Al systems, where geometry can determine the efficiency of both stress transfer and heat flow [45,51,54].

Processing changes different intermediate structures: hot pressing can close pores and strengthen interparticle contacts, whereas platelet alignment alters the continuity and direction of heat-flow paths. These interventions produce different combinations of mechanical and functional response even when both improve the apparent quality of consolidation. Table 2 relates representative processing changes to their measured structural descriptors and engineering implications [44,51,53,66].

Table 2. Processing interventions, intermediate microstructural descriptors, and associated engineering implications.

Intervention/Evidence	Intermediate Descriptor	Property or Comparison	Engineering Interpretation
Powder deformability and post-sintering hot pressing [44]	Green contact network; final relative density; interparticle bonding	600 °C/30 min favorable pre-sintering condition; maximum tensile strength 343 MPa after hot pressing	Improved compactability and subsequent pressure-assisted densification contribute at different processing stages.
Pressure-assisted TiB architecture [32,66]	Reinforcement connectivity; Ti ligament size; residual pores	Strength–elongation balance and tribological response	A designed network is not equivalent to accidental agglomeration.
SPS electrical/thermal history [96,107]	Current path; specimen versus die temperature; displacement	Densification and retained microstructure	A common machine schedule does not establish equal specimen thermal histories.
Cu blending or platelet alignment [51,53]	Dispersion; retained sheet geometry; directional connectivity	Conductivity retention or directional heat flow	Mixing quality and architecture are different interventions.
Carbon/metal chemical modification [33,55]	Oxygen state; metal decoration; contact or boundary coupling	Interface conductance or bulk thermal/mechanical response	Interface-sensitive conductance and bulk conductivity probe different length scales.
W-derived interlayer on diamond [56,108]	Carbide phase sequence; boundary continuity	Bulk thermal conductivity and modeled interface response	Beneficial reaction is chemistry- and geometry-specific; no universal layer thickness follows.

4. Matrix-Dependent Behavior of Metal Matrix Composites

Matrix density, deformability, thermal expansion, chemical reactivity, and oxide stability determine the function of a reinforcing phase. The associated service environment further governs whether load support, transport, or protection is the principal objective. Matrix-specific comparison consequently connects the alloy condition and fabrication history to the response of ceramic, carbonaceous, and hybrid architectures [3,5,6,11,23].

4.1. Aluminum-Based Metal Matrix Composites

Al-based MMCs combine low density with extensive alloy and processing flexibility. The design problem is to translate reinforcement into useful specific mechanical or functional performance while retaining matrix continuity and damage tolerance. Hard ceramics, carbonaceous phases, and hard–lubricating combinations address different functions. The useful distinction is between resisting deformation, controlling sliding shear, and managing transport or environmental response [6,8,109].

4.1.1. Ceramic-Reinforced Al Matrix Composites

SiC restricts local deformation in Al, with the final contribution determined by distribution, matrix state, and densification. Akbarpour et al. examined nanoscale SiC incorporated through PM, while Shaikh et al. compared the influence of sintering techniques [36,37]. Together, these studies establish that reinforcement scale and consolidation route are coupled design variables. Matrix refinement, pore elimination, and particle constraint can contribute concurrently to a measured hardness increase.

Saheb et al. reported 171.53 HV for mechanically milled and SPS-consolidated Al containing 10 wt.% SiC [41]. The retained XRD crystallite scale provides evidence of a refined coherent structure, but is not identical to an electron backscatter diffraction (EBSD) grain-size distribution. Density, matrix refinement, retained dislocations, and ceramic obstacles may contribute concurrently; the available measurements determine how specifically these contributions can be interpreted.

B_4C reinforces Al through a combination of rigid-particle support and processing-dependent matrix constraint. In PM Al2024, Varol and Canakci compared median B_4C sizes of 5 and 49 μm across contents up to 20 wt.% [27]. Hardness increased within the investigated range while bulk density decreased. The density response combines the lower density of the constituent with any residual pore contribution, and the rising hardness trend places the best-performing tested composition at the sampled boundary rather than at an interior maximum.

The stir-cast Al7075–B_4C series of Rajanish et al. provides a melt-processing comparison [34]. At the reported 5% condition, Brinell hardness (HB) increased from 83.97 to 118.41 HB (H/H_0 = 1.410), while volume loss per sliding distance decreased from 9.124×10^{-3} to 5.223×10^{-3} mm^3/m (ratio 0.572). These wear values describe loss per distance and are retained on that basis; a load-normalized conversion additionally requires an unambiguous load associated with each endpoint. Their interpretation remains specific to the cast alloy and its processing history.

Canakci and Varol provide a distinct solid-state route involving AA7075 chips, added Al powder, SiC, and hot pressing [42]. Reinforcement content is only one of several variables because the added powder changes packing and metal-to-metal contact. Such recycling-oriented processing should be distinguished from both a fully powder-derived feedstock and melt casting. Route classification is consequently an essential part of the comparison, not merely a table label.

For Al–SiC and related reactive pairs, the final interface must also be checked for reaction products. The formation, continuity, and extent of an Al–C product can change damage and environmental response. Absence of a detectable new XRD peak is not sufficient to establish an atomically reaction-free boundary; when the interpretation depends on a thin layer, local microscopy and chemistry are needed [8].

The distinction between hardness optimization and damage tolerance is evident in size-controlled Al–SiC systems. Small particles provide shorter matrix slip distances and relatively fine-scale constraints, while larger particles introduce larger potential fracture origins. Tokaji's fatigue comparison of PM Al2024 containing 10 wt.% SiC at different particle sizes therefore complements monotonic strength measurements rather than merely reproducing their ranking [43]. The engineering consequence is that particle-size selection depends on the dominant damage process: plastic indentation, abrasive penetration, fatigue initiation, and long-crack propagation sample different structural length scales.

The preferred ceramic size also depends on the loading mode. Tokaji et al. examined PM 2024 Al with 10 wt.% SiC at average sizes of 5, 20, and 60 μm. The 5 μm condition improved rotary-bending fatigue strength; the 20 μm condition changed from a benefit at higher stress to a slight penalty at lower stress, whereas the 60 μm condition reduced fatigue strength. Crack initiation, rather than a universal change in small-crack propagation, controlled much of this difference. Thus, a particle size selected from indentation or wear alone may not satisfy fatigue-critical structural service [43].

4.1.2. Hybrid Ceramic Reinforcement and Tribological Synergy

Bharathi and Kumar compared PM Al/SiC and Al/SiC/B_4C systems [10]. Combining the two ceramics changes the distribution of rigid load-bearing sites, packing behavior, and the reinforcement–matrix contact network. The hybrid response therefore

incorporates both the properties of the constituents and the microstructure produced during consolidation. Its practical value is the resulting balance of mechanical resistance and wear rather than the presence of two hard phases alone.

A PM hard–lubricating example is Al6061 containing 2–8 wt.% B_4C and a fixed 2 wt.% BN. Chand et al. varied compaction pressure from 200 to 800 MPa and sintering temperature from 400 to 600 °C [28]. Increasing B_4C reduced compressibility and sinterability, yet the 8 wt.% B_4C–2 wt.% BN condition at 800 MPa/600 °C gave the reported maxima of 184 HV and 249 MPa compressive strength. Final property improvement and ease of consolidation are therefore different outcomes.

Ceramic-rich hybrid regions can support applied contact load while restricting local plastic flow. Their benefit is reduced when particle fracture or debonding supplies abrasive debris, making interface retention important alongside bulk hardness. The measured hardness–wear relationship consequently reflects both resistance to penetration and the stability of the load-bearing architecture during repeated sliding [10,28,110].

Hierarchical ceramic–carbon arrangements extend hybridization beyond homogeneous mixing. Zhang and Li combined graphene and Al_2O_3 within a bioinspired Al architecture and reported simultaneous improvements in strength and toughness [46]. The significance lies in coordinating hard platelet support with a deformable metallic phase and interfacial interlocking, rather than attributing the response to two independent reinforcement increments. Such architectures provide a structural route to distributing deformation across multiple length scales, although their orientation and processing history remain integral to the measured response.

4.1.3. Hard–Lubricating Hybrid Systems: ZnO–hBN and Related Architectures

ZnO–hBN/Al combines ceramic support with the shear-accommodating function of a lamellar phase. The study reports maximum hardness of 105 HB for its 10 wt.% hBN formulation and an approximately sevenfold increase in wear resistance for its 1 wt.% hBN formulation [111]. The different endpoints reflect the balance between strengthening and lubrication. These hBN labels describe the formulations used in that study and remain distinct from the total amount of hybrid reinforcement in the final Al composite.

The difference between the hardness and wear endpoints is the central design insight. Matrix constraint, lubricant availability, and particle retention do not necessarily favor the same composition. Increasing a lubricating phase can accommodate shear while reducing the continuous load-bearing metal. A useful selection therefore satisfies a minimum mechanical requirement and an explicit friction/wear target rather than maximizing one measurement.

The hard–lubricating concept is transferable only after the stability of both functions is considered. A ceramic-rich surface requires adequate matrix support, whereas a lubricating phase requires access to the contact and a renewal mechanism as material is removed. Excessive lubricant coverage can lower shear resistance but also weaken interparticle contacts during consolidation. The preferred composition therefore depends on whether the component experiences continuous sliding, interrupted contact, abrasive ingress, or corrosive exposure. This explains why the composition yielding maximum hardness in ZnO–hBN/Al need not maximize wear life, without requiring one endpoint to be treated as anomalous [13,73,111].

4.1.4. Carbonaceous Reinforcements in Aluminum Matrices

Graphene, graphite, and CNTs introduce high-aspect-ratio geometries and potentially useful transport or shear responses. GO and rGO additionally differ in oxygen functionality and defect state. Their effective contribution depends on the dimensions and

structure retained after mixing and consolidation, not simply the nominal starting material [1,38–40,112].

Rashad et al. evaluated microstructural, mechanical, and electrochemical behavior in Al reinforced with graphene nanoplatelets [39], while Esawi et al. examined CNT-content effects in Al [40]. These studies emphasize the need to retain both content and distribution. An observed mechanical gain does not independently establish improved corrosion or electrical behavior, and a higher fraction can introduce local heterogeneity without changing the nominal matrix chemistry.

Liu et al. engineered nano-SiC-cladded CNTs for Al composites [38]. Such decoration is an interface intervention rather than simply another additive. Its value depends on preserving a useful carbon aspect ratio while modifying the matrix contact. Carbon dimensions, Raman structural indicators where measured, local chemistry, and density help distinguish improved incorporation from fragmentation or excessive reaction.

Ceramic, carbonaceous, and decorated reinforcements modify different parts of the deformation and transport response. Rigid ceramics primarily provide local load support; carbonaceous phases additionally influence shear and conduction; decorated structures modify the connection between these phases and the metal. Their practical contribution is determined by the geometry and chemistry retained after processing and by the function required during service [8,12,38].

Li et al. produced bioinspired nanolaminated rGO/Al composites in which the organization of composite powders generated an ordered reinforcement–metal architecture [45]. The simultaneous enhancement of mechanical performance and retention of tensile deformability demonstrates that carbon content alone does not describe reinforcement efficiency. Layer alignment, matrix ligament dimensions, and the continuity of the interfaces provide additional degrees of freedom. Relative to a randomly clustered carbon addition, a designed laminate can redistribute local stress and promote controlled deformation, but its through-thickness response remains a separate design consideration.

Direct deformation experiments provide a stronger basis for carbon-reinforcement mechanisms than hardness alone. Boesl et al. observed strengthening during in situ tensile testing of SPS Al containing 1 vol.% CNTs, with reported increases of approximately 40% in strength and 65% in stiffness relative to their reference. Pull-out and telescopic wall sliding were observed, showing that reinforcement deformation and interwall processes participate in the response. Chen et al. further used in situ tensile observations in aligned CNT/Al to connect nanotube fracture with load transfer. These experiments support mechanism-specific interpretation, while remaining conditional on retained tube geometry and interface state [99,100].

4.1.5. Microstructural Evidence: From Reinforcement Addition to Performance

A nominal concentration may produce either a dispersed architecture or reinforcement-rich clusters separated by a depleted matrix. Representative SEM sampling and density measurements distinguish these states, while EDS and XRD identify compositional or phase associations. None alone uniquely quantifies stress transfer or retained dislocation strengthening [8,27,41].

Microstructural interpretation integrates particle distribution, matrix grain structure, porosity, and reaction products with the observed deformation mode. Agreement between these measurements strengthens the assignment of a governing mechanism; different combinations can produce similar hardness. In particular, a refined matrix with residual interface gaps and a coarser matrix with strong particle retention need not exhibit the same tensile, fatigue, or wear response despite comparable indentation values [8,27,41,43].

4.1.6. Comparative Assessment of Al-Based Systems

All selection rules are conditional. Stiffness and load support favor effective ceramic volume, matrix continuity, and particle retention. Sliding wear additionally requires counterface, debris, and film evidence. Carbon-containing systems require attention to aspect ratio, structural integrity, and transport/environmental constraints. Processing that improves one descriptor can worsen another, so a composition-only ranking is insufficient [8,10,27,38,39].

A maximum at the highest tested content is a best-performing tested endpoint, not an established interior optimum. Bracketing and specimen-level uncertainty are needed to locate a true maximum. Where hardness, fatigue resistance, ductility, wear, and corrosion favor different compositions, the useful result is a feasible region or non-dominated set. Section 5.4 develops this interpretation through explicit size–route–property comparisons.

For Al-based component selection, the evidence supports a staged decision. First establish that the matrix heat-treatment condition, density, and reinforcement retention meet the structural requirement. Then evaluate whether the ceramic or carbon architecture improves the required surface or transport response. Finally examine a failure-sensitive property—such as fatigue, elongation, or environmental stability—that is not represented by hardness. The size-dependent fatigue result and the pressure-assisted high-SiC result show why these stages cannot be collapsed into a single maximum-hardness composition [39,43,44].

4.2. Copper-Based Metal Matrix Composites

Cu requires a structural–functional balance because conductivity is often part of the reason for selecting the matrix. Reinforcement can constrain deformation or alter sliding shear while changing the continuity and resistance of conducting paths. Bulk electrical conductivity, contact resistance, and thermal conductivity are distinct responses and should not be inferred interchangeably [9,11,23].

Independent studies broaden the comparison beyond one experimental series: Gao et al. investigate mechanical and thermal response [52]; Chu et al. engineer aligned graphene networks [51]; Wang et al. combine transport, mechanical, and corrosion measurements [24]; Souza et al. compare GO blending routes [53]; and Shi et al. use copper-formate-derived powder chemistry [54]. These studies address different control variables and form complementary evidence rather than a single pooled dataset.

4.2.1. Ceramic and Metallic Reinforcement of Cu Matrices

The fixed-1-wt.% PM Cu series compares B_4C, B, Cr, Co, Al_2O_3, and graphite under a common nominal protocol [13]. This improves internal comparability but does not hold reinforcement volume, surface area, morphology, or local densification constant. The resulting ranking belongs to this experimental design, not to reinforcement chemistry independent of geometry and processing.

The reported hardness order is Cu–B_4C > Cu–B > Cu–graphite > Cu–Al_2O_3 > Cu–Cr > Cu–Co. Relative to 70 HV0.3 for the processed Cu control, the corresponding means are 118.24, 116.50, 114.78, 113.25, 99.88, and 95.23 HV0.3. Ratios span 1.360–1.689. These integrate matrix, porosity, phase, and local constraint effects; they do not quantify a unique interfacial-strengthening increment [13].

Dominant face-centered cubic (FCC) Cu peaks identify the principal matrix phase but do not exclude thin, amorphous, or low-fraction interface products. Particle retention in SEM is useful correlative evidence but is not an interface shear-strength measurement. The interpretation therefore separates the observed structure from the proposed cause of the mechanical improvement [8,13].

The Cu reference and its reinforced counterparts were processed and tested within a common experimental series. The hardness improvements therefore quantify the response to the selected additions under that route, including their effects on matrix structure, dispersion, and densification. Because the additions were matched by mass rather than volume, the series does not isolate an equal-volume intrinsic reinforcement efficiency [13].

Section 6.4 supplies the within-study numerical basis for this Cu comparison. The mechanistic distinction is between rigid-particle support and potential carbon-assisted shear accommodation, both dependent on retained architecture and the wear environment.

Equal mass fraction is a useful manufacturing control but does not isolate chemistry alone. Different constituent densities produce different particle volume fractions, and different dimensions produce different interface areas. A more informative interpretation therefore combines mass and volume fraction with matrix ligament width and particle retention. Independent Cu studies on precursor-derived TiB_2 and controlled graphene incorporation broaden the comparison beyond any one experimental series. They indicate that hard-phase generation, metal continuity, and processing-induced matrix state are separate design levers, each capable of changing the apparent strengthening efficiency [11,50,52,53].

4.2.2. Boron- and B_4C-Containing Cu–Cr Hybrid Composites

Kara et al. vary sintering temperature, additive ratio, and B/B_4C particle size in Cu–Cr [47]. This addresses a different question from the fixed-mass-fraction Cu comparison: how composition, geometry, and thermal processing interact. It does not isolate one universal B_4C fraction transferable between Cu and Cu–Cr matrices.

A temperature change can improve density while also modifying Cr distribution, interface reaction, or particle retention. A useful interpretation therefore retains the final density and phase state alongside the hardness or wear response. Without a matched descriptor set, a difference between the two research series is conditional evidence, not a contradiction or a direct chemistry-only ranking [13,47].

A separate Cu composite study uses an Al–TiB_2 precursor to introduce reinforcement [50]. Classification follows the final Cu matrix and fabrication route, not the aluminum-containing precursor. This avoids turning a preparation label into an incorrect Al–TiB_2 bulk-composite dataset.

In Cu–Cr hybrids, a hard ceramic and a metallic solute or precipitate affect the matrix through different pathways. Changes in sintering temperature can alter particle bonding and the Cr-containing matrix state simultaneously. A composition series should therefore retain the cooling history and any subsequent aging treatment, rather than attributing the entire response to B_4C. The relevant transport question is whether the selected hard-phase distribution preserves sufficiently continuous Cu pathways; the relevant wear question is whether those particles remain supported during repeated loading. These requirements motivate measuring electrical response alongside density and tribological loss [11,47].

4.2.3. Graphene Oxide-Reinforced Cu Composites

The PM/hot-pressed GO–Cu series examined 0.5, 0.75, and 1 wt.% GO. At the upper tested loading, we reported a hardness increase of 109.97%, wear-loss decrease of 82.88%, and COF decrease of 51.33%, corresponding to ratios of 2.100, 0.171, and 0.487 [14]. The result establishes a best-performing tested condition, not an interior optimum outside the sampled range.

SEM/EDS and matrix-phase observations support effective incorporation but do not independently partition load transfer, grain-boundary strengthening, and retained-

dislocation contributions. A grain-size statement must identify its measurement method. The tribological response also does not establish an electrical benefit because conductivity is not a reported endpoint of this GO study [14].

Souza et al. compare mechanical stirring, rotary evaporation, tip ultrasonication, and ultrasonication followed by stirring [53]. Their combined route provides a favorable overall dispersion/property response, while 0.25 wt.% GO did not significantly alter conductivity relative to the Cu control. This directly shows why the blending method should accompany concentration in Cu–GO comparisons.

The numerical PM GO and arc-induction rGO results remain separate in the study-specific comparisons in Section 6.4. Carbon state, processing history, matrix reference, and indentation scale differ. A common graphene-related label is insufficient to combine the data [14,35,53].

The retained oxygen state provides an additional control variable in GO/Cu. Oxygen-containing groups may facilitate initial interaction with powder surfaces, but their later evolution changes local chemistry and can affect gas release, defects, and transport. The direct graphene–metal measurements of Jiang et al. show that some oxygen-mediated bonding can improve boundary heat transfer, whereas removing all oxygen is not automatically the best interfacial strategy. That thin-interface result does not predict a bulk GO/Cu conductivity by itself; it identifies a chemical variable to measure and control alongside consolidation and sheet connectivity [14,33,53].

4.2.4. Hybrid Al_2O_3–Graphene Reinforcement in Cu

The Al_2O_3–graphene–Cu architecture combines a rigid ceramic with a high-aspect-ratio carbon phase. Alumina provides local constraint and load support, while graphene can modify interface contact and sliding response. Their combined performance is governed by whether both phases are integrated within a continuous Cu skeleton or segregated into reinforcement-rich regions. Comparison with the corresponding single-addition systems separates the practical advantage of hybrid functionality from a stronger claim of super-additive strengthening [13,48].

The microstructural basis of hybrid performance includes the location of each reinforcement relative to Cu grain boundaries, the continuity of metal contacts, and the tendency of ceramic particles to associate with carbon sheets. Co-location can create a useful hierarchical interface or a poorly consolidated cluster. These alternatives have different consequences for load transfer and conductivity and are distinguished by spatially resolved characterization rather than total reinforcement fraction alone [23,38,48].

Metal decoration provides an independent hybrid route. Yang et al. incorporated nickel nanoparticle-decorated, oxygen-plasma-treated graphene into sintered Cu. At the reported 0.1 wt.% addition, thermal conductivity and shear strength reached 216.2 W/(m·K) and 56.3 MPa, respectively. The stated improvements of 105.3% and 87.3% refer to the study's sintered Cu-nanoparticle control, not annealed bulk copper. This distinction matters: an intervention can produce a large relative benefit by repairing weak interparticle contacts while the absolute conductivity remains below that of dense conventional Cu [55].

4.2.5. Doped-rGO/Cu Hybrid Composites and Multifunctional Performance

B-, N-, and Si-doped rGO introduce chemical variables that can modify defects, contact, and carrier scattering [49]. These effects must be separated from density, dispersion, and metal continuity. Joint mechanical, tribological, and electrical measurements support multifunctional selection but do not establish a dopant ranking independent of fabrication.

Shi et al. use GO/copper-formate precursors to establish intimate contact before consolidation [54]. At 0.49 vol.% rGO the reported room-temperature yield strength and

thermal conductivity are 553 MPa and 364 W/(m·K). These endpoints describe a specific precursor/consolidation state; later rolling changes that state. Volume percent should not be converted to mass percent without constituent densities and an explicit conversion assumption.

Atomistic calculations offer a complementary explanation for chemical modification. Fang et al. used density functional theory to examine Cu interaction with defective and heteroatom-modified graphene, including boron and oxygen-mediated bonding. The predicted bonding changes support a plausible route for modifying adhesion and mechanical response, but are not experimental measurements of doped-rGO/Cu conductivity or wear. Validation requires the actual dopant configuration, chemical state, and interface coverage to be established in the consolidated composite. This separation allows theoretical insight to guide processing without treating an idealized interface as a measured bulk material [49,113].

4.2.6. Powder Consolidation and Arc Induction Melting of Cu–Carbon Composites

Arc induction melting changes incorporation from solid-state powder contact to melt dispersion and solidification. Relevant variables include melt flow, carbon retention, solidification texture, and oxygen pickup. PM/hot pressing additionally retains powder-boundary oxides, compaction history, and pore closure. These are distinct processing histories, not interchangeable labels for the same Cu–carbon structure [14,35].

At 1 wt.% rGO, the arc-induction study reported a hardness increase from 65 ± 4 to 225 ± 3 HV30, corresponding to a mean-value ratio of 3.462. The reported sampling comprised five indentations per specimen. Its sliding protocol used a 10 N load, a speed of 50 mm/s, and a distance of 1000 m. The indentation variation characterizes within-specimen measurements and is distinct from the variability of independently fabricated specimens [35].

Electrical conductivity increased from 1.9×10^5 to 2.0×10^5 S/cm, equivalent to 19 and 20 MS/m, respectively. The ratio of 1.053 describes conductivity retention and improvement relative to that processed Cu reference. Both the absolute level and the reference state are important for electrical-contact selection because a relative increase does not establish equivalence to high-purity annealed copper [35].

The PM GO/Cu and arc-induction rGO/Cu studies exhibit different hardness ratios and characterization sets. Their difference combines carbon chemistry, matrix condition, reinforcement incorporation, and indentation scale rather than representing a route-only effect. In PM, powder-boundary oxides and incomplete neck formation can interrupt metallic continuity; in a melt route, carbon redistribution, wetting, and solidification structure become dominant controls. The reported responses are therefore interpreted through these route-specific structural variables [14,35].

Powder routes initially place carbon on or between metal particles, after which pressure and diffusion establish contact. Melt incorporation instead subjects the carbon phase to fluid motion and a moving solidification front, with possible changes in retained geometry and local concentration. Subsequent rolling, extrusion, or annealing modifies both architectures through texture development, pore closure, and carbon alignment. Final-state grain structure, retained carbon chemistry, relative density, and orientation are consequently central to evaluating route-dependent performance [14,35,51,54].

Microwave-sintered Cu–rGO provides an independent powder-route comparison. Chen et al. combined wet ball milling with microwave sintering under argon and obtained 81.1 HV, 87.10% International Annealed Copper Standard (IACS) electrical conductivity, and 391.62 W/(m·K) thermal conductivity. Local hardness differed between oxide-containing and precipitate-free regions, linking matrix heterogeneity to the measured response.

The study demonstrates that simultaneous hardness and transport measurements can reveal processing effects that are obscured by a single bulk average [57].

Taken together, hot pressing, microwave sintering, and arc induction melting produce distinct metal–carbon contact histories. A transferable route advantage requires comparison at equivalent final reinforcement volume, matrix composition, and test scale. Nevertheless, the existing evidence already identifies useful design priorities: preservation of continuous Cu paths, control of oxygen-bearing regions, and retention of an effective carbon architecture. These priorities connect route selection to the required combination of mechanical resistance, sliding stability, and conduction rather than to hardness gain alone [14,35,54,57].

4.2.7. Critical Comparison of Reinforcement Mechanisms in Cu-Based MMCs

Three functions organize the Cu evidence: maintaining a load-bearing metal network, retaining reinforcement under contact, and preserving charge/heat transport. Ceramic additions emphasize constraint, graphitic additions may also accommodate shear, and chemical/architectural changes modify contact and conduction. Similar hardness can therefore arise from different structures with different functional consequences [11,23,24,51–54].

Current-carrying contacts introduce resistance and temperature evolution at the sliding junction in addition to bulk conductivity. Oxide formation, material transfer, and interruption of real contact area can therefore alter electrical performance while specimen wear remains low. Bulk strengthening is valuable when it stabilizes the contact without excessively reducing conductive continuity; evaluation of the complete contact requires the electrical and mechanical loading conditions to be considered together [23,24].

The comparison becomes more informative when the competing mechanisms are represented by different observables. A hardness increase with lower porosity supports improved constraint but does not identify a low-shear film. A lower friction coefficient with retained conductivity may favor a carbon-assisted contact architecture, whereas increased thermal conductivity after boundary modification tests a transport mechanism. Mechanical, tribological, and electrical endpoints should therefore be plotted or tabulated as a vector of responses from the same material state. Combining the best endpoint from each processing state would describe a composite that was not actually tested [51,53–55].

4.2.8. Comparative Assessment and Design Implications

For a non-current-carrying wear component, retention and usable toughness may dominate; for a contact, conductivity and heating are mandatory constraints; for a heat spreader, direction, expansion mismatch, and boundary resistance are essential. A practical selection rejects candidates that violate these requirements before comparing remaining trade-offs. The outcome is a feasible set rather than a universally weighted score.

Thermal-management Cu composites further expand the reinforcement design space beyond graphene and conventional wear ceramics. Wang et al. achieved 640 W/(m·K) in a hot-pressed diamond/Cu composite at 50 vol.% diamond using a tungsten-derived carbide interlayer. The reported interlayer phase composition was predominantly WC, with smaller W_2C and residual W fractions. Yang et al. subsequently examined tungsten-coated diamond/Cu consolidated by SPS. Together, these studies identify conversion of a poorly coupled diamond–Cu boundary into a chemically engineered heat-transfer path as a distinct design objective; their high diamond fraction is not comparable to low-content wear-modifying additions [56,108].

4.3. Fe/316L-, Mg-, Ti-, and Ni-Based Metal Matrix Composites

Fe/316L-, Mg-, Ti-, and Ni-based systems extend interface engineering across distinct service constraints. Steel emphasizes the balance between hard-phase formation and damage tolerance, Mg couples low density with environmental sensitivity, Ti requires control of reactive interfaces and phase architecture, and Ni introduces temperature-dependent stability and lubrication. These differences determine which microstructural descriptor is most relevant to the selected application [3,25,26,29,58,66,69].

4.3.1. Fe- and 316L Stainless-Steel-Based Composites

Matrix grade and reaction path remain important in ferrous MMCs. TiC-reinforced Fe and B- or Al_2O_3-containing 316L do not share one interface chemistry. The in situ/in-mould Fe–TiC production comparison is retained as a non-PM comparator, whereas the B/Al_2O_3–316L series concerns PM consolidation; these studies address different route and chemistry questions [69,70].

The 316L study includes unreinforced material, mono-reinforced compositions, and B–Al_2O_3 hybrids produced by mechanical alloying and PM, with sintering at 1150 °C in argon [69]. XRD identifies Fe_2B/FeB in B-containing compositions and retained α-Al_2O_3. This establishes phase formation, whereas its contribution to strength requires phase fraction, continuity, distribution, and crack-path evidence.

Discrete hard phases can support load, while a connected brittle region can create a preferential fracture path. Hardness alone does not resolve this difference or demonstrate improved fatigue/corrosion resistance. The phase-based interpretation remains distinct from a directly measured interface-strengthening increment.

Reaction-derived reinforcement is also demonstrated independently in polymer-derived steel composites. Guan et al. processed a steel matrix with polymer-derived particles through PM; reaction of the derived ceramic species generated carbide and silicide constituents rather than simply preserving the original precursor as inert SiC. Such systems should be described by their final phases and distribution. For 316L-related designs, hard-phase strengthening must additionally be assessed against matrix continuity and corrosion-sensitive changes in local chemistry. A favorable tensile or hardness result does not independently establish that the original corrosion resistance of the stainless matrix has been preserved [69,70,72].

TiC–316L processed by warm compaction and microwave sintering supplies an independent ferrous example in which reinforcement content and consolidation jointly determine abrasive behavior [76]. Unlike boron-assisted formation of Fe borides, TiC incorporation introduces a pre-existing carbide whose effectiveness depends on retention and matrix support. The contrast highlights two separate design variables: whether the hard phase is produced by reaction or introduced directly, and whether the processing route provides sufficient continuity around that phase. Both routes can raise resistance to deformation, but their associated fracture paths need not be equivalent.

4.3.2. Magnesium-Based MMCs

Mg combines low density with sensitivity to surface oxides and electrochemical heterogeneity. TiB_2/AZ91 prepared by vacuum milling and hot pressing illustrates a tensile-property window: the reported 5 wt.% condition gave ultimate tensile strength of 234 MPa, yield strength of 91 MPa, and elongation of 7.3% [58]. This combination is not automatically the optimum for wear or corrosion.

Pure Mg, AZ91, and AZ92 retain different alloy/thermal histories and must not be merged into one reference. Hard inclusions can constrain deformation while changing oxide-bearing area, local packing, or electrolyte access. Specific strength is strength

divided by density; density normalization alone does not make wear protocols or corrosion endpoints service-equivalent [5,58,59].

Turan et al. examined 0.1, 0.25, and 0.5 wt.% graphene nanoplatelets in pure Mg through a semi-PM route [26]. The upper tested content gave the best wear response at 10 N despite partial agglomeration, while corrosion deteriorated relative to Mg. This directly demonstrates that a mechanically favorable content need not be environmentally favorable.

Pardo et al. evaluated PM AZ92–SiC in 3.5 wt.% NaCl, neutral salt fog, and high-humidity exposure [25]. The reinforcement increased attack and promoted corrosion-product cracking/spalling in salt fog, while its effect was weaker in high humidity. The exposure protocol is part of the result; one corrosion ranking cannot be detached from it.

For Mg, acceptable mechanical performance and environmental stability define a joint design constraint. Conductive inclusions can change local cathodic activity, while connected pores and reinforcement-rich boundaries alter electrolyte access. Surface barriers and bulk–coating combinations are particularly relevant when corrosion rather than dry wear controls component life. Their benefit depends on maintaining protection after deformation or wear exposes the underlying composite [25,26].

Recent hybrid Mg evidence permits a more quantitative comparison. Ogunbiyi et al. consolidated AZ91D with 1.5 wt.% Ni and a graphene-nanoplatelet series by SPS at 500 °C, 50 MPa, and a 5 min hold. The reported endpoints changed from 67.4 to 89.7 HV and from 5.21×10^{-3} to 3.85×10^{-3} $mm^3/(N \cdot m)$ in specific wear rate, giving ratios of 1.331 and 0.739, respectively. The wear protocol used a 10 N load. These results support a within-study mechanical–tribological benefit; the upper tested composition is not evidence of a universally transferable graphene optimum [60].

Dengiz et al. examined graphene fraction together with compaction pressure, sintering temperature, and time in PM Mg. Their favorable 0.15 wt.% condition, associated with 600 MPa compaction and 520 °C/60 min sintering, gave 44.34 HV, 300 MPa compressive strength, and 8.52×10^{-4} $mm^3/(N \cdot m)$. These values cannot be ranked directly against the AZ91D hybrid because matrix chemistry, secondary addition, and contact protocol differ. They demonstrate instead that a substantially lower carbon fraction can be useful when the powder and thermal route are different [64].

Carbon surface chemistry can separate the best mechanical and corrosion endpoints even within one Mg alloy. Li et al. compared graphene, carboxylated graphene, and GO in SPS AZ91D: the 0.1 wt.% carboxylated-graphene condition favored mechanical performance, whereas the 0.1 wt.% graphene condition favored corrosion behavior in the reported comparison. This complements the wear–corrosion divergence in semi-PM Mg/graphene and confirms that "carbon reinforcement" is not one electrochemical condition. Biodegradable Mg studies by Saberi et al. and Shahin et al. additionally require degradation and biological response to be assessed alongside mechanics; those application requirements should not be inferred from structural wear data [26,61–63].

Heterogeneous architecture provides another route to reconciling Mg property requirements. Xu et al. used an in situ reaction involving rGO–Fe_2O_3 and Mg to develop a layered heterogeneous structure with mechanical and electromagnetic functionality [65]. The reported deformation behavior involved activation of non-basal dislocations and distributed microcracking. This example broadens Mg reinforcement design from particle addition to coordinated spatial and interfacial organization. Its mechanical and shielding benefits address a different functional problem from corrosion protection, emphasizing that multifunctionality must be defined by the properties actually measured.

4.3.3. Titanium-Based MMCs

Ti requires control of interstitial uptake, reactive interfaces, matrix transformation, and reinforcement architecture. These can alter strength and ductility independently of nominal fraction. Comparisons should retain matrix alloy, final phase constitution, interstitial information where available, geometry, and test temperature [3,29,66].

HIP-consolidated in situ TiB/Ti–6Al–4V demonstrates architecture as a design variable [66]. A network-like arrangement changes matrix confinement and load paths relative to a uniform dispersion. Its hardness and tribological response should not be extrapolated to tensile damage tolerance without the corresponding fracture and deformation evidence.

Heat treatment in discontinuous-carbon-fiber/Ti changes TiC development and residual reinforcement geometry [29]. Reaction can promote contact while progressively consuming the carbon phase. The useful descriptor set is therefore layer-thickness distribution, phase identity, residual fiber dimensions, matrix condition, and measured response, not furnace temperature alone.

A useful reaction window is system-specific and requires bracketing by controlled thermal exposure. A favorable thin layer in one specimen does not define a universal critical thickness for all Ti–carbon systems. High-resolution cross sections, local chemistry, fracture location, and damage-sensitive mechanical tests are needed to establish that relationship [29].

Environmental performance remains separate: the Ti–Mo–Nb–Al–Si/TiC study concerns hot-corrosion resistance [67]. Room-temperature strengthening cannot establish elevated-temperature or corrosive-service reliability. Ti therefore extends the framework from indentation/wear optimization to retention of architecture and interface function under thermal exposure [3,29,67].

Ti provides a particularly clear example of the distinction between a designed network and uncontrolled agglomeration. Huang et al. tailored an in situ TiB-whisker network in PM Ti. At the reported 8.5 vol.% condition, tensile elongation reached 11.8% with a 74.6% strength increase relative to their reference. The architecture preserves comparatively deformable Ti regions while concentrating reinforcement in a connected skeleton. Therefore, a nonuniform reinforcement distribution can be deliberate and beneficial when its length scale, connectivity, and deformation accommodation are controlled; uniformity alone is not a sufficient design criterion [32].

The network concept and the Ti–carbon reaction-layer concept address different limitations. A spatial network redistributes where the hard phase carries load, whereas controlled reaction changes how load crosses an individual boundary. In carbon-fiber/Ti, thermal exposure also reduces the remaining carbon geometry as reaction products develop. In TiB/Ti–6Al–4V, pressure and architecture influence residual pores and load paths. Comparisons should therefore retain the matrix alloy and phase condition, reinforcement morphology, and consolidation/post-treatment sequence. Treating Ti, Ti–6Al–4V, and a reacted Ti–carbon composite as interchangeable baselines would obscure the source of the mechanical response [29,32,66].

The response of near-α Ti composites further demonstrates that the preferred TiB content depends on the deformation and failure endpoint. Li et al. hot-pressed TA15 with 0–4 vol.% TiB and observed changes in prior-β grain size, colony dimensions, and reinforcement location. The 1 vol.% condition improved strength, ductility, and strain hardening within that series [68]. Reinforcement at colony boundaries and within colonies participates differently in slip transfer and particle fracture. These observations support the use of matrix transformation structure and reinforcement position as design descriptors alongside the total TiB fraction.

For structural Ti applications, the relevant architecture must support both distributed plastic deformation and resistance to crack extension. Tensile strength and elongation

characterize monotonic loading, whereas fatigue initiation, crack-growth threshold, and fracture resistance probe the accumulation and localization of damage. Thermal exposure further changes matrix phases and reaction layers. This combination makes Ti MMC selection a problem of retained damage tolerance under the intended temperature and environment, rather than a direct extension of room-temperature hardness optimization [3,29,67,68].

4.3.4. Nickel-Based MMCs

Ni-based composites combine metallic load support with reinforcement stability, oxidation response, and temperature-dependent lubrication. A phase that accommodates shear at room temperature may oxidize or react during heating, while an initially ineffective additive can become active through smearing or reaction at elevated temperature. Temperature-resolved friction, wear, and surface chemistry therefore define the operative lubrication interval [71,85].

For carbide-containing Ni, intact carbide retention must be distinguished from dissolution and secondary-carbide formation. Similar hardness can mask different crack resistance. For carbon-containing Ni, processing-dependent carbon integrity and distribution matter alongside matrix grain structure. An interface explanation should identify which of these variables was measured rather than treating all carbon additions as equivalent [71].

The acceptance condition includes retained mechanical support, stable friction/wear, and a suitable oxidation response over the intended interval. A higher lubricating-phase fraction can reduce shear yet weaken the load-bearing network. The preferred fraction is therefore constrained by matrix continuity and operating temperature, not only the minimum measured COF [71].

Ni-based self-lubrication also depends on the phases actually generated during sliding. Davis et al. investigated hot-pressed NiMoAl composites with Cr_2AlC, Ag-containing, and MoS_2-containing additions. The Cr_2AlC–Ag formulation gave the most favorable combined response in that series, and Raman evidence linked the worn surface to Ag_2MoO_4 and Al_2O_3-containing products. The experiment provides a chemical basis for discussing tribofilm-assisted behavior rather than relying solely on a low friction value. Because those tests were conducted at ambient temperature, they do not independently validate the same ranking for elevated-temperature service [73].

Piasecki et al. examined PM Ni/NiCrSiB sinters containing 20 wt.% CaF_2 against an Inconel 625 counterface at 23, 200, 400, and 600 °C. Their tests used 5 N loading and three repeated wear experiments per condition. CaF_2 spreading on the specimen and counterface became particularly evident at elevated temperature, while the wear response shifted from pronounced cutting and ploughing toward film-associated behavior and oxidation [74]. This temperature-dependent evidence directly connects lubricant distribution to the evolving contact, rather than extrapolating a room-temperature friction result.

Temperature-dependent coating evidence extends, rather than replaces, the bulk Ni comparison. Torres et al. examined self-lubricating Ni-based laser claddings from room temperature to 600 °C, with soft-metal and dichalcogenide additions. Processing and service can transform the nominal lubricant into other sulfide or oxide phases, so retention of the starting powder is not the only route to lubrication. The relevant question is whether the evolving surface chemistry sustains low shear and adequate cohesion across the intended temperature interval [85].

An alternative architecture is nanocrystalline Inconel 718 containing solid lubricants introduced by powder mixing and high-pressure torsion (HPT). Kasalo et al. compared several lubricant additions and counterfaces; functionalized CNTs provided a particularly favorable ambient-temperature response, while the effectiveness of other additives

depended on contact conditions [75]. The result couples matrix refinement with lubricant integration. It therefore complements, rather than duplicates, the high-temperature CaF_2 system: severe plastic deformation establishes the starting load-bearing architecture, whereas elevated-temperature sinters additionally rely on the thermal stability and mobility of the lubricating phase.

4.3.5. Cross-Matrix Comparison

Accordingly, a hardness-only window can differ from a strength–elongation, wear–corrosion, or conductivity-constrained wear window. These differences are part of the design problem rather than exceptions to a common concentration law. Section 5.4 organizes the relevant geometry, processing, and endpoint distinctions.

The matrix comparison therefore separates three useful design variables: constituent selection, interfacial conversion, and spatial architecture. Al and Mg highlight the competition between compactability and particle support; Cu emphasizes continuity of electrical and thermal pathways; Ti shows how architecture and reaction can be used to preserve deformation capacity; and Fe/Ni systems emphasize phase evolution under load and temperature. These differences explain why a common nominal reinforcement percentage cannot be transferred between matrices. A service constraint should first define the required response, after which the processing route is selected to establish the relevant interface and defect state [11,29,32,58,69,73].

5. Reinforcement Chemistry, Content, and Interface Engineering

Reinforcement design couples chemistry, retained geometry, spatial distribution, and interfacial response. Sections 3 and 4 establish how these descriptors arise during processing and vary with the matrix. The following comparison uses them to distinguish reinforcement families, define property-specific feasible windows, and connect measurable interfaces to engineering selection [8,11,23].

5.1. Ceramic Reinforcements

Rigid ceramics share load and resist local deformation when retained in a sufficiently continuous matrix. Volume, spacing, shape, and interfacial support matter alongside intrinsic hardness. For micrometer-scale particles, matrix constraint and load sharing are more defensible initial explanations than an unquantified assertion of dominant Orowan strengthening [8,11,12].

Refinement raises potential obstacle density but also increases surface/oxide sensitivity and interface-controlled transport resistance. Angular particles can create stronger stress concentrations, while elongated features introduce orientation dependence. The largest agglomerates may govern fracture even when the mean primary-particle diameter is small. A “nano” designation alone therefore does not predict the optimal fraction [12,27,30].

Reinforcement retention controls the contribution of hard particles during sliding. Intact particles support local load, fractured particles alter contact geometry, and detached particles enter the third-body population. Consequently, an increase in hardness can coexist with higher wear when interface debonding supplies abrasive debris. Worn-surface and subsurface observations distinguish these failure paths, while dedicated mechanical measurements establish the strength of the corresponding interface [8,13,110].

A ceramic particle can fail internally, debond from the matrix, or remain intact while the surrounding metal yields. These alternatives depend on particle size, shape, flaws, and interface constraint. Angular particles can increase local stress concentration, while larger particles may contain a different flaw population from nanoscale dispersoids. The fatigue response of size-controlled SiC/Al demonstrates why the active failure event

should be identified rather than assigning all ceramic effects to Orowan strengthening. For micrometer-scale particles, load support, constraint, grain structure, and damage initiation generally provide the more relevant first interpretation [12,27,43].

5.2. Carbonaceous Reinforcements

Graphene/graphite are sheet-like, CNTs elongated, and GO/rGO chemically and structurally distinct. Sheet thickness and lateral size or tube length/diameter must be retained when comparing content. Equal carbon wt.% does not establish equivalent contact area, alignment, structural integrity, or conductive connectivity [1,9,23].

High intrinsic carbon conductivity does not guarantee increased bulk conductivity. Oxide-bearing contact, defects, agglomeration, and interrupted metal paths can offset the reinforcement's properties. Alignment may improve one direction while leaving the transverse response less favorable. The consolidated material must therefore be measured in the intended direction and thermal state [30,51,52].

Dispersion improvement can coexist with carbon fragmentation or oxygen retention. A milling/chemical route that maximizes hardness may not maximize conductivity. Density, carbon structure, distribution, and transport should be characterized on the same final material condition rather than combined from separately optimized stages [38,53,54].

For tribology, carbon-rich debris, a film in the specimen track, and an adherent counterface transfer film are different states. Evidence should identify location, composition, coverage, and persistence. A low COF is not by itself proof that a stable graphitic film caused the wear improvement [13,14,23].

The carbon–metal boundary can be tuned chemically and geometrically, but these adjustments are not equivalent. Increasing embedded length improves the opportunity for stress transfer; adding chemical bridges can alter local adhesion or heat flow; and reducing sheet thickness changes both interface area and conduction anisotropy. Direct CNT pull-out and graphene–metal thermal measurements demonstrate different boundary functions. An interface optimized for tensile stress transfer need not minimize thermal resistance, and a treatment that improves initial wetting may damage the carbon structure. These functions therefore require their own measured descriptors [33,98,101].

5.3. Hybrid Reinforcement Strategies

Hybrid design combines reinforcement functions within a shared microstructure. A rigid phase can support contact load, a low-shear phase can accommodate sliding, and chemical modification can integrate both with the metallic matrix. The resulting performance depends on phase location and connectivity as well as composition. Mechanically useful hybridization therefore includes both complementary property contributions and architectural interactions that distribute deformation or modify transport [10,28,38,46,48].

The practical advantage of a hybrid is the property combination it delivers under the relevant constraints. A ceramic–carbon composite can be useful even when its hardness is below that of a ceramic-only specimen, provided friction or conductivity is improved without unacceptable loss of load support. Conversely, combining two individually beneficial additives may create reinforcement-rich clusters that impede densification. Comparisons at matched matrix state and total reinforcement volume reveal whether the interaction is beneficial or simply reflects a change in density or constituent fraction [10,28,48,60].

The bioinspired Al/graphene/Al_2O_3 architecture illustrates a geometrical interaction: platelet organization and interlocking coordinate stiff reinforcement with deformable metal, enabling strength and toughness to be considered together [46]. Designed TiB networks and heterogeneous Mg architectures apply a related principle at different length scales [32,65]. These systems establish that controlled nonuniformity can be functional.

The distinction from harmful agglomeration is the preservation of intended load paths and deformable matrix regions, not uniformity as an end in itself.

5.4. Reinforcement Content and the System-Specific Optimum Window

The reinforcement window comprises the compositions and processing states that satisfy the required property combination. Its boundaries depend on matrix condition, particle geometry, dispersion, consolidation, and service environment. A measured response may rise throughout the sampled range, reach an interior maximum, or favor different fractions for different endpoints. The largest tested value therefore characterizes the experimental range, whereas an interior optimum additionally requires an observed deterioration on either side.

The evidence contains rising hardness over a tested PM Al2024–B_4C range, a best-performing tested 5% condition in a casting comparator, and a highest-tested-loading endpoint in GO/Cu [14,27,34]. Mg–graphene adds a conflict between wear and corrosion [26]. These responses differ because their matrices, geometries, routes, and constraints differ, not because they must fit one universal peaked curve.

Size shifts the window through interfacial area, spacing, surface reactivity, and consolidation. For platelets/fibers, aspect ratio and alignment also alter load paths and transport connectivity. A content determined for one diameter or orientation cannot be transferred simply by retaining wt.%. Final cluster dimensions can be more relevant than feedstock dimensions when agglomeration persists [12,30,51].

With competing objectives, the feasible region is bounded by minimum strength or conductivity, maximum allowable wear or corrosion, and required ductility or fracture resistance. Within this region, a non-dominated composition cannot improve one objective without sacrificing another. This interpretation accommodates different preferred fractions for hardness, friction, fatigue, and environmental performance without forcing unlike measurements into an arbitrary weighted score.

Figure 4 illustrates the competition between reinforcement-associated benefits and defect accumulation. Table 3 compares the matrix, particle geometry, route, and target property that position the useful reinforcement window in representative systems.

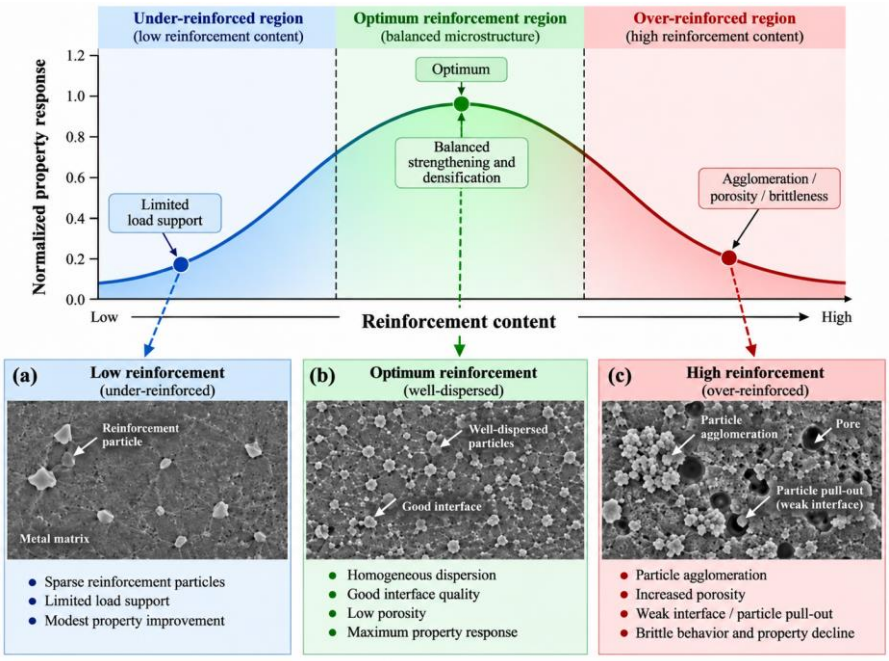

Figure 4. Conceptual effect of reinforcement content on material properties: (**a**) low reinforcement; (**b**) optimum dispersion; (**c**) excessive reinforcement and defect accumulation. Colors and arrows indicate the corresponding regions and microstructures [12,14,26–28,34].

Table 3. Matrix-, geometry-, processing-, and property-dependent reinforcement windows in representative MMCs.

System/Source	Dimensions and Tested Content	Route/Target	Supported Inference
Al2024–B_4C [27]	d_{50} = 5 and 49 μm; 0, 5, 10, 20 wt.%	Milling/PM; hardness and density	Hardness increases over the tested range. Size/content/milling interact; density change is not solely porosity.
Al–CNT [40]	High-aspect-ratio CNTs; concentration series	Ball milling and hot extrusion; mechanical response	Fraction alone does not characterize dispersion. Retained length and cluster size are needed for a transferable threshold.
Al6061–B_4C/BN [28]	2–8 wt.% B_4C plus 2 wt.% BN; size effect not independently isolated	200–800 MPa; 400–600 °C; hardness/compression	8 wt.% B_4C at 800 MPa/600 °C is the best tested endpoint, despite reduced compressibility with content.
Al7075–B_4C [34]	0, 1, 3, 5, 7% series; matched size-effect series NR	Stir casting, non-PM comparator; hardness/wear	The cited 5% result is confined to its alloy and casting history; not a generic PM optimum.
Cu–GO [14]	0.5, 0.75, 1 wt.%; final sheet-size distribution NR	PM/hot pressing; hardness, loss, COF	1 wt.% is the highest tested content and best reported endpoint; an interior peak is not established.
Cu–graphene [24,51]	Aligned versus dispersed architectures; composition basis specific to each study.	Directional thermal transport/corrosion	Alignment and exposure can change the preferred fraction; wt.% alone cannot transfer the optimum.
Mg–graphene [26]	0.1, 0.25, 0.5 wt.%; partial agglomeration at upper content	Semi-PM; wear and corrosion	Best tested wear and corrosion response do not coincide; environmental performance is a separate constraint.
Ti–carbon fiber [29]	Discontinuous fibers; reaction changes remaining geometry	Heat treatment; interface and mechanical response	A useful reaction window depends on layer growth and retained geometry, not a universal content or thickness.
PM 2024 Al–SiC [43]	10 wt.% SiC; average sizes 5, 20, 60 μm	Rotary-bending fatigue	5 μm improved fatigue; the 20 μm benefit depended on stress level; 60 μm decreased fatigue strength.
AZ91D–Ni/graphene nanoplatelets (GNP) [60]	1.5 wt.% Ni with a 0–2 wt.% GNP series	SPS at 500 °C, 50 MPa, 5 min; mechanical/wear response	A favorable upper tested endpoint is not a bracketed global optimum.
Mg–graphene [64]	0.15 wt.% favorable content in the studied process design	600 MPa compaction; 520 °C/60 min sintering	Preferred content is conditional on pressure, thermal schedule, and matrix.
TiB-whisker/Ti [32]	8.5 vol.% network-reinforced condition	In situ/PM architecture; tensile response	Designed connectivity can preserve deformation; not all nonuniformity is agglomeration.
TA15–TiB [68]	0–4 vol.% TiB; colony and prior-β grain refinement	PM hot pressing; tensile response and fracture	1 vol.% improved tensile properties but reduced fracture toughness; the preferred content depends on damage criterion.

Ni/NiCrSiB–CaF_2 [74]	20 wt.% CaF_2 formulation	PM; dry sliding from 23 to 600 °C	Lubricant spreading and oxidation change with temperature; the useful response is an operating interval.

The Al fatigue, Mg wear–corrosion, and diamond/Cu thermal examples occupy different regions of this design space. Their preferred fractions differ because the relevant interfacial area, constituent density, loading mode, and functional requirement differ. A low carbon fraction can strongly modify a conductive or electrochemically active boundary, whereas a heat-spreading diamond architecture may require a large reinforcement volume. Composition is therefore interpreted together with the structural feature through which it acts [26,43,56,64].

5.5. Matrix–Reinforcement Interface

The interface transmits stress and heat, affects charge transport, and can provide a crack or corrosion path. The target is sufficient integrity and suitable transport without an unacceptable brittle or resistive layer, not maximum chemical reaction or bond strength in isolation [8,29,30].

A reaction layer should be described by phase, thickness distribution, continuity, crystallography, and position relative to damage. One favorable thin layer does not establish a critical thickness. Such a threshold requires controlled growth and an associated transition in fracture or transport. A continuous-looking SEM boundary establishes contact at that resolution, not atomically clean bonding [8,29].

Al–SiC and Ti–carbon illustrate different reaction problems. Al–C products can compromise environmental or mechanical stability, whereas TiC development can improve contact while consuming the original carbon geometry. The useful reaction extent must be determined for its chemistry and thermal history rather than transferred between matrix systems [8,29].

In B-containing 316L, Fe_2B/FeB formation identifies a hard-phase pathway [69]. Discrete and continuous distributions can have different effects on damage tolerance. Phase detection therefore needs fraction, morphology, and crack-path evidence before it supports a quantitative interface-strengthening rule.

Cu–carbon illustrates a possible mechanical–transport conflict. An oxide/reaction interlayer can affect contact while increasing resistance. Thermal boundary resistance is $R_k = \Delta T/q$, where q is heat flux, with units $m^2 \cdot K/W$; it is not the reciprocal of bulk thermal conductivity. A resistance obtained by fitting an effective-medium model is model-derived unless independently measured [23,30].

Single-reinforcement tests can connect boundary mechanics to composite models. Zhou et al. measured an interfacial shear strength of 24.8 ± 3.2 MPa by in situ pull-out of selected multi-walled carbon nanotubes (MWCNTs) from an Al matrix. The experiment involved six selected nanotubes, not six independently fabricated composite batches. Its value is the direct interface-sensitive measurement and the connection to shear-lag analysis. The stated uncertainty is retained as reported rather than recast as a population confidence interval. Such measurements allow load-transfer models to use an observed boundary parameter instead of a fitted value chosen solely to reproduce bulk strength [98].

Mechanical integrity and thermal coupling need not respond identically to interlayer formation. Monachon and Weber measured the thermal boundary conductance of refractory-metal/diamond contacts before and after carbide-forming annealing. Despite substantial conversion of interfacial material, the conductance did not increase significantly in the examined systems [106]. The finding complements the high-conductivity diamond/Cu composites: creating a carbide phase can establish chemical compatibility, but

the resulting heat transfer also depends on the initial boundary, layer thickness, and transport across the newly formed interfaces.

For an ideal straight cylindrical reinforcement under a simplified shear-lag balance, the critical transfer length scales as $l_c \approx \sigma_f d_f/(2\tau_i)$, where σ_f is reinforcement tensile strength, d_f its diameter, and τ_i an effective interfacial shear stress. The expression clarifies why milling-induced shortening can offset stronger bonding. For hollow multi-walled nanotubes, the active wall area, interwall sliding, orientation, and end conditions require additional treatment; for platelets, a different geometry is necessary. This scaling is used here to identify required measurements, not to calculate unmeasured reinforcement strengths or to equate all carbon morphologies [98–100].

5.6. Quantitative Interface Characterization and Measurable Descriptors

Quantification links a technique to a descriptor and spatial scale. Cross-sectional transmission electron microscopy (TEM) or scanning transmission electron microscopy (STEM) resolves layers and local structure; EDS and electron energy-loss spectroscopy (EELS) probe chemistry; EBSD provides grain/orientation information; and tomography distinguishes pore topology. These answer different questions and are not interchangeable demonstrations of "good bonding" [8,29].

Instrumented indentation provides local hardness and modulus when contact geometry, pile-up/sink-in, and substrate influence are addressed [31]. An indent crossing multiple phases is a mixed response. Push-out/push-in, micropillar, or microcantilever measurements can probe interface-associated failure with suitable geometry and a justified mechanical model. Scratch critical load is a test-specific failure metric, not a universal adhesion energy.

A distribution is preferable to one selected interface. Reporting should identify fields, particles/interfaces, independent specimens, selection method, resolution, and central value/spread. Thickness in nm, bonded-perimeter fraction, cluster fraction, strength in MPa, fracture energy in J/m^2, and thermal resistance in $m^2 \cdot K/W$ test different links to performance. Table 4 organizes the method–descriptor–interpretation relationships.

Method limitations constrain inference. EDS enrichment does not alone establish oxidation state or bond type; XRD can miss thin, amorphous, or low-fraction products; Scherrer estimates describe coherent crystallites rather than metallographic grains. When a discriminating descriptor is unavailable, a mechanism remains correlative or interpretive rather than becoming an assumed numerical contribution [8,29,31,41].

Table 4. Quantitative interface descriptors, measurement methods, and the physical quantities constrained by each technique.

Descriptor and Units	Suitable Measurement	Question Tested	Interpretation Boundary
Reaction-layer thickness/continuity (nm; fraction)	Cross-sectional transmission electron microscopy (TEM), scanning TEM (STEM), local diffraction, EDS, and electron energy-loss spectroscopy (EELS) [8,29]	Does reaction progress change fracture or transport?	A thickness distribution across interfaces is needed to distinguish local reaction from a specimen-wide threshold.
Local chemistry/segregation (atomic fraction; spatial profile)	Calibrated STEM–EDS/EELS; X-ray photoelectron spectroscopy (XPS) for accessible surfaces [8,29]	Is a chemically distinct boundary present?	Elemental enrichment alone does not determine bonding or oxidation state.

Reinforcement geometry (μm or nm; aspect ratio)	SEM/TEM image analysis with declared segmentation [27,41,97]	Are the active obstacles particles, sheets, fibers, or clusters?	Final retained dimensions, their distributions, and section orientation determine the operative geometry.
Dispersion (cluster fraction; spacing; field variability)	Representative image statistics; tomography where appropriate [27,41,53]	Does mixing improve uniformity independently of density?	Two-dimensional sections are not automatically representative volumes.
Porosity (fraction; connectivity)	Bulk/true density; cross sections; tomography [90,91]	Is performance controlled by pore closure or connected defects?	Constituent-density changes and reaction products must be separated from pores.
Matrix grain/crystallite size (μm or nm)	Electron backscatter diffraction (EBSD)/TEM for grains; XRD for coherent domains [8,41]	Can a grain-related strengthening estimate be supported?	Crystallite and grain sizes are not interchangeable; texture and method resolution matter.
Local hardness/modulus; interface-associated strength (HV/GPa; MPa)	Instrumented indentation; modeled push-out or micromechanical tests [8,31]	Which phase or boundary carries load and where does failure occur?	Mixed-phase indents, substrate effects, and geometry must be accounted for.
Adhesion/fracture response (MPa; J/m^2 where derived)	Pull-off with failure plane; validated fracture or micromechanical geometry [15,16,31]	Does failure occur in layer, boundary, substrate, or adhesive?	Scratch critical load is not universally an interface fracture energy.
Thermal boundary resistance (m^2·K/W)	Interface-sensitive transport experiment or calibrated model [30]	Does the boundary limit heat flow?	Bulk conductivity alone does not uniquely identify R_k; fitted values are model-dependent.
Tribofilm/transfer-film state (thickness, coverage, chemistry)	Both contact surfaces, cross sections, Raman/XPS and debris analysis	Does a persistent low-shear layer accompany lower loss?	COF or SEM appearance alone does not identify film composition or causal action.
Carbon structural integrity (intensity ratio, band width, excitation energy)	Raman spectra at declared excitation and fitting conditions [101]	Does dispersion processing alter the retained carbon structure?	Defect regime and excitation dependence prevent a universal linear damage calibration.

Thermal boundary experiments offer a parallel quantitative test. Jiang et al. combined X-ray photoelectron spectroscopy (XPS) with time-domain thermoreflectance (TDTR) and reported an approximately 55% increase in graphene–Cu interfacial thermal conductance at an intermediate oxygen functionalization state, with a peak near an O/C atomic ratio of 7.7%. The composition describes interface chemistry, not a 7.7 wt.% reinforcement fraction. This direct boundary measurement supports oxygen-mediated coupling, but does not by itself specify the effective conductivity of a porous or randomly oriented bulk Cu/graphene compact [33].

Instrumented indentation adds spatially resolved hardness and modulus but requires a separation of contact size, phase dimensions, and substrate influence. The Nix–Gao size-effect relation, $H^2/H_0^2 = 1 + h^*/h$, illustrates why hardness can increase as penetration depth h decreases even in a single crystalline material; h* is a characteristic length, not a reinforcement fraction. Consequently, a nanoindentation map cannot be directly compared with macrohardness without scale information. Similarly, the Williamson–Hall treatment separates size- and strain-related diffraction broadening within its assumptions,

but its coherent-domain size is not automatically the metallographic grain size [31,102,114].

Table 5 places these quantitative interface-related examples beside their measurement scale and engineering interpretation. The key distinction is between a measured local quantity, a measured bulk response, and a model-derived parameter. A boundary conductance, an interfacial shear strength, and a composite thermal conductivity answer different questions; their numerical magnitudes are not interchangeable measures of "interface quality".

Table 5. Representative interface-sensitive measurements and their implications for mechanical and thermal coupling.

System/Study	Measurement and Result	Evidence Scale	Design Implication
Multi-walled carbon nanotube (MWCNT)/Al [98]	In situ single-tube pull-out: 24.8 ± 3.2 MPa interfacial shear strength	Six selected nanotubes; local interface strength with reported uncertainty, rather than batch-scale variability.	Measured boundary stress can constrain a geometry-appropriate load-transfer model.
CNT/Al [99,100]	In situ tensile observation of pull-out, wall sliding, or nanotube fracture	Direct deformation observations; composite geometry and orientation remain relevant	Distinguishes transfer and reinforcement failure from an inference based solely on hardness.
Graphene/Cu boundary [33]	TDTR: approximately 55% conductance increase at intermediate oxygen functionalization	Direct boundary-transport experiment; peak near 7.7% O/C atomic ratio	Boundary chemistry is not a bulk reinforcement fraction or a bulk conductivity measurement.
Ni-decorated graphene/Cu [55]	216.2 W/(m·K); shear strength 56.3 MPa at reported 0.1 wt.% addition	Bulk responses; gains relative to the same-study sintered Cu-nanoparticle control	Improved coupling can benefit transport and mechanics without implying performance above annealed bulk Cu.
W-modified diamond/Cu [56]	640 W/(m·K) at 50 vol.% diamond	Measured bulk conductivity; interface conductance interpreted with models	High-volume-fraction composite; fitted boundary conductance remains model-dependent.
Instrumented indentation/diffraction [31,102,114]	Load–displacement response; size and strain contributions to peak broadening	Method-dependent local mechanics and coherent-domain descriptors	Indentation hardness is not interface shear strength; coherent domains are not automatically metallographic grains.
Al/SiC [104,105]	In situ cooling observations of dislocation generation near reinforcement	Direct microscopy of thermal-mismatch deformation	Supports mismatch-induced dislocations; retained strengthening additionally depends on recovery.
Cr, Mo, Nb, W/diamond [106]	As-deposited conductance: 315, 220, 220, 205 MW/(m^2·K), respectively	Time-domain thermoreflectance before and after 800 °C/2 h annealing	Carbide conversion did not significantly change conductance in these thin-film systems.

5.7. Reinforcement Selection as a Multi-Objective Design Problem

Application-specific selection begins with the dominant function, mandatory secondary-property thresholds, and the service environment. A Cu contact couples electrical transport with contact heating, Mg components require both structural integrity and environmental stability, and a hard coating depends on adhesion and substrate support over the required functional depth. These constraints define the feasible architecture before reinforcement fraction is optimized [23–26].

The feasible design region contains compositions that satisfy all mandatory property thresholds. Within this region, normalized responses reveal trade-offs, whereas absolute values determine suitability for the component. This constrained formulation prevents a large hardness gain from compensating mathematically for unacceptable conductivity, brittleness, or environmental degradation.

An engineering interface specification consequently combines geometry, chemistry, and function. For a mechanically loaded boundary, useful descriptors include bonded area, reaction-layer continuity, and the location of crack initiation. For a thermal boundary, conductance and layer resistance are required in the direction of heat flow. For an environmentally exposed boundary, electrolyte access and local electrochemical activity become decisive. The same processing treatment may improve one specification while degrading another, which explains why interface optimization is most effectively linked to an explicit service function [29,30,33,98,106].

A useful multi-objective decision also includes robustness. Two formulations with similar mean wear may differ in variability, sensitivity to milling, or the width of their acceptable sintering window. A broader feasible processing window can be preferable to a sharply peaked laboratory optimum, especially for larger components with temperature or density gradients. The selected material should therefore satisfy the target across realistic manufacturing tolerances, rather than only at a fitted optimum. This shifts optimization from one maximum response to a reproducible combination of properties and process margins [4,44,64,96].

6. Comparative Mechanical, Tribological, and Functional Performance

Comparative interpretation combines within-study normalization with the physical meaning of the measured endpoint. Hardness ratios use controls measured on the same indentation scale and load, while wear data retain the distinction among mass loss, volume loss, and specific wear rate. Dimensionless ratios express the magnitude of a change within its processing and testing context; the accompanying protocols establish the conditions under which different material responses can be compared.

6.1. Hardness and Strength

Hardness integrates local deformation, phase distribution, porosity, and indentation scale. It is not tensile or interfacial strength. A reinforced material can gain hardness while losing elongation or fracture resistance. Where available, strength and ductility are therefore retained together rather than ranked using indentation alone [8,58].

The fixed-1-wt.% B_4C/Cu means give RH = 118.24/70 = 1.689 [13], while GO/Cu reports RH = 2.100 [14]. The casting comparator gives 118.41/83.97 = 1.410 [34]. Each quantifies its own control and test scale, not an intrinsic reinforcement ranking across matrices or routes.

Absolute endpoints and normalized changes provide complementary information. The 184 HV Al6061–B_4C/BN and 171.53 HV SPS Al–SiC conditions locate experimentally achieved processing–property combinations. Their interpretation follows the measured

final state, whereas a reinforcement-induced fractional gain additionally requires a directly matched reference condition [28,41].

Strength and damage tolerance require independent attention. Hardness samples a confined deformation field; tensile elongation reflects strain localization and damage accumulation over a gauge volume, and fatigue depends strongly on initiation sites and cyclic driving force. The TiB/Ti network example combines strength improvement with 11.8% elongation, whereas the Al–SiC fatigue series changes ranking with particle size and stress level. Neither outcome is recoverable from hardness alone. Therefore, structural screening should include at least one damage-sensitive endpoint alongside indentation, with density, matrix heat treatment, and specimen orientation retained [32,43].

6.2. Wear Resistance and Unit Harmonization

The preferred common measure is specific wear rate $k = \Delta V/(F_N L)$, in $mm^3/(N \cdot m)$, where ΔV is volume loss, F_N normal load, and L distance. A result in mm^3/m is divided by the associated load only when that load is unambiguous. Scar width and reciprocal wear resistance cannot automatically be converted to k.

Mass-to-volume conversion uses $\Delta V = \Delta m/\varrho$; mg divided by g/cm^3 yields volume numerically in mm^3. It assumes representative removed material. Selective binder loss, reinforcement-rich debris, or oxide formation may invalidate a bulk-density conversion. The density and assumption should therefore accompany every converted value; otherwise the original loss unit is retained.

The Al7075–B_4C comparison remains in mm^3/m because the summarized endpoints cannot be assigned uniquely to one load; its ratio is 0.572 [34]. GO/Cu supplies a stated loss decrease, giving 0.171 [14]. Neither is relabeled as an absolute $mm^3/(N \cdot m)$ endpoint without the necessary metadata.

Compatibility also requires counterbody material/radius, geometry, roughness, lubrication, environment, and treatment of running-in. Mean COF needs its averaging interval, while wear should distinguish cumulative from steady-state response. A lower value under a different protocol does not establish the better material for a particular contact.

The distinction between specific wear rate and the dimensionless Archard coefficient is also important. In the idealized relation $\Delta V = K\ FN\ L/H$, K is dimensionless when all quantities use a consistent unit system, whereas $k = \Delta V/(FN\ L)$ has dimensions of volume per load–distance. Thus, $k = K/H$ only under the assumptions of that model and compatible units. Increasing hardness need not reduce k proportionally when the operative wear mechanism, counterface damage, or third-body layer changes. Source-normalized wear ratios are therefore more defensible than imposing an inverse-hardness law across unlike contacts [115].

6.3. Coefficient of Friction, Tribofilms, and Transfer Films

A tribofilm develops on the specimen surface through deformation, mixing, oxidation, or reaction. A transfer film is deposited on the opposing body. A third-body layer participates in contact without necessarily remaining attached. These terms describe location and evolution, not one obligatory chemical composition.

Reduced COF in hBN- or carbon-containing systems is compatible with a low-shear contribution, but chemistry and counterface coverage are needed to identify the film. SEM morphology alone cannot distinguish graphitic material from an oxide-rich mechanically mixed layer. Interpretations must match the measurements actually reported [13,14,111].

Low friction does not guarantee low wear. Easy shear can facilitate removal, and a hard reinforcement can protect the specimen while abrading the counterbody. Both

surfaces, debris, film persistence, and friction evolution complement the material-loss endpoint. Section 6.8 develops the corresponding mechanism tests.

A chemically identified film can distinguish a reaction-assisted mechanism from simple mechanical smearing. The NiMoAl study links an improved contact response to Ag_2MoO_4- and Al_2O_3-containing surface products, while temperature-dependent laser-cladding work shows that lubricant precursors can transform during deposition or sliding. These observations motivate time-resolved interruption tests: characterize the track and counterbody before, during, and after the transition to a stable friction regime. Film coverage, chemistry, and debris production can then be related to the interval over which material loss decreases, rather than inferred from the final worn surface alone [73,85].

6.4. Strength–Wear–Conductivity Trade-Off

Conductivity is a constraint in many Cu applications. Units, temperature, direction, and processed control are retained. Thermal conductivity cannot be inferred solely from electrical conductivity when interfaces, defects, phonons, and anisotropy change. The continuous Cu network and carbon architecture require direct assessment [23,24,30,51–54].

The arc-induction conductivity ratio of 20/19 = 1.053 accompanies improved hardness in that source [35], whereas the blending study emphasizes preservation of conductivity through processing control at low GO content [53]. These are different design observations, not evidence that one route universally dominates. Table 6 separates material state, endpoint, control, normalization, and reporting limits.

Table 6. Published mechanical and tribological endpoints and within-study normalized responses. Ratios retain the control material, material state, and original measurement basis.

Material/Route/Source	Reported Endpoint and Control	Derived Ratio	Protocol or Statistical Boundary
Cu–1 wt.% B_4C/PM [13]	Hardness: 70 → 118.24 HV0.3	R_H = 1.689; +68.91%	Matched PM Cu control; HV0.3. The ratio describes the reported mean endpoints.
Cu–1 wt.% B/PM [13]	Hardness: 70 → 116.50 HV0.3	R_H = 1.664; +66.43%	Shared Cu control; not independent of other ratios in this series.
Cu–1 wt.% graphite/PM [13]	Hardness: 70 → 114.78 HV0.3	R_H = 1.640; +63.97%	Different geometry/volume at equal mass fraction; not chemistry-only isolation.
Cu–1 wt.% Al_2O_3/PM [13]	Hardness: 70 → 113.25 HV0.3	R_H = 1.618; +61.79%	Shared processed-Cu control; dependent within-series comparison.
Cu–1 wt.% GO/hot pressing [14]	Reported changes: hardness +109.97%; loss −82.88%; COF −51.33%	R_H = 2.100; R_{loss} = 0.171; R_μ = 0.487	Relative hardness, material-loss, and friction changes under the reported test conditions.
Cu–1 wt.% rGO/arc induction [35]	65 ± 4 → 225 ± 3 HV30; 19 → 20 MS/m	R_H = 3.462; R_σ = 1.053	Five indentations per specimen; reported measurement uncertainty. Non-PM comparator.

Al7075–5% B_4C/casting [34]	83.97 → 118.41 HB; 9.124 × 10^{-3} → 5.223 × 10^{-3} mm^3/m	R_H = 1.410; R_{loss} = 0.572	Non-PM. Endpoint-to-load association NR; no conversion to $mm^3/(N·m)$.
Al–10 wt.% SiC/milling + SPS [41]	171.53 HV	Absolute endpoint; no matched-control ratio	Does not establish tensile strength or separate mechanism increments from this hardness endpoint.
Al6061–8 wt.% B_4C–2 wt.% BN/PM [28]	184 HV; compressive strength 249 MPa	Not normalized	800 MPa compaction; 600 °C sintering. Best tested combination, not a universal optimum.
AZ91–5 wt.% TiB_2/vacuum milling + hot pressing [58]	Ultimate tensile strength 234 MPa; yield strength 91 MPa; elongation 7.3%	Not normalized	A tensile-property combination; no wear/corrosion optimum is inferred.
Cu–0.49 vol.% rGO/precursor route [54]	Yield strength 553 MPa; thermal conductivity 364 W/(m·K)	Not normalized	Room-temperature reported endpoints. Rolled and unrolled conditions are not merged.
Cu–0.5 wt.% graphene [24]	Charge-transfer resistance 1705 $Ω·cm^2$	Not normalized	Study-specific electrochemical model/exposure; not equivalent to corrosion-current density.
NiCrBSi/NiCrBSi–50 wt.% WC–Co coatings [78]	776 ± 4 → 959 ± 5 HV0.1	R_H = 1.236	Reference: the NiCrBSi coating without WC–Co on AZ91D, rather than the bare substrate.
AZ91D–Ni/graphene nanoplatelets (GNP)/SPS [60]	Hardness: 67.4 → 89.7 HV; specific wear: 5.21 × 10^{-3} → 3.85 × 10^{-3} $mm^3/(N·m)$	RH = 1.331; Rk = 0.739; wear reduction 26.1%	10 N wear load; descriptive endpoint ratios for the investigated AZ91D–Ni/GNP series.
Mg–0.15 wt.% graphene/PM [64]	44.34 HV; compression 300 MPa; k = 8.52 × 10^{-4} $mm^3/(N·m)$	Not normalized	600 MPa compaction; 520 °C/60 min sintering. Absolute mechanical and wear response.
TiB-whisker/Ti network/PM [32]	Strength gain 74.6%; elongation 11.8% at 8.5 vol.%	Strength ratio = 1.746	Reported reference state; elongation is an absolute value, not a relative gain.
High-SiC Al/sintering + hot pressing [44]	Maximum tensile strength 343 MPa; reported improvement >70% over sintered-only state	Strength ratio >1.70 (reported lower bound)	Processing-state comparison, not an unreinforced-matrix ratio.
Ni-decorated graphene/Cu [55]	Shear strength 56.3 MPa; reported increase 87.3%	Shear-strength ratio = 1.873	Same-study sintered Cu-nanoparticle reference, not tensile strength or annealed bulk Cu.

Cu–rGO/microwave sintering [57]	71 → 81.1 HV; conductivity 87.10% IACS (International Annealed Copper Standard)	Hardness ratio = 1.142	Wet-milled precursor; argon; matrix heterogeneity influences local hardness.
CNT/Inconel 718/HPT [75]	Best reported 5 wt.% condition: COF 0.78 → 0.14; k ≈ 10^{-6} $mm^3/(N·m)$	COF ratio ≈ 0.179	Ambient reciprocating tests; k converted from ≈10^{-9} $mm^3/(N·mm)$. References are matched within deformation/test sets.

Electrical design also separates bulk resistivity from constriction and film resistance at a contact. A highly conducting substrate does not prevent a resistive oxide or poorly bonded surface layer from controlling contact heating. For current-carrying sliding components, the relevant response includes contact voltage, current density, temperature rise, wear, and the stability of the surface layer. Reinforcement-induced hardening can reduce deformation while simultaneously changing real contact area. Accordingly, bulk conductivity retention is necessary but may be insufficient for choosing between a Cu MMC and a coated Cu substrate [23,35,49,115].

6.5. Thermal Transport and Directional Interface Effects

A mechanically effective interface can still produce a substantial temperature drop. Effective-medium modeling explicitly includes interface resistance and reinforcement shape/size [30]. The scale $R_k\kappa_m/a$ compares boundary resistance with matrix conduction over feature dimension a; it increases as a decreases at fixed R_k and κ_m. This explains why nanoscale addition does not automatically improve heat transport despite a highly conductive constituent.

Gao et al. consider mechanical and thermal properties together [52], while Chu et al. deliberately form an aligned graphene architecture [51]. Dispersion/contact and directional connectivity are different design variables. A valid comparison retains fraction, density, temperature, and heat-flow direction; in-plane and through-thickness conductivity are distinct endpoints.

The copper-formate-derived composite combines 553 MPa room-temperature yield strength with 364 W/(m·K) thermal conductivity at 0.49 vol.% rGO [54]. These jointly reported properties describe a particular precursor and consolidation state. Rolling subsequently changes the architecture, so the property combination is associated with the tested state rather than assembled from separate processing optima. This linkage is essential when selecting a structural heat-transfer component.

Bulk thermal conductivity integrates matrix transport, reinforcement transport, pore resistance, and the thermal boundaries between phases. A thin interlayer can improve contact while adding its own series resistance. For a planar layer, the resistance per unit area scales as t/κ_i, where t is layer thickness and κ_i its conductivity; the two adjoining boundaries contribute additional resistances. Reducing a contact gap may therefore be beneficial even when the interlayer is less conductive than the matrix, but continued layer growth need not remain beneficial [30,33,106].

Laser-flash analysis determines thermal diffusivity from the transient rear-surface temperature response, with conductivity calculated as $\kappa = \alpha\, \varrho\, C_p$, where α is diffusivity, ϱ density, and C_p specific heat capacity [103]. Each term corresponds to the tested composition and temperature. Anisotropic composites require direction-specific interpretation, and porosity or evolving phase fractions can change more than one term simultaneously. Consequently, bulk diffusivity and thermal-boundary conductance provide complementary, rather than interchangeable, information [30,103].

Two independent Cu examples illustrate different meanings of a transport improvement. Nickel-decorated graphene improves the sintered Cu-nanoparticle reference, whereas carbide-modified diamond/Cu achieves a much higher absolute conductivity at a much larger reinforcement volume fraction. The former addresses metal-contact and boundary coupling at low additive content; the latter develops a high-conductivity diamond-containing architecture. These systems should be compared through their design functions, density, mechanical integrity, and heat-flow direction—not through relative percentage gain alone. Expansion mismatch and thermal cycling then determine whether the favorable room-temperature transport is retained in a component [55,56,108].

Thermal expansion and interfacial heat transfer impose a further trade-off in high-volume-fraction heat spreaders. Increasing a low-expansion reinforcement fraction can improve dimensional compatibility with an attached device, while increasing the number of interfaces crossed by heat. Orientation controls whether the heat path preferentially follows a conductive constituent or repeatedly crosses boundaries. The optimum architecture therefore depends on the direction and spatial distribution of heat input, the permitted expansion mismatch, and interface stability under cycling. A high room-temperature conductivity is most useful when these geometrical and thermomechanical conditions remain compatible [30,51,56,106,108].

6.6. Corrosion and Coupled Environmental Performance

Corrosion introduces electrochemical stability in a defined exposure as a separate objective. Conductive additions can alter local cathodic area, while connected pores provide electrolyte access. Matrix chemistry, exposed reinforcement, impurities, surface films, and processing determine the result; hardness or bulk density alone cannot establish a benefit [24–26].

For graphene/Cu, Wang et al. reported a charge-transfer resistance of 1705 $\Omega \cdot cm^2$ at the 0.5 wt.% condition with the most favorable corrosion response in their series [24]. This electrochemical resistance reflects the exposed material and the fitted response under the reported conditions. It differs physically from thermal boundary resistance and cannot be converted directly into corrosion current without the corresponding electrochemical model and parameters. The result links protection to the composite surface state rather than to carbon fraction alone.

The Mg evidence provides a cross-property boundary: wear improvement can accompany corrosion deterioration, while salt-fog and high-humidity rankings can differ [25,26]. A dry indoor contact and chloride-exposed component therefore need not select the same reinforcement content even when the initial hardness ordering is identical.

Corrosion endpoints probe different aspects of degradation. Polarization measurements describe electrochemical kinetics over the tested potential range; impedance resolves frequency-dependent resistance and capacitance; mass loss and hydrogen evolution integrate material consumption over time. Their interpretation depends on electrolyte concentration and pH, temperature, aeration, surface preparation, exposed area, and stabilization history. In a coated composite, wear-induced defects and thermal-cycle cracks additionally determine when the underlying matrix becomes electrochemically accessible [24–26,84].

Coated-metal experiments demonstrate why exposure time changes the corrosion conclusion. Prasai et al. reported approximately sevenfold slower electrochemical corrosion of graphene-coated Cu in aerated sodium sulfate solution. Schriver et al., by contrast, found that graphene could worsen long-term Cu oxidation/corrosion under their exposure conditions. These observations address different test histories and defect-mediated electrochemical behavior; they are not interchangeable estimates of one constant protective efficiency. A conductive coating can block transport locally while defects create paths

that concentrate attack, so protection must be assessed over the intended duration and after representative damage [116,117].

The same distinction applies to GO deposited on stainless steel. Mahmoudi et al. varied surface pretreatment and suspension conditions in EPD on 316 stainless steel; the comparatively thin GO layer on an anodized substrate under the selected phosphate-buffered conditions gave better protection than a thicker, more defective layer. This connects coating performance to coverage and defect accessibility rather than thickness alone. Active protection adds another mechanism: inhibitor-containing nanocontainers embedded in hybrid coatings can release protective species at damaged regions. Such chemical recovery is different from restoring the original mechanical cohesion of a cracked coating [84,118].

Table 7 compares thermal and corrosion responses with their reference state and exposure conditions. Heat-spreader selection depends on directional conduction and interface coupling, whereas protective architectures depend on stable coverage and controlled electrochemical activity over time. These functions can favor different phase fractions and interface chemistries within the same matrix.

Table 7. Thermal-transport and corrosion responses of representative composites and coatings, with their material state and comparison conditions.

System/Source	Endpoint or Observed Contrast	Reference/Condition	Application-Specific Inference
Precursor-derived rGO/Cu [54]	Thermal conductivity 364 W/(m·K); yield strength 553 MPa	0.49 vol.% rGO; reported material state retained	The jointly reported strength and conductivity correspond to this state; subsequent rolling defines a separate state.
Ni-decorated graphene/Cu [55]	Thermal conductivity 216.2 W/(m·K); reported increase 105.3%	Reported 0.1 wt.% addition; sintered Cu-nanoparticle control	Large relative gain and high absolute conductivity are different selection criteria.
W-derived carbide/diamond/Cu [56]	Thermal conductivity 640 W/(m·K)	Hot pressing; 50 vol.% diamond; interlayer phase chemistry retained	Supports chemically engineered heat-flow boundaries, not a generic nanoparticle-addition rule.
Graphene/Cu [24]	Charge-transfer resistance 1705 Ω·cm^2	Study-specific 0.5 wt.% condition and electrochemical model	Charge-transfer resistance is not an intrinsic thermal/electrical boundary resistance.
Graphene-coated Cu [116]	Approximately sevenfold slower corrosion	Aerated sodium sulfate; same-study uncoated Cu	A short-duration electrochemical benefit is conditional on exposure and coating integrity.
Graphene-coated Cu [117]	Long-term oxidation/corrosion can exceed uncoated Cu	Different long-duration exposure from the preceding study	Defect accessibility and exposure duration control the protection factor.
AZ91D with graphene derivatives [61]	Carboxylated graphene favored mechanics; graphene favored corrosion in the comparison	0.1 wt.% additions; SPS; reported corrosion exposure	The best mechanical and environmental endpoints can select different carbon chemistry.

EPD GO/316 stainless steel [84]	Thin coating under selected anodized/phosphate-buffered saline (PBS) conditions gave better protection than a thicker defective layer	Pretreatment and suspension conditions varied; PBS: phosphate-buffered saline	Barrier continuity and defect accessibility are more informative than thickness alone.
Cu–rGO/microwave sintering [57]	Thermal conductivity 391.62 W/(m·K)	Wet ball milling followed by microwave sintering in argon	Concurrent hardness and conduction measurements connect oxide-bearing heterogeneity to functionality.
WC–CoCr/HVAF and HVOF [88]	HVAF improved the investigated wear responses; corrosion resistance was similar across coatings	Fine/coarse feedstocks and Al-alloy substrate; multiple degradation tests	Wear improvement and corrosion protection respond to different coating features.

6.7. Measurement Uncertainty and Comparative Interpretation

A property ratio R = X/Y expresses the change between a composite endpoint X and its corresponding reference Y. Its precision depends on the uncertainty of both measurements and on their statistical dependence. Repeated indentations characterize local variability, repeated tracks characterize contact variability, and independently fabricated specimens capture an additional processing contribution. These distinctions are particularly important when reinforcement changes microstructural heterogeneity.

For sufficiently small relative uncertainties, the variance of the logarithmic ratio is approximated by $\mathrm{Var}(\ln R) \approx \mathrm{Var}(X)/X^2 + \mathrm{Var}(Y)/Y^2 - 2\mathrm{Cov}(X,Y)/(XY)$. The covariance term accounts for shared controls or coupled measurements. Ratios based on the same reference are therefore not statistically independent. A larger difference between mean ratios is most persuasive when it also exceeds the uncertainty associated with specimen preparation and testing.

The tabulated normalized responses retain the precision of their supporting endpoints. Where the definition of a reported interval or the independent specimen count is unavailable, the ratio remains a descriptive comparison rather than a significance estimate. The figures provide conceptual illustrations of processing and mechanisms; quantitative comparisons are presented in the text and tables without reconstructed statistical error bars.

Variability also has a microstructural origin. A wide particle-spacing or pore-size distribution can broaden local hardness and increase the probability of an extreme defect governing fatigue or fracture. Mean properties therefore summarize only part of material reliability. For heterogeneous MMCs and coatings, the spatial distribution of defects and the scatter between independent specimens are complementary to the average strengthening or wear response.

6.8. Corroborating Wear Mechanisms Across the Contact

Wear develops through interactions among the specimen, counterface, and third-body population. Grooves identify directional material displacement, but their origin can be detached reinforcement, oxide particles, or counterface fragments. Adhesive transfer is associated with material deposited on the opposing surface, whereas delamination involves subsurface cracking and layer removal. Combining surface chemistry with subsurface morphology differentiates these pathways more effectively than the appearance of a single worn track [13,73,85,115].

Film-assisted interpretation is stronger when a chemically identified layer persists over the interval of favorable friction/wear. Raman spectroscopy and X-ray photoelectron

spectroscopy (XPS) can add chemical-state evidence, while cross sections establish continuity and thickness. A COF decrease alone cannot distinguish a protective film from transient transfer [13,14,111].

Figure 5 compares the principal wear pathways and the role of reinforcement retention. Their relative importance evolves with contact pressure, sliding history, temperature, and the availability of a protective film.

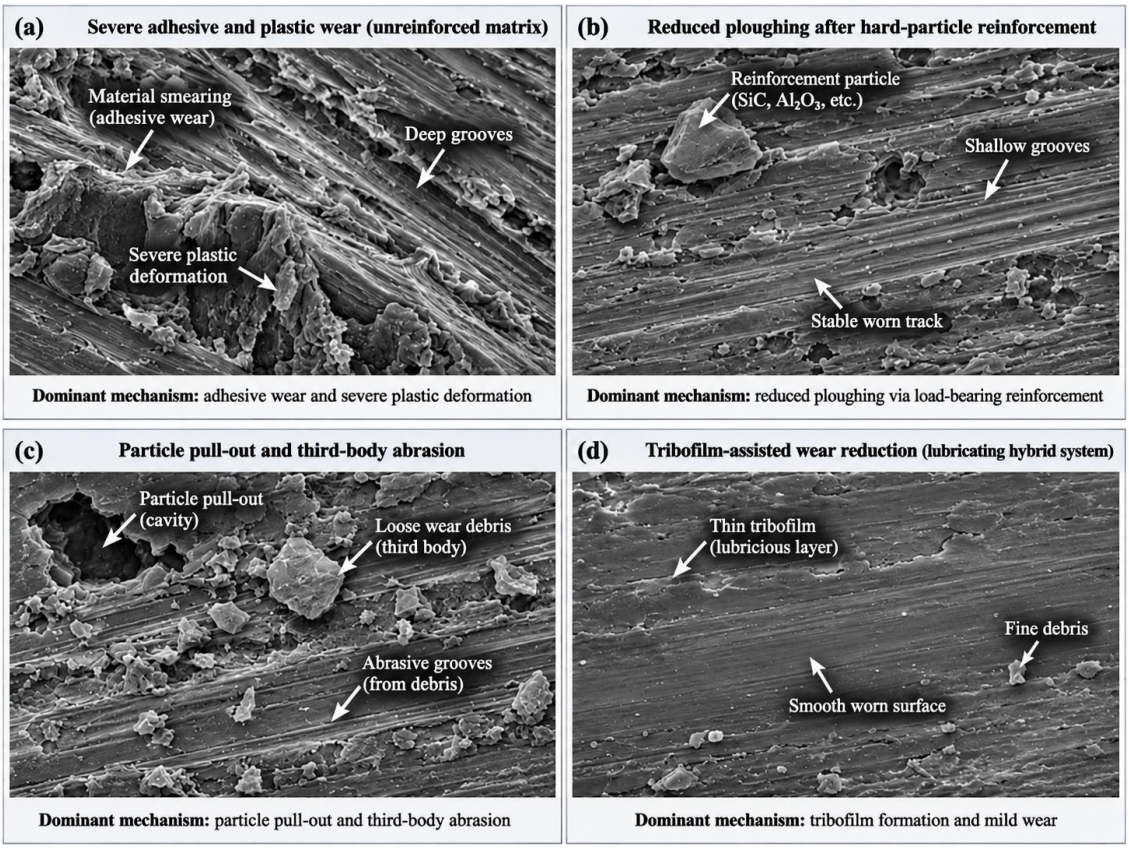

Figure 5. Conceptual illustration of wear mechanisms: (**a**) adhesive wear and plastic deformation; (**b**) reduced ploughing by hard particles; (**c**) particle pull-out and third-body abrasion; (**d**) tribofilm-assisted wear reduction. Arrows indicate representative features [13,14,111].

Wear-mechanism validation is especially valuable when two reinforcements produce similar loss through different pathways. A hard ceramic may reduce specimen penetration but increase counterface abrasion; a softer lubricating phase may reduce interfacial shear while increasing the rate of film renewal. The preferred architecture depends on the total tribosystem, including counterbody replacement and debris sensitivity. Cross-sectional damage depth and chemically resolved counterface deposits complement the schematic modes in Figure 5 and prevent a low specimen-loss endpoint from being treated as complete contact-system optimization [13,73,85,115].

6.9. Fatigue, Fracture, and Temperature-Dependent Reliability

Static strength, indentation resistance, and sliding wear describe different aspects of mechanical performance from cyclic damage and fracture. Reinforcement can reduce matrix deformation while introducing particle-fracture sites or reducing the deformable ligament available ahead of a crack. The balance depends on reinforcement dimensions, interface strength, and the length scale of the applied damage process. This is particularly

important when a composition selected for maximum hardness is intended for a component subjected to repeated contact or tensile cycling [43,68].

The SiC/Al fatigue results distinguish particle-size effects from reinforcement content: at a fixed 10 wt.% fraction, the fatigue behavior differed among 5, 20, and 60 μm particles [43]. Smaller particles reduced the scale of individual damage origins, whereas larger particles altered initiation and crack propagation. The resulting trend demonstrates why the same nominal fraction cannot be transferred between particle-size grades without reconsidering fatigue behavior. Matrix condition and applied stress remain part of that comparison.

In near-α Ti–TiB, monotonic improvements can coexist with reduced fracture resistance. Li et al. reported that the 1 vol.% TiB condition combined improved strength, ductility, and strain hardening with a substantial reduction in mode-I fracture toughness, associated with colony refinement and reduced crack deflection [68]. The contrast separates distributed plastic deformation from resistance to an existing crack. Matrix transformation structure and reinforcement location therefore require different optimization for tensile response and crack propagation.

A structural comparison can be expressed through three linked stages: crack initiation at a particle, pore, or interface; short-crack interaction with the surrounding microstructure; and longer-crack growth through the composite architecture. Different interface modifications can benefit different stages. Increased bonding may delay debonding but transfer damage into a brittle reinforcement, while a compliant or deflecting interface may increase energy dissipation at the expense of initial stiffness. Direct pull-out and in situ deformation measurements establish the local failure mode, and fatigue or fracture testing determines how it influences the full specimen [43,68,98–100].

Temperature-dependent wear adds chemical evolution to this damage sequence. In Ni/NiCrSiB–CaF_2 sinters, the transition toward a smeared lubricating phase and oxidation-associated surface layer changed the dominant contact processes over 23–600 °C [74]. The relevant material state is thus the sliding-generated surface as well as the initial sintered microstructure. Lubricant supply, film retention, and matrix support jointly determine whether low shear is sustained or followed by coating or matrix removal [74,85].

Thermal cycling can additionally change the residual stress produced by matrix–reinforcement expansion mismatch. Dislocations generated during cooling may recover during subsequent exposure, while repeated mismatch strains can initiate interfacial damage. In situ Al/SiC observations establish that cooling-induced dislocation generation is physically real [104,105]; they do not imply that the same dislocation population remains unchanged throughout long-term service. Retained strengthening consequently depends on the balance between generation, recovery, and damage at the operating temperature.

For engineering selection, these effects favor a property envelope rather than a single maximum: adequate yield resistance, acceptable tensile deformation or fracture resistance, controlled fatigue damage, and stable contact behavior across the operating interval. Functional constraints such as conductivity or corrosion resistance are then imposed on the same material state. This approach connects the reinforcement window to reliability and avoids treating an initially favorable hardness ratio as a complete measure of component durability [26,43,56,68,74].

7. Quantitative Links Between Interfaces, Deformation, and Damage

Mechanistic interpretation connects processing to a measurable intermediate structure and then to the observed property. The decisive quantities include reinforcement connectivity, grain and dislocation structure, boundary strength, reaction-layer topology, and pore geometry. Their combined evaluation separates changes in matrix state from

changes in the interface itself and establishes the length scale at which reinforcement becomes effective.

7.1. Dispersion Statistics and Representative Sampling

Dispersion is described by complementary spatial statistics: cluster fraction, particle spacing, reinforcement-rich region dimensions, and variation between representative fields. Each quantifies a different aspect of heterogeneity. Two-dimensional sections are influenced by particle orientation and preparation, whereas three-dimensional measurements additionally resolve connectivity. A network architecture is therefore characterized by its ligament dimensions and connected reinforcement paths rather than classified solely by a uniformity metric [8,27,32,41].

At fixed composition, changes in milling or blending can alter both dispersion and reinforcement integrity. The resulting strength or conductivity response depends on these changes together with residual porosity and matrix refinement. Process-focused GO/Cu blending studies connect these variables to the final contact network [53]. When density remains comparable, a relationship with cluster size or interface coverage becomes more specific; when density also changes, both contributions remain relevant.

The physical distinction between a designed network and an agglomerate is the coordination of deformation. A prescribed reinforcing skeleton can confine deformable matrix regions while maintaining connected load paths, as demonstrated in TiB/Ti [32]. An uncontrolled cluster instead creates local reinforcement-rich and matrix-depleted regions without ensuring adequate support or bonding. Both structures are nonuniform, but their connectivity, characteristic spacing, and response to strain differ fundamentally.

7.2. Grain, Orowan, and Thermal-Mismatch Contributions

Grain-boundary strengthening is commonly related to $d^{(-1/2)}$ through a Hall–Petch description, with d denoting matrix grain size. The appropriate coefficient depends on the matrix and microstructural regime. Electron backscatter diffraction and transmission electron microscopy provide grain-scale information, while diffraction line broadening resolves coherent-domain and strain contributions that need not equal the metallographic grain size. These measures constrain different aspects of refinement and are interpreted accordingly [8,41,102].

For non-shearable obstacles, an Orowan-type contribution scales approximately as $(Gb/\lambda)\ \ln(r/b)$, where G is the matrix shear modulus, b the Burgers-vector magnitude, λ the effective obstacle spacing, and r the obstacle radius. The inverse spacing dependence explains the greater relevance of a dense nanoscale dispersion than of widely separated micrometer-scale particles. In the latter case, load sharing, matrix constraint, local dislocation structures, and damage initiation generally dominate over a large bypass increment [12].

Direct evidence for thermal-mismatch dislocations is provided by Arsenault and Shi's analysis and by the in situ high-voltage electron microscopy study of Vogelsang et al. [104,105]. Cooling Al/SiC specimens generated dislocations near the reinforcing phase, with the observed response linked to differential thermal contraction. These experiments establish the physical mechanism independently of a hardness fit. Its retained contribution in a processed MMC subsequently depends on particle geometry, cooling history, and recovery.

Quantitative partitioning of strength consequently requires separate inputs for grain structure, obstacle spacing, retained dislocation density, and interface transfer. Fitting several terms to the same total strength increase can count the same microstructural change more than once. A constrained interpretation combines grain mapping, diffraction broadening, and local deformation observations with the measured yield response. The

resulting estimates identify plausible magnitudes while preserving interactions between refinement, dislocation storage, and load transfer [8,12,102,104].

7.3. Demonstrating Interfacial Stress Transfer

Stress-transfer attribution is stronger when mechanical response, fracture location, and interface measurements agree. Retained interfaces around fractured particles or an interface-sensitive test are more discriminating than an apparently smooth boundary. Pull-out can indicate weak contact, but preparation damage must be excluded before treating every cavity as service debonding [8,29].

Matrix strengthening is a competing explanation because it can increase hardness and reduce pull-out without changing intrinsic interface strength. Indentation mapping can separate local responses [31], but is not universally a bond-strength measurement. A justified model or dedicated interface experiment is necessary for that attribution.

Direct in situ observations also reveal how reinforcement geometry changes the failure sequence. CNT pull-out, nanotube fracture, and interwall sliding imply different balances among interface transfer, tube strength, and wall coupling. An interface that is strong enough to avoid early debonding may transfer damage into the reinforcement or matrix rather than eliminate damage altogether. This is why the measured pull-out strength and observed tensile fracture mode should be interpreted together. The design target is stable load sharing with acceptable composite deformation, not maximum interfacial strength in isolation [98–100].

7.4. Reaction Products and Layer Growth

Crystalline peaks establish a phase when the assignment is reliable, not its quantitative strengthening increment. Fe_2B/FeB in steel and TiC at a Ti–carbon boundary identify different pathways; value depends on location, fraction, continuity, and relation to damage or transport [29,69].

Reaction-layer growth links thermal exposure to both interface chemistry and reinforcement consumption. A growing carbide layer at a Ti–carbon boundary changes the residual carbon dimensions as well as the stiffness and continuity of the interface. In a diamond/metal contact, carbide formation can alter adhesion without producing a proportional increase in thermal conductance. These contrasting responses show that layer thickness is meaningful only together with phase identity, the initial interface state, and the property being transferred [29,106].

XRD identifies crystalline reaction products above the relevant detection limit, whereas thin, discontinuous, overlapping, or amorphous boundary phases can remain unresolved. Transmission electron microscopy, scanning transmission electron microscopy, and local compositional analysis address this spatial scale. Bulk phase analysis and interface-resolved characterization therefore provide complementary constraints on whether a reinforcement is retained, partly consumed, or transformed during processing [8,29].

Reaction products should be interpreted through location and connectivity as well as phase identity. Isolated fine carbides, a thin boundary layer, and a continuous brittle network can have very different consequences even when they share a chemical formula. Polymer-derived steel composites and tungsten-modified diamond/Cu illustrate beneficial reaction engineering for different functions: load-bearing phase formation in one case and boundary heat transfer in the other. A phase peak establishes that a crystalline product is present, whereas its continuity, thickness, and contribution to failure or transport require spatially resolved evidence [56,72,108].

7.5. Separating Porosity from Reinforcement Effects

Bulk density is compared with an appropriate final-phase theoretical density before assigning porosity. Connected pores matter particularly to fluid ingress, while isolated pores still affect fatigue and local deformation. A pore-area fraction from one field is not equivalent to three-dimensional connectivity [25,90,91].

Matched-composition density series reveal the influence of pore elimination, while comparisons at similar relative density emphasize other reinforcement effects. In both cases, pore morphology remains relevant: a rounded isolated pore and an interconnected defect at a reinforcement cluster produce different stress and transport fields. Density is therefore combined with pore size, shape, and location rather than treated as a complete description of consolidation [30,90,91].

Connected pores can transmit electrolyte, interrupt thermal contact, and intersect the surface as wear proceeds. Even a small average pore fraction can therefore contain a localized population that controls failure. Table 8 summarizes the measurements that distinguish the principal processing, interface, and damage mechanisms and relates each to the property it can physically influence.

Table 8. Mechanism-resolving measurements linking processing, interface structure, and the observed property response.

Proposed Mechanism	Required Descriptor/Contrast	Supportive Observation	Competing Explanation to Test
Load transfer [98,100]	Embedded geometry; orientation; interface-sensitive stress or in situ strain	Reinforcement load uptake or a resolved transfer/failure sequence	Matrix refinement, porosity reduction, or changed texture.
Grain refinement [8,102]	Comparable EBSD/TEM grain distributions and matrix state	Strength trend consistent with measured grain change	Peak broadening from strain or coherent domains rather than grain size.
Orowan bypass [12]	Non-shearable nanoscale obstacles and spacing	Scale-consistent strengthening estimate and dislocation evidence	Micrometer-particle constraint, load sharing, or a fitted sum of mechanisms.
Thermal-mismatch strengthening [104,105]	Thermal history and retained dislocation structure	Measured increase consistent with mismatch and recovery	Milling strain or matrix precipitation introduced by the same heat treatment.
Reaction-mediated response [56,72]	Phase chemistry; layer thickness/continuity; location	Property and damage/transport transition correlated with reaction progress	A new XRD peak without evidence of beneficial morphology or connectivity.
Film-assisted low shear [73,85]	Track and counterbody chemistry; time/coverage; debris	Persistent identified layer during favorable friction/wear interval	Transient material transfer or smoothing without a protective film.
Defect-controlled corrosion [84,116,117]	Exposure time; connected pores/cracks; electrochemical or mass-loss data	Attack linked to accessible defects and changing barrier integrity	A favorable potential shift treated as a lower corrosion rate.
Impact bonding in cold spray [86,87]	Velocity/temperature; local deformation; oxide disruption	Adhesion with a resolved impact/deformation pathway	Assuming that bonding alone proves adiabatic shear instability.

8. Surface Engineering and Functional Coatings

Surface engineering places functional material at the service-exposed region. Its design variables include retained coating phases, coating–substrate and inter-splat interfaces, thickness, connected defects, residual stress, and substrate support. These descriptors connect the selected deposition route to failure mode and retained function [15,16].

8.1. Thermal Spray and HVOF Coatings

Thermal spraying accelerates feedstock toward a prepared substrate and builds a layer through repeated impact and consolidation. HVOF can retain useful hard phases with relatively dense deposition when particle thermal/kinetic histories are controlled. Feedstock, stand-off distance, gas conditions, and substrate preparation influence splat cohesion, oxide formation, stress, and final porosity [15,16].

Quantitative descriptors include thickness distribution, total/connected porosity, oxide fraction, retained/transformed carbide, residual stress, and failure plane. A pull-off number must identify whether failure was within the coating, at the substrate boundary, or in the testing adhesive. These distinguish cohesion from interface adhesion and prevent a fixture-limited test from being misinterpreted as intrinsic bond strength [15,16].

Independent thermal-spray comparisons broaden the interpretation beyond binder composition. Bolelli et al. compared WC–10Co4Cr coatings deposited by HVOF and high-velocity air-fuel (HVAF) processes. The material designation alone does not capture the resulting contact response because particle heating, retained carbide, intersplat cohesion, and defects depend on deposition history. Consequently, comparisons should retain both the feedstock and the process-induced phase state. A coating that resists one sliding or abrasive condition may not retain the same ranking under a different contact severity or erosive environment [82].

8.1.1. WC–Co and WC–Co–Cr Coatings on High-Speed Steel

The comparison of WC–Co and WC–Co–Cr coatings on high-speed steel resolves the coupled influence of binder chemistry and coating thickness [77]. Carbide retention supplies local load support, while the metallic binder governs particle anchoring, cohesion, and accommodation of contact strain. Thickness changes the load distribution and the stored elastic energy, so the observed wear response reflects the full coating–substrate architecture rather than carbide hardness alone.

Cr-containing binder can change environmental behavior, but improvement requires testing in the relevant exposure. More thickness provides a greater wear allowance while altering stress and cracking/delamination risk. The relationship need not be monotonic; the hardest coating is not necessarily the one with the longest component life [15,16,77].

The comparison retains feedstock size, spray conditions, thickness/roughness distribution, substrate state, and microhardness load. Thin-layer indentation requires attention to substrate influence and penetration depth [31]. Quantitative comparisons retain the original source conditions rather than assuming that binder chemistry is their only independent variable.

Owoseni et al. compared HVOF- and HVAF-deposited WC–CoCr coatings on an Al alloy, considering wear and corrosion within the same coating study [88]. The comparison extends the analysis to a compliant, lightweight substrate, for which coating thickness and support influence contact damage. It also emphasizes that a surface with favorable abrasive behavior need not provide equivalent protection against fluid access or cavitation. Feedstock, spray history, and the substrate-supported coating structure jointly determine the resulting property combination.

Coating thickness influences both protection depth and fracture driving force. In a simplified elastic-film scaling, stored energy available for interfacial failure increases with $\sigma r^2 h/E'$, where σr is residual stress, h thickness, and E′ an appropriate constrained modulus. The expression is not a universal delamination criterion because geometry, cracking, plastic relaxation, and interface toughness also matter. It nevertheless explains why thicker coatings may provide more wear allowance yet become less tolerant of adhesion defects. Thickness optimization should therefore combine usable depth with stress, cohesion, and the observed failure plane [15,16,77].

8.1.2. NiCrBSi/WC–Co Coatings

Gürgenç et al. studied HVOF NiCrBSi/WC–Co on AZ91D with 0, 10, 30, and 50 wt.% WC–Co feedstock additions [78]. Reported hardness increased from 776 ± 4 to 959 ± 5 HV0.1 across the series, giving a mean-value ratio of 1.236 between coating conditions. This is not a ratio to the bare Mg substrate. The upper tested carbide condition gave the lowest reported wear in that spray window.

Feedstock wt.% is not automatically the retained carbide volume after deposition. Dissolution, oxidation, decarburization, and differential deposition efficiency can modify the final phase balance. The upper-loading endpoint is therefore a best-performing tested condition rather than a universal optimum. Final-phase and failure-location evidence is needed to distinguish particle support from binder or interface effects [78].

This system demonstrates localized functional modification of a lightweight substrate. The engineering benefit remains conditional on adhesion, retained substrate properties, and usable wear depth. Substrate exposure after coating failure must be part of a service comparison rather than omitted from an as-deposited hardness ranking.

On a compliant Mg substrate, the coating must transfer contact load without excessive substrate indentation or bending. Increasing WC–Co fraction can strengthen the surface while changing binder continuity and residual stress. The resulting design is thus a coating–substrate system, not a freestanding hardness comparison. Cross-sectional porosity, substrate condition after deposition, interface preparation, and the location of cracks should accompany the wear result. Retained protection after sliding is particularly important when the coating also serves as a corrosion barrier, because even a locally exposed Mg region can change the environmental response [25,78,79].

8.1.3. Inconel 625/WC Coatings

Inconel 625/WC illustrates a different Ni-based binder architecture on Mg [79]. Carbide identity alone cannot establish equivalence with NiCrBSi/WC–Co: binder chemistry alters cohesion, oxidation/corrosion response, thermal mismatch, and particle retention. These variables remain visible beside hardness and wear.

A useful comparison measures retained carbide distribution, coating defects, and damage location at matched contact conditions. If different binders fail at different planes, the cause cannot be reduced to the highest carbide hardness. The functional layer must remain supported by its metallic binder and substrate throughout loading [78,79].

For Inconel 625/WC and related metallic-binder coatings, reinforcement retention depends on the balance between carbide support and matrix accommodation. Partial carbide dissolution can modify the binder and generate additional phases; excessive reaction can reduce the fraction of the intended load-bearing constituent. The binder's environmental resistance is also not automatically identical to the corrosion resistance of a porous composite coating. A meaningful comparison therefore reports retained carbide, binder chemistry, connected defects, and the service medium, rather than inferring coating durability solely from the nominal alloy designation [79,82].

8.2. PVD and CVD Coatings

PVD physically transports vaporized material, for example through magnetron sputtering [21]; CVD forms coatings through gaseous-precursor reactions at or near the substrate [81]. Their thermal exposures, conformality, chemistry, and interface formation differ by implementation. A fixed universal thickness or temperature interval obscures these process-dependent differences.

For hard nitride and diamond-like carbon (DLC) films, thickness, residual stress, adhesion, and substrate support act together. A very hard film can crack when a compliant substrate yields. Duplex processing may improve support, but its value requires measured substrate state and failure behavior rather than an assumption based on the name of the treatment [21,31].

Cross-sectional structure, scale-appropriate indentation, and scratch/contact-fatigue failure morphology provide complementary evidence. Scratch critical load requires tip geometry, loading history, and a defined failure criterion; it is not directly an interface fracture energy. Functional depth and thermal exposure must also be included when comparing a thin film with a bulk MMC [21,31,81].

The mechanical support provided by the substrate defines the useful load range of a thin hard coating. If the substrate deforms appreciably, tensile or bending stresses can develop in a coating that is intrinsically resistant to indentation. A diffusion-hardened near-surface region or a graded interlayer can reduce this mismatch, but may also change residual stress and transport across the surface. Thin-film hardness, adhesion, and substrate yield behavior consequently form a coupled design set rather than independent selection criteria [21,81,83].

Thermal evolution can itself strengthen a hard thin film within a finite window. Mayrhofer et al. demonstrated self-organized nanoscale structures in the Ti–Al–N system, establishing a basis for discussing age-related hardening associated with decomposition and coherent domain formation. Longer or more severe exposure can alter that favorable structure. PVD selection should consequently consider the coating state after service-relevant thermal exposure, not only the as-deposited hardness. Interface adhesion, residual stress, and substrate support remain separate requirements; a highly hard film cannot compensate for a substrate that yields excessively under the contact [21,31,83].

8.3. Electrophoretic Deposition

EPD moves charged suspended particles under an electric field and assembles them on a substrate. Suspension chemistry, particle mobility, field, concentration, and deposition time control yield and distribution. The method offers composition flexibility, but successful deposition does not by itself establish a mechanically reliable coating [17–19].

The relevant descriptors include deposited mass/area, thickness distribution, drying-crack density, final porosity, and interface/cohesive strength. Zeta potential or suspension stability describes the deposition stage, not the final adhesion. Drying and subsequent consolidation or bonding treatments must be included in the complete process history [17–19].

The final thermal budget of EPD includes drying and any subsequent consolidation or bonding treatment. These steps change particle contacts, shrinkage, porosity, and substrate compatibility. A uniform deposit can consequently develop cracks or altered adhesion during post-treatment, linking suspension design to the final coating rather than to deposition alone [17–19].

MacLucas et al. quantified CNT coating growth during EPD on stainless steel as a function of voltage, additive, and time [89]. Higher voltage increased deposition rate, while magnesium nitrate and triethylamine produced different thickness-development histories. Approximately linear growth persisted over different initial intervals for the two

suspension chemistries. This comparison gives a mechanistic basis for controlling functional thickness: electrophoretic transport and evolving deposit resistance act together, so equal deposition time does not guarantee equal coating architecture across suspensions.

EPD separates suspension transport from final coating performance. In an idealized initial-stage deposition model, deposited mass per area scales with particle concentration, electrophoretic mobility, electric field, and time; real growth departs from this limit as suspension concentration and the electrical resistance of the deposit evolve. Drying and thermal treatment then establish cohesion and can generate cracks. Mahmoudi et al.'s GO/316 stainless-steel study provides a practical example: substrate pretreatment and electrolyte/suspension conditions affected protection, and a thicker coating was not necessarily the better barrier. The useful processing endpoint is a continuous, adherent layer with controlled defects [18,19,84].

8.4. Sol–Gel and Hybrid Coating Routes

Sol–gel processing modifies surface chemistry and can form oxide or hybrid layers from molecular/colloidal precursors. Drying, curing, and shrinkage govern continuity, cracks, and final thickness. The acceptance criterion is retained barrier or interface function, not merely the existence of a deposited precursor layer.

Sol–gel-coated B_4C incorporated into Al illustrates coating the reinforcement rather than the finished component [80]. Its relevant outcome is the final particle–matrix boundary after consolidation: whether the precursor survives, reacts usefully, or forms a brittle/resistive inclusion. This connects surface processing with bulk design without assuming an intact external barrier remains in service.

For sol–gel barriers, connected pores and cracks govern the transport of aggressive species, while adhesion determines whether protection survives exposure. For coated reinforcement particles, the same precursor chemistry instead influences wetting, reaction, and the final matrix–particle boundary during consolidation. These two applications share surface-chemical control but differ in the interface function and processing state that determine performance [80,118].

A hybrid barrier coating provides both an interface to the metal and a transport path for water and ions. Increasing cross-linking or filler tortuosity can reduce ingress, whereas drying shrinkage, aggregation, and thermal mismatch can create connected defects. Inhibitor-containing nanocontainers introduce a separate active response at damaged regions [118]. Barrier retention and local chemical inhibition are complementary functions, but neither implies recovery of the original mechanical strength of an opened crack. Their effectiveness is evaluated through exposure-dependent protection together with adhesion and damage morphology [80,84,118].

Hybrid sol–gel protection can be either passive or active. A continuous oxide/organic–inorganic network reduces access of aggressive species, while incorporated inhibitor reservoirs can respond to local damage. Shchukin et al. demonstrated layer-by-layer assembled nanocontainers in a hybrid coating on Al alloy, providing a distinct inhibitor-mediated protection mechanism. The appropriate evidence is the evolution of corrosion at a damaged site and the stability of the host layer. Release of an inhibitor should not be described as complete mechanical healing unless the original cohesion and barrier structure are also restored [118].

8.5. Laser Cladding

Laser cladding locally melts feedstock and part of a substrate to create a bonded surface layer. Power, scan speed, spot size, feed, substrate heat extraction, and reheating determine melt-pool history, dilution, phase evolution, and residual stress. Its metallurgical

connection introduces a corresponding heat-affected region and potential distortion/cracking constraints [20].

Dilution describes the fraction and distribution of substrate material incorporated into a laser-clad layer. It depends on melt-pool geometry and thermal history, so identical laser power can produce different dilution at different travel speeds, feed rates, or substrate conditions. Retained carbide, dissolution and reprecipitation, solidification morphology, and residual stress together determine the resulting hardness and failure response [20].

A selected coating is accepted only when it meets both surface and substrate requirements. A dense, hard deposit can be unsuitable if cracking or dilution compromises integrity or chemistry. Local hardness maps, cross sections, and representative contact tests therefore complement the nominal processing parameters.

In laser-clad MMCs, reinforcement retention competes with dissolution and reprecipitation in the melt pool. A higher nominal carbide addition can therefore change both the surviving particle population and the chemistry of the solidifying matrix. Fine reprecipitated phases may strengthen the coating, whereas coarse or continuous brittle constituents can form crack paths. The resulting architecture is determined by local thermal history, dilution, and solidification rather than feedstock composition alone. Cross-sectional phase distribution and the continuity of the metallurgical interface link these features to sliding and thermally assisted failure [20,85].

Laser cladding introduces a spatially and temporally varying thermal cycle. The ratio of laser power to travel speed is a useful first descriptor of line energy, but does not determine melt-pool state independently of spot size, absorptivity, powder feed, overlap, and heat extraction. Dilution should be measured from the actual deposited geometry or chemistry. For self-lubricating feedstocks, high processing temperature can transform the initial lubricant before service begins. The temperature-resolved study of Torres et al. therefore links feedstock chemistry, reaction products, and tribological response, rather than assuming that the original MoS_2 or WS_2 remains unchanged throughout deposition and use [20,85].

8.6. Comparative Assessment of Coating Technologies

Table 9 compares route-specific controls, measurable descriptors, and acceptance evidence. Thickness is treated as a system-dependent design variable rather than a universal numerical band. The table supports selection against substrate sensitivity, geometry, functional depth, and finishing requirements, not a claim that one process is inherently superior [15–21,80,81].

HVOF addresses thick particulate/cermet layers, PVD/CVD thin-film architectures, EPD particle assemblies, sol–gel precursor-based chemistry, and laser cladding melt-processed surface modification. The correct comparison identifies whether service failure occurs in the layer, at the substrate boundary, or within the substrate. This connects coating selection directly with the interface framework.

Cold spray supplies an additional solid-state comparison because particles are accelerated without intentional pre-impact melting. Assadi et al. related bonding to severe interfacial deformation and localization during impact. Later work by Hassani-Gangaraj et al. demonstrated that adiabatic shear instability is not a necessary condition for adhesion, identifying alternative impact-driven deformation and jetting pathways. The difference is mechanistically important: observed bonding should not be treated as proof of one universal instability. Particle velocity and temperature, oxide disruption, substrate response, and local deformation provide the experimentally accessible variables [86,87].

This solid-state route connects coating formation with PM interparticle bonding while retaining a different timescale and stress state. It can limit some melting-related

reactions, yet strong deformation, interface oxides, and post-deposition heat treatment still govern the final state. The coating comparison therefore spans three principal bonding routes: consolidation of particles under pressure and heat, impact-driven contact during spraying, and solidification or chemical growth at the substrate. Each requires a different control strategy, even when the final chemistry is nominally similar [81,86,87,96].

Table 9. Surface-engineering routes compared by functional thickness, interface formation, principal benefits, and controlling failure mechanisms.

Route and Sources	Key Process Controls	Descriptor/Acceptance Evidence	Principal Boundary
Thermal spray/HVOF and HVAF [15,16,77–79,88]	Feedstock, gas/thermal history, velocity, standoff, preparation	Thickness/porosity; carbide/oxide state; cohesion/adhesion; failure location	More thickness or hardness does not guarantee longer life; substrate support and stress remain essential.
PVD [21,31]	Vapor/ion conditions, bias, temperature, interlayer	Film structure/stress; support; scale-appropriate indentation; contact failure	Thin-film hardness is influenced by penetration and substrate; scratch load is protocol-dependent.
CVD [81]	Precursor, reactions, temperature, pressure, transport	Chemistry, uniformity/conformality, interface and substrate state	Thermal exposure and reaction compatibility must be established for the implementation.
EPD [17–19,89]	Suspension chemistry/mobility, field, time, drying, post-treatment	Deposited mass/area; thickness; crack/porosity; final bonding	Low deposition temperature is not the complete process thermal budget.
Sol–gel/particle functionalization [80]	Precursor chemistry, deposition cycles, drying/curing	Continuity, chemistry, cracks, final interface after consolidation	A precursor layer need not remain an intact service barrier or interlayer.
Laser cladding [20]	Power, speed, spot/feed, heat extraction, reheating	Measured dilution, phase retention, cracking, heat-affected substrate	Metallurgical bonding must be balanced against distortion, stress, and chemistry change.
Cold spray [86,87]	Impact velocity, temperature, oxide state, substrate response	Bonded fraction, local deformation, cohesion/adhesion and post-treatment state	Bonding is not unique evidence of adiabatic shear instability; absence of pre-impact melting does not ensure an oxide-free interface.

9. Bulk MMCs Versus Surface-Coating Strategies

The principal choice is the depth over which the function must persist. Bulk reinforcement is relevant to through-thickness stiffness, expansion control, or wear-through functionality. A coating is relevant when degradation is localized and the substrate already meets structural requirements. Neither is selected solely by the highest surface hardness.

Bulk MMCs expose fresh reinforced material during progressive wear, but manufacturing gradients, texture, and segregation can make that response nonuniform. The complete volume must meet integrity requirements. Ductility, toughness, machinability, and process repeatability therefore accompany the property gain.

A coating preserves bulk material while allocating functional constituents to the surface, provided adhesion, cohesion, support, and usable wear depth are adequate. Performance before breakthrough is not sufficient when expected wear rapidly reaches the substrate. A realistic comparison retains the transition to exposed-substrate behavior.

Current and heat paths determine the usefulness of a surface layer on Cu. Preserving bulk conductivity does not help if current must cross an excessively resistive coating. On Mg, a wear-improving bulk addition may worsen environmental performance, making a verified barrier or combined architecture worth considering. These examples show why service function, rather than hardness alone, determines the architecture [24–26].

The scale of material modification can be related to the depth and sequence of degradation. A bulk composite retains reinforcement as the surface recedes, whereas a coating provides a finite functional depth and can fail either by gradual removal or abrupt loss of adhesion. A duplex architecture can distribute these roles: the substrate supports load, an intermediate region reduces mismatch, and an outer layer controls shear or chemical exposure. Its value depends on whether the additional interfaces remain stable over the intended service interval [15,16,77,84,88].

Repairability and resource use are additional criteria. Recoating can extend use only when stripping, heat input, and repeated processing remain compatible with the substrate. A material-saving surface treatment is not automatically environmentally preferable if preparation energy, consumables, or replacement frequency dominate. A defensible comparison states a service-based system boundary.

Combined bulk-plus-coating architectures are justified when neither modification alone meets the constraints. The extra interface and residual-stress state must be evaluated rather than assuming that two individually favorable treatments remain favorable together. Table 10 summarizes the decision criteria and Figure 6 retains the volume-wide versus localized distinction.

Table 10. Application-oriented comparison of bulk reinforcement, surface coatings, and combined architectures.

Requirement	Bulk MMC	Surface Coating/Combined Architecture
Functional depth	Appropriate when modification must persist through the volume or substantial wear depth.	Appropriate when usable coating depth exceeds degradation depth and the substrate meets bulk needs.
Structural support	Matrix continuity, density uniformity, toughness, and fatigue response.	Substrate yielding, layer cohesion, adhesion, residual stress, and failure location.
Current/heat path	Retained bulk conductivity and direction-dependent heat transport.	Resistance across the layer and boundary, in addition to substrate conduction.
Environmental durability	Electrolyte access, galvanic interactions, and surface-film stability.	Connected defects, barrier continuity, and protection following wear or damage.
Manufacturing robustness	Mixing, segregation, consolidation, and spatial variability in the final architecture.	Preparation, deposition, finishing, thermal impact, and coating variability.
Repair/life-cycle	Retained reinforced volume can tolerate deeper wear; repair compatibility remains material-specific.	Recoating may extend life if stripping and repeated processing preserve substrate integrity.
Combined design	Supplies necessary structural/transport functionality through the component.	Adds surface function only when the additional interface and stress state satisfy service testing.

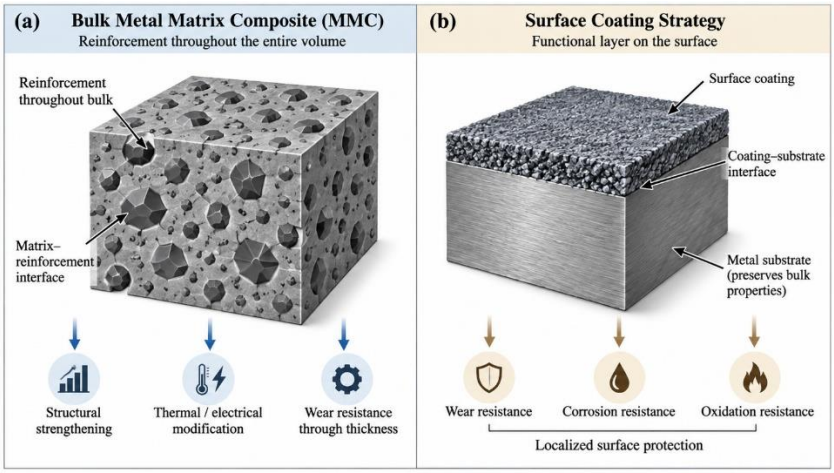

Aspect	Bulk MMC (a)	Surface Coating (b)
Property modification	Bulk properties (mechanical, thermal, electrical)	Surface properties (tribological, corrosion, oxidation)
Main interface	Matrix–reinforcement interface (throughout bulk)	Coating–substrate interface (at surface)
Typical failure risk	Particle fracture, interface debonding, matrix cracking	Coating delamination, interfacial failure
Most suitable use	Load-bearing structural components	Surface protection and lifetime extension

Figure 6. Conceptual comparison of (**a**) bulk metal matrix composites (MMCs) with volume-wide reinforcement and (**b**) surface coatings with localized surface protection, highlighting key interfaces and failure mechanisms.

Component-level selection should define the required functional depth before choosing the material route. For a coating, the usable thickness is the deposited thickness remaining after finishing, tolerances, and a damage allowance; it should exceed the expected service removal depth under a compatible wear protocol. For a bulk MMC, continued reinforcement exposure during wear is an advantage only if the deeper material has comparable density and architecture. Thus, the decision involves spatial uniformity as well as mean properties. Figure 6 illustrates the location of these functional regions, while the preceding selection table sets the corresponding engineering checks [4,15,16].

For conductive contacts, the functional depth is not purely mechanical. Current must cross the real contact junction and, for a coated component, potentially the coating and its boundary with the substrate. A wear-resistant but resistive layer can therefore shift damage from material removal to local heating. For heat-transfer components, an analogous issue arises when an interlayer improves adhesion but adds thermal resistance. Component selection consequently follows the actual load and flux paths, including interfaces between the engineered material and adjoining parts [23,30,33,106].

A combined bulk-plus-coating design introduces at least two interface populations: matrix–reinforcement boundaries and the coating–substrate boundary. A useful hierarchy might place load-bearing reinforcement in the bulk and a low-shear layer at the surface, but the coating thermal cycle can also modify the underlying composite. Heat treatment, diffusion, residual stress, and electrolyte access must therefore be assessed across the complete stack. The benefit is credible when the combined architecture outperforms relevant bulk-only and coating-only controls under the same service condition, rather than when separately measured best properties are assembled into an assumed system response [29,77,85].

10. Challenges and Research Directions

The principal unresolved issue is the transfer of laboratory-scale property improvements into reproducible interface specifications and service-relevant processing windows. Composition, architecture, matrix state, and environment interact, making isolated optimization of one response insufficient. Progress depends on resolving which interfacial

change governs a property and whether that change survives consolidation, post-processing, and operation.

10.1. Interface Evolution and Property Transfer

Reaction and contact evolution are particularly important where chemical bonding and transport compete. Controlled thermal exposure, combined with spatial distributions of layer thickness, phase identity, and residual reinforcement dimensions, can establish the reaction interval that preserves both integrity and function. The Ti–carbon and carbide/diamond results indicate that a mechanically useful reaction state need not maximize heat transfer. A central research question is therefore how the same evolving boundary redistributes stress, heat, and damage under repeated exposure [8,29,33,106].

10.2. Architecture, Damage Tolerance, and Coupled Service

Hierarchical and network architectures offer a route to separating rigid load-bearing regions from deformable matrix ligaments. Their effectiveness depends on the size, orientation, and connectivity of both phases. The next scientific challenge is to connect these descriptors to fatigue initiation, crack growth, and environmental access, rather than only monotonic strength. Cu contacts additionally require simultaneous current and sliding; Mg requires protection during deformation and wear; and coated substrates require adhesion and barrier retention after thermal or mechanical damage [26,32,43,45,46,65,68,88].

10.3. Reproducibility and Scale-Dependent Heterogeneity

Scale-up introduces spatial distributions of temperature, pressure, reinforcement concentration, and residual stress. These distributions can shift the governing failure mode even when the nominal recipe is unchanged. Independent powder batches and components, together with spatially resolved microstructural and property measurements, distinguish manufacturing variability from within-specimen measurement scatter. Reference materials and comparable contact configurations would further connect interlaboratory results to the microstructural features responsible for their differences [4,53,90,96].

10.4. Physics-Informed and Adaptive Materials Design

Data-driven models are most transferable when their descriptors represent the structure produced by processing. General materials descriptors and benchmarking procedures provide a starting point [119,120], but MMC prediction additionally requires matrix state, final reinforcement geometry, pore topology, interface chemistry, and test conditions. Wu et al. demonstrated the relevance of physical, chemical, and processing descriptors to interfacial thermal resistance [121]. Their training domain excluded two-dimensional and metal–metal interfaces, illustrating why a descriptor strategy can be useful even when direct transfer of a fitted model to graphene/metal systems requires new validation.

Adaptive experimental design provides a complementary approach to the cost of mapping coupled processing variables. Xue et al. integrated predictive uncertainty and sequential experimentation in a materials-design problem [122]. Applied to MMCs, the corresponding research objective is to sample both promising property combinations and uncertain boundaries of the acceptable processing region. Unsuccessful conditions carry information about incomplete densification, reaction-induced brittleness, corrosion, and delamination; their inclusion complements favorable endpoints and reduces selection bias in the resulting design map [122,123].

Model validation must preserve the structure of the experimental evidence. Measurements from the same batch share processing history, and multiple compositions can

share a control material. Separating validation by study or independently produced batch tests transfer more stringently than randomly splitting nearby measurements. Interpretable relationships between interface descriptors and response can then be evaluated prospectively: a predicted improvement is tested in a newly processed state, together with neighboring conditions that probe the proposed failure boundary [119–122].

10.5. Resource Efficiency and Service-Life Assessment

Environmental and economic assessment depends on the selected functional unit. Santiago-Herrera et al. compared high-energy-milled Ti6Al4V–TiC powder and atomized Ti6Al4V on a one-kilogram powder basis, providing a concrete framework for process accounting [124]. Component-level comparison additionally includes the different functions of the products, manufacturing yield, finishing, repair, and replacement interval. Shorter sintering dwell or high feedstock utilization alone does not resolve the total burden. A durable surface layer may reduce material use through repair, while a bulk composite may retain functionality after substantial wear; these service pathways determine the relevant life-cycle boundary.

Table 11 relates the principal research questions to measurable descriptors and decision outcomes. Together, these directions connect interface evolution, hierarchical deformation, coupled service, reproducibility, and resource use to the development of transferable processing–property relationships.

Table 11. Research priorities linking unresolved physical questions to measurable descriptors and engineering decisions.

Question	Controlled Experiment	Minimum Quantitative Evidence	Decision Enabled
Dispersion or damage? [53,101]	Mixing-energy series at fixed chemistry and consolidation	Cluster/length distributions; Raman conditions; density; batch-level properties	Identify when deagglomeration gains are offset by reinforcement fragmentation.
Useful reaction-layer window? [29,56,98]	Thermal-exposure series from one starting batch	Layer/phase distributions plus local mechanics or boundary transport	Locate a chemistry-specific window rather than assume one critical thickness.
How does optimum content shift? [43,44,64]	Fraction × size × processing design, with processed controls	Volume basis, density, matrix state, wear and damage-sensitive response	Distinguish an interior optimum from an upper tested endpoint.
Does the benefit survive service? [61,85,117]	Current-assisted sliding, environmental exposure, or thermal cycling	Temperature/contact resistance; wear; corrosion/degradation after damage	Select by retained function rather than isolated room-temperature hardness.
Are results reproducible?	Independent batches and specimens with nested repeat measurements	Defined intervals, failure modes, calibrated geometry and complete test metadata	Separate processing variability from measurement scatter.

Does the model generalize? [119–123]	Study-held-out validation followed by prospective tests	Final-state and test descriptors; missingness; uncertainty; failed conditions	Predict a feasible region and a discriminating next experiment.
Is the route resource-efficient? [124]	Equivalent component/service comparison across scale and yield	Powder production, gas/energy, finishing, replacement, repair and recovery	Select lower burden per accepted service, not merely shorter dwell.

11. Conclusions

Reinforcement effectiveness is governed by the interface and microstructure created during processing, not by constituent identity alone. Matrix state, reinforcement geometry, bonded contact, residual porosity, and reaction history determine whether an addition contributes to load transfer, heat and charge transport, or damage initiation. These variables provide a common basis for interpreting PM-derived MMCs and surface-engineered metallic systems.

Within-study comparisons quantify distinct strengthening and wear responses. The B_4C/Cu and GO/Cu examples yield hardness ratios of 1.689 and 2.100, respectively, while the AZ91D–Ni/graphene series gives a hardness ratio of 1.331 and a specific-wear-rate ratio of 0.739. Their different reference states and test conditions preserve their value as material-specific benchmarks. Particle-size-dependent Al fatigue and Ti–TiB deformation further establish that hardness and tensile strength cannot replace damage-tolerance criteria [13,14,43,60,68].

The useful reinforcement window is property dependent. Carbon chemistry can separate favorable mechanical and corrosion responses in Mg, interface and orientation control can reconcile strength with conduction in Cu, and hierarchical Al or Ti architectures can distribute load while retaining deformable metallic regions. Ni-based systems additionally require a lubricant and matrix that remain functional across the operating temperature interval [32,45,46,54,61,74].

Thermal and environmental performance are controlled by different aspects of interface continuity. Improved contact and engineered interlayers can enhance heat transfer, but carbide formation alone does not guarantee higher boundary conductance. Corrosion protection requires stable coverage and controlled electrochemical access over time; an initially protective conductive film can become unfavorable when defects and exposure history change. Interface chemistry is therefore selected together with the transport direction and service environment [33,56,106,116,117].

Direct interface-sensitive measurements provide the strongest constraints on mechanistic interpretation. Nanotube pull-out, in situ deformation and dislocation observations, local phase analysis, and thermal-boundary measurements connect specific boundary processes to the observed response. Bulk hardness, diffraction, and microscopy correlations remain valuable when interpreted alongside matrix refinement, pore structure, and the limitations of their spatial resolution [98–102,104,105].

Bulk MMCs are favored when functional modification must persist through the component, whereas coatings concentrate protection where damage is localized. Their integration requires adequate substrate support, stable adhesion, controlled connected defects, and a functional depth compatible with wear and environmental exposure. The preferred architecture satisfies these constraints without imposing unnecessary loss of ductility, conductivity, or material efficiency [77,84,88].

Future advances are most likely to arise from controlled interface evolution, deliberate spatial architecture, and validation under coupled service conditions. Quantitative

descriptors and independent replication can transform isolated property gains into reproducible processing windows, while adaptive design and service-based resource assessment can accelerate selection among competing solutions. This integration provides a mechanistic foundation for durable, multifunctional MMCs and coatings rather than optimization of a single response in isolation [119–124].

Author Contributions: C.K.M. was responsible for the conceptualization and overall design of the review, literature investigation, critical analysis and synthesis of the published findings, development of the process–structure–property framework, and preparation of the original manuscript. M.A. contributed to the literature review, extraction and organization of relevant scientific data, comparative evaluation of metal matrix composites and functional coating systems, and critical revision of the manuscript. B.A. provided scientific supervision, methodological guidance, project administration, and funding acquisition, and contributed to the interpretation of the reviewed evidence and critical revision of the manuscript. F.K. and Y.S. contributed to the technical evaluation of the literature, interpretation of microstructural and materials-performance relationships, validation of the comparative discussion, and manuscript review and editing. All authors have read and agreed to the published version of the manuscript.

Funding: This work was supported by the Fırat University Research Fund (FÜBAP) under Project No. SHY.26.08.

Data Availability Statement: The data and scientific evidence evaluated in this review were obtained from previously published studies, which are appropriately cited in the manuscript. No new experimental datasets were generated as part of this review. Additional information regarding the literature synthesis and comparative analyses is available from the corresponding author upon reasonable request.

Acknowledgments: The authors gratefully acknowledge the financial support provided by the Fırat University Scientific Research Projects Coordination Unit (FÜBAP) under Project No. SHY.26.08. The authors also thank Aisin Automotive Parts Industry and Trade Inc. for its valuable technical and institutional support.

During the preparation of this manuscript, the authors used OpenAI's ChatGPT (GPT-6), including its image-generation functionality, for English language refinement, scientific text editing, and AI-assisted creation and revision of conceptual illustrations. The AI-assisted figures are schematic representations and do not constitute experimental SEM/TEM micrographs. The authors have reviewed, verified, and edited the generated content and take full responsibility for the scientific accuracy, integrity, and content of this publication.

Conflicts of Interest: Merve Ayık was employed by Aisin Automotive Parts Industry and Trade Inc. The remaining authors declare that the research was conducted in the absence of any commercial or financial relationships that could be construed as a potential conflict of interest. The funders had no role in the design of the study; in the collection, analyses, or interpretation of data; in the writing of the manuscript; or in the decision to publish the results.

References

1. Zhao, Z.; Bai, P.; Du, W.; Liu, B.; Pan, D.; Das, R.; Liu, C.; Guo, Z. An Overview of Graphene and Its Derivatives Reinforced Metal Matrix Composites: Preparation, Properties and Applications. *Carbon* **2020**, *170*, 302–326.
2. Akhtar, S.; Saad, M.; Misbah, M.R.; Sati, M.C. Recent Advancements in Powder Metallurgy: A Review. *Mater. Today Proc.* **2018**, *5*, 18649–18655.
3. Fang, Z.Z.; Paramore, J.D.; Sun, P.; Chandran, K.S.R.; Zhang, Y.; Xia, Y.; Cao, F.; Koopman, M.; Free, M. Powder Metallurgy of Titanium–Past, Present, and Future. *Int. Mater. Rev.* **2018**, *63*, 407–459.
4. Danninger, H.; Calderon, R.D.O.; Gierl-Mayer, C. Powder Metallurgy and Sintered Materials. *Addit. Manuf.* **2017**, *19*, 1–57.

5. Sharma, S.K.; Gajević, S.; Sharma, L.K.; Mohan, D.G.; Sharma, Y.; Radojković, M.; Stojanović, B. Significance of the Powder Metallurgy Approach and Its Processing Parameters on the Mechanical Behavior of Magnesium-Based Materials. *Nanomaterials* **2025**, *15*, 92.
6. Gök, D.A.; Bayraktar, C.; Hoşkun, M. A Review on Processing, Mechanical and Wear Properties of Al Matrix Composites Reinforced with Al_2O_3, SiC, B_4C and MgO by Powder Metallurgy Method. *J. Mater. Res. Technol.* **2024**, *31*, 1132–1150.
7. Suryanarayana, C. Mechanical Alloying and Milling. *Prog. Mater. Sci.* **2001**, *46*, 1–184.
8. Wang, Z.; Rong, X.; Zhao, D.; Zhang, X.; He, C.; Zhao, N. Recent Advances in Interface Engineering in Aluminum Matrix Composites Reinforced by Nano-Ceramic Phases: From Atomic Structure to Mechanical Performance. *Mater. Horiz.* **2025**, *12*, 10478–10497.
9. Ren, X.; Chang, Y.; Ge, C. State-of-the-Art Carbon-Nanotubes-Reinforced Copper-Based Composites: The Interface Design of CNTs and Cu Matrix. *Int. J. Mol. Sci.* **2024**, *25*, 12957.
10. Bharathi, P.; Kumar, T.S. Mechanical Characteristics and Wear Behaviour of Al/SiC and Al/SiC/B4C Hybrid Metal Matrix Composites Fabricated through Powder Metallurgy Route. *Silicon* **2023**, *15*, 4259–4275.
11. Yan, Y.-F.; Kou, S.-Q.; Yang, H.-Y.; Shu, S.-L.; Qiu, F.; Jiang, Q.-C.; Zhang, L.-C. Ceramic Particles Reinforced Copper Matrix Composites Manufactured by Advanced Powder Metallurgy: Preparation, Performance, and Mechanisms. *Int. J. Extreme Manuf.* **2023**, *5*, 32006.
12. Zhang, Z.; Chen, D.L. Consideration of Orowan Strengthening Effect in Particulate-Reinforced Metal Matrix Nanocomposites: A Model for Predicting Their Yield Strength. *Scr. Mater.* **2006**, *54*, 1321–1326.
13. Macit, C.K.; Gürgenç, T.; Aksakal, B.; Aslan, N. Comparative Microstructural, Mechanical, and Tribological Evaluation of Cu Matrix Composites Reinforced with B4C, B, Cr, Co, Al2O3, and Graphite via Powder Metallurgy. *Lubricants* **2026**, *14*, 243.
14. Macit, C.K.; Aksakal, B.; Horlu, M. Graphene Oxide-Reinforced Copper Matrix Composites: Microstructural Enhancements and Tribological Performance Via Hot Pressing. *Tribol. Lett.* **2025**, *73*, 117.
15. Pawlowski, L. *The Science and Engineering of Thermal Spray Coatings*; John Wiley & Sons: Hoboken, NJ, USA, 2008.
16. Fauchais, P.L.; Heberlein, J.V.R.; Boulos, M.I. *Thermal Spray Fundamentals: From Powder to Part*; Springer Science & Business Media: Berlin/Heidelberg, Germany, 2014.
17. Boccaccini, A.R.; Zhitomirsky, I. Application of Electrophoretic and Electrolytic Deposition Techniques in Ceramics Processing. *Curr. Opin. Solid State Mater. Sci.* **2002**, *6*, 251–260.
18. Sarkar, P.; Nicholson, P.S. Electrophoretic Deposition (EPD): Mechanisms, Kinetics, and Application to Ceramics. *J. Am. Ceram. Soc.* **1996**, *79*, 1987–2002.
19. Besra, L.; Liu, M. A Review on Fundamentals and Applications of Electrophoretic Deposition (EPD). *Prog. Mater. Sci.* **2007**, *52*, 1–61.
20. Toyserkani, E.; Khajepour, A.; Corbin, S.F. *Laser Cladding*; CRC Press: Boca Raton, FL, USA, 2004.
21. Kelly, P.J.; Arnell, R.D. Magnetron Sputtering: A Review of Recent Developments and Applications. *Vacuum* **2000**, *56*, 159–172.
22. Sarmah, P.; Gupta, K. Recent Advancements in Fabrication of Metal Matrix Composites: A Systematic Review. *Materials* **2024**, *17*, 4635.
23. Hidalgo-Manrique, P.; Lei, X.; Xu, R.; Zhou, M.; Kinloch, I.A.; Young, R.J. Copper/Graphene Composites: A Review. *J. Mater. Sci.* **2019**, *54*, 12236–12289.
24. Wang, J.; Guo, L.; Lin, W.; Chen, J.; Zhang, S.; Zhen, T.; Zhang, Y. The Effects of Graphene Content on the Corrosion Resistance, and Electrical, Thermal and Mechanical Properties of Graphene/Copper Composites. *New Carbon Mater.* **2019**, *34*, 161–169.
25. Pardo Gutiérrez Del Cid, Á.; Merino, S.; Merino Casals, M.C.; Mohedano Sánchez, M.; Arrabal Durán, R. Corrosion Behaviour of Silicon-Carbide-Particle Reinforced AZ92 Magnesium Alloy. *Corros. Sci.* **2009**, *51*, 841–849.
26. Turan, M.E.; Sun, Y.; Akgul, Y.; Turen, Y.; Ahlatci, H. The Effect of GNPs on Wear and Corrosion Behaviors of Pure Magnesium. *J. Alloys Compd.* **2017**, *724*, 14–23.
27. Varol, T.; Canakci, A. Effect of Weight Percentage and Particle Size of B4C Reinforcement on Physical and Mechanical Properties of Powder Metallurgy Al2024-B4C Composites. *Met. Mater. Int.* **2013**, *19*, 1227–1234.
28. Chand, S.; Chandrasekhar, P.; Roy, S.; Singh, S. Influence of Dispersoid Content on Compressibility, Sinterability and Mechanical Behaviour of B4C/BN Reinforced Al6061 Metal Matrix Hybrid Composites Fabricated via Mechanical Alloying. *Met. Mater. Int.* **2021**, *27*, 4841–4853.
29. Lv, S.; Li, J.S.; Li, S.F.; Kang, N.; Chen, B. Effects of Heat Treatment on Interfacial Characteristics and Mechanical Properties of Titanium Matrix Composites Reinforced with Discontinuous Carbon Fibers. *J. Alloys Compd.* **2021**, *877*, 160313.

30. Nan, C.-W.; Birringer, R.; Clarke, D.R.; Gleiter, H. Effective Thermal Conductivity of Particulate Composites with Interfacial Thermal Resistance. *J. Appl. Phys.* **1997**, *81*, 6692–6699.
31. Oliver, W.C.; Pharr, G.M. An Improved Technique for Determining Hardness and Elastic Modulus Using Load and Displacement Sensing Indentation Experiments. *J. Mater. Res.* **1992**, *7*, 1564–1583.
32. Huang, L.J.; Wang, S.; Dong, Y.S.; Zhang, Y.Z.; Pan, F.; Geng, L.; Peng, H.X. Tailoring a Novel Network Reinforcement Architecture Exploiting Superior Tensile Properties of in Situ TiBw/Ti Composites. *Mater. Sci. Eng. A* **2012**, *545*, 187–193.
33. Jiang, T.; Zhang, X.; Vishwanath, S.; Mu, X.; Kanzyuba, V.; Sokolov, D.A.; Ptasinska, S.; Go, D.B.; Xing, H.G.; Luo, T. Covalent Bonding Modulated Graphene–Metal Interfacial Thermal Transport. *Nanoscale* **2016**, *8*, 10993–11001.
34. Rajanish, M.; Avilasha, B.G.; Katti, P.P.; Ashwini, M.V.; Sudarshan, T.A.; Anantha Padmanabham, T.C.; Veeresha, G.; Nagaraj, P.; Hemanth Raju, T.; Udayashankar, S. Microstructure, Hardness and Wear Study of Al7075-B4C Metal Matrix Composites. *J. Inst. Eng. Ser. D* **2024**, 106, 1851–1863.
35. Macit, C.K.; Aksakal, B.; Çelik, Ü.; Horlu, M. Fabrication of High-Performance RGO/Cu Composites via Arc Induction Melting: A Comprehensive Study on Microstructure, Tribological and Electrical Properties. *Adv. Eng. Mater.* **2026**, *28*, e202502310.
36. Akbarpour, M.R.; Alipour, S.; Azar, F.L.; Torknik, F.S. Microstructure and Hardness of Al-SiC Nanocomposite Fabricated through Powder Metallurgy Method. *Indian J. Sci. Technol.* **2016**, *9*, 42.
37. Shaikh, M.B.N.; Aziz, T.; Arif, S.; Ansari, A.H.; Karagiannidis, P.G.; Uddin, M. Effect of Sintering Techniques on Microstructural, Mechanical and Tribological Properties of Al-SiC Composites. *Surf. Interfaces* **2020**, *20*, 100598.
38. Liu, L.; Li, S.; Zhang, X.; Pan, D.; Gao, L.; Chen, B.; Umeda, J.; Kondoh, K. Syntheses, Microstructure Evolution and Performance of Strength-Ductility Matched Aluminum Matrix Composites Reinforced by Nano SiC-Cladded CNTs. *Mater. Sci. Eng. A* **2021**, *824*, 141784.
39. Rashad, M.; Pan, F.; Yu, Z.; Asif, M.; Lin, H.; Pan, R. Investigation on Microstructural, Mechanical and Electrochemical Properties of Aluminum Composites Reinforced with Graphene Nanoplatelets. *Prog. Nat. Sci. Mater. Int* **2015**, *25*, 460–470.
40. Esawi, A.M.K.; Morsi, K.; Sayed, A.; Taher, M.; Lanka, S. Effect of Carbon Nanotube (CNT) Content on the Mechanical Properties of CNT-Reinforced Aluminium Composites. *Compos. Sci. Technol.* **2010**, *70*, 2237–2241.
41. Saheb, N.; Aliyu, I.K.; Hassan, S.F.; Al-Aqeeli, N. Matrix Structure Evolution and Nanoreinforcement Distribution in Mechanically Milled and Spark Plasma Sintered Al-SiC Nanocomposites. *Materials* **2014**, *7*, 6748–6767.
42. Canakci, A.; Varol, T. Microstructure and Properties of AA7075/Al–SiC Composites Fabricated Using Powder Metallurgy and Hot Pressing. *Powder Technol.* **2014**, *268*, 72–79.
43. Tokaji; Shiota; Kobayashi. Effect of Particle Size on Fatigue Behaviour in SiC Particulate-reinforced Aluminium Alloy Composites. *Fatigue Fract. Eng. Mater. Struct.* **1999**, *22*, 281–288.
44. Cao, L.; Dai, Q.; Liang, Q.; Zhang, X. The Influence of Process Conditions and Reinforcement Characteristics on the Densification and Mechanical Properties of Powder Metallurgy SiCp/Al Composites. *Materials* **2025**, *18*, 5060.
45. Li, Z.; Guo, Q.; Li, Z.; Fan, G.; Xiong, D.-B.; Su, Y.; Zhang, J.; Zhang, D. Enhanced Mechanical Properties of Graphene (Reduced Graphene Oxide)/Aluminum Composites with a Bioinspired Nanolaminated Structure. *Nano Lett.* **2015**, *15*, 8077–8083.
46. Zhang, Y.; Li, X. Bioinspired, Graphene/Al2O3 Doubly Reinforced Aluminum Composites with High Strength and Toughness. *Nano Lett.* **2017**, *17*, 6907–6915.
47. Kara, G.I.; Sezek, S.; Aksakal, B.; Macit, C.K.; Horlu, M. Effect of Sintering Temperature, Additive Ratios, and Reinforcement of Boron and Boron Carbide Particle Sizes on the Mechanical and Tribological Properties of the Synthesized Cu-Cr Hybrid Composites. *Tribol. Int.* **2024**, *199*, 110011.
48. Macit, C.K.; Horlu, M.; Tanyeri, B.; Aksakal, B. Publisher Correction: Production of Alumina–Graphene–Copper Hybrid Composites by Hot Pressing Technique: Investigation of Mechanical, Structural, and Tribological Properties. *J. Mater. Res.* **2025**, *40*, 980.
49. Macit, C.K.; Horlu, M.; Aksakal, B.; Er, Y. Synthesis of Copper Matrix Hybrid Composites with Boron-, Nitrogen-, and Silicon-Doped Reduced Graphene Oxide by Hot Press Technique: Investigation of Tribological, Mechanical, and Electrical Conductivity Properties. *Adv. Eng. Mater.* **2025**, *27*, 2401670.
50. Liu, Z.; Chen, X.; Zhang, S.; Cao, F.; Jiang, Y.; Chen, Z.; Kang, H.; Cao, Z.; Guo, E.; Liang, S. Preparation, Mechanical Properties and Tribological Properties of Cu Matrix Composites Induced by an Al-TiB2 Precursor. *J. Alloys Compd.* **2025**, *1020*, 179542.
51. Chu, K.; Wang, X.; Wang, F.; Li, Y.; Huang, D.; Liu, H.; Ma, W.; Liu, F.; Zhang, H. Largely Enhanced Thermal Conductivity of Graphene/Copper Composites with Highly Aligned Graphene Network. *Carbon* **2018**, *127*, 102–112.
52. Gao, X.; Yue, H.; Guo, E.; Zhang, H.; Lin, X.; Yao, L.; Wang, B. Mechanical Properties and Thermal Conductivity of Graphene Reinforced Copper Matrix Composites. *Powder Technol.* **2016**, *301*, 601–607.

53. de Souza, C.M.P.; Cunali Junior, J.R.C.; da Silva, M.R.; dos Santos, V.T.; Lobo, F.G.; dos Santos, G.A.; Almeida, G.F.C.; Couto, A.A.; Massi, M. Evaluation of Different Blending Methods to Obtain Copper Composites with Graphene Oxide. *Metals* **2024**, *14*, 1279.
54. Shi, Z.; Yun, Q.; Zhang, T.; Xing, C.; Li, J.; Wu, Y.; Wang, L. Facile Preparation of High-Performance Reduced Graphene Oxide (RGO)/Copper (Cu) Composites Based on Pyrolysis of Copper Formate. *Materials* **2024**, *17*, 2519.
55. Yang, G.; Zhang, Q.; Fang, Q.; Li, W.; Wei, H.; Zhao, T.; Zhang, Y.; Huang, G.; Cui, C.; Zhang, K. Preparation of Nickel Nanoparticle-Decorated Graphene/Copper Composites with Enhanced Interfacial Bonding and Heat Dissipation Properties. *J. Alloys Compd.* **2025**, *1028*, 180696.
56. Wang, Q.; Ye, Z.; Liu, L.; Bai, J.; Zhao, Y.; Hu, Q.; Liu, H.; Hu, L.; Guo, X.; Xiao, Y. High Thermal Conductivity Diamond–Copper Composites Prepared via Hot Pressing with Tungsten–Coated Interfacial Layer Optimization. *Materials* **2025**, *18*, 3882.
57. Chen, X.; Zhao, L.; Jiang, L.; Wang, H. Microstructures and Properties of Cu-Rgo Composites Prepared by Microwave Sintering. *Materials* **2021**, *14*, 4899.
58. Sui, X.; Xu, H.; Jiang, B.; Wang, Y.; Hu, M.; Ji, Z. Effect of the TiB2 Content on the Mechanical and Tribological Properties of TiB2/AZ91 Composites Fabricated by Vacuum Hot-Press Sintering Process Incorporating Vacuum Ball Milling. *Mater. Today Commun.* **2024**, *40*, 109722.
59. Kumar, A.; Kumar, S.; Mukhopadhyay, N.K.; Yadav, A.; Winczek, J. Effect of SiC Reinforcement and Its Variation on the Mechanical Characteristics of AZ91 Composites. *Materials* **2020**, *13*, 4913.
60. Ogunbiyi, O.; Iwarere, S.A.; Sadiku, R.; Daramola, M.O. Microstructure, Mechanical, Tribological and Synergistic Strengthening Mechanisms of Nickel/Graphene Nanoplatelets Hybrid Reinforced AZ91D Magnesium-Based Matrix Composites via Spark Plasma Sintering. *J. Mater. Res. Technol.* **2024**, *29*, 2628–2640.
61. Li, L.; Peng, D.; Lei, P.; Chen, L.; Hou, H.; Zhao, Y. Study of the Microstructure, Corrosion Behavior, and Mechanical Properties of AZ91D Composites Containing Various Graphene-Based Nanomaterials. *Mater. Sci. Eng. A* **2024**, *912*, 146939.
62. Saberi, A.; Bakhsheshi-Rad, H.R.; Karamian, E.; Kasiri-Asgarani, M.; Ghomi, H. Magnesium-Graphene Nano-Platelet Composites: Corrosion Behavior, Mechanical and Biological Properties. *J. Alloys Compd.* **2020**, *821*, 153379.
63. Shahin, M.; Munir, K.; Wen, C.; Li, Y. Magnesium-Based Composites Reinforced with Graphene Nanoplatelets as Biodegradable Implant Materials. *J. Alloys Compd.* **2020**, *828*, 154461.
64. Dengiz, E.Ö.; Dengiz, C.G.; Gürbüz, M. Experimental and Numerical Study on the Influence of Graphene Reinforcement and Processing Parameters on the Mechanical and Tribological Behavior of Magnesium Composites. *Proc. Inst. Mech. Eng. Part L J. Mater. Des. Appl.* **2026**, *240*, 1608–1628.
65. Xu, Z.Y.; You, Y.Q.; Lu, Q.; Li, C.J.; Song, M.; Tan, J.; Liu, L.; Chen, X.F.; Yi, J.H. Breaking Mg Matrix Composite Property Trade-Offs via in-Situ Interface Reaction and Heterogeneous Structure Design. *J. Magnes. Alloys* **2025**, *13*, 6121–6135.
66. Cai, C.; Song, B.; Qiu, C.; Li, L.; Xue, P.; Wei, Q.; Zhou, J.; Nan, H.; Chen, H.; Shi, Y. Hot Isostatic Pressing of In-Situ TiB/Ti-6Al-4V Composites with Novel Reinforcement Architecture, Enhanced Hardness and Elevated Tribological Properties. *J. Alloys Compd.* **2017**, *710*, 364–374.
67. Liu, Y.; Xu, X.; Tabie, V.; Li, C.; Jiang, Z.; Liu, Q.; Xiao, Y.; Zhang, X. Hot Corrosion Resistance of a Ti–Mo–Nb–Al–Si Titanium Matrix Composites Reinforced with in-Situ TiC Prepared by Powder Metallurgy. *Mater. Res. Express* **2019**, *6*, 126510.
68. Li, Q.; Huang, S.; Gao, Y.; Ramamurty, U. Deformation, Fracture, and Fatigue Crack Growth Behavior in TiB-Reinforced near-α Ti Matrix Composites Fabricated Using Powder Metallurgy Technique. *Mater. Sci. Eng. A* **2024**, *916*, 147351.
69. Macit, C.K.; Aksakal, B.; Horlu, M. Enhancement on the Tribological Properties of 316L Stainless Steel via Boron and Alumina Additions Using Mechanical Alloying and Powder Metallurgy Techniques. *Ceram. Int.* **2025**, *51*, 51549–51572.
70. Razavi, M.; Yaghmaee, M.S.; Rahimipour, M.R.; Razavi-Tousi, S.S. The Effect of Production Method on Properties of Fe–TiC Composite. *Int. J. Miner. Process.* **2010**, *94*, 97–100.
71. Patil, A.; Walunj, G.; Ozdemir, F.; Gupta, R.K.; Borkar, T. Tribological Behavior of Carbon-Based Nanomaterial-Reinforced Nickel Metal Matrix Composites. *Materials* **2021**, *14*, 3536.
72. Guan, D.; He, X.; Zhang, R.; Qu, X. Microstructure and Tensile Properties of in Situ Polymer-Derived Particles Reinforced Steel Matrix Composites Produced by Powder Metallurgy Method. *Mater. Sci. Eng. A* **2017**, *705*, 231–238.
73. Davis, D.; Marappan, G.; Sivalingam, Y.; Panigrahi, B.B.; Singh, S. Tribological Behavior of NiMoAl-Based Self-Lubricating Composites. *ACS Omega* **2020**, *5*, 14669.
74. Piasecki, A.; Kotkowiak, M.; Tisov, O.; Gapiński, B.; Jakubowicz, M.; Sobkowiak, J.; Tuliński, M.; Legutko, S. The Wear Resistance of NiCrSiB-20% CaF2 Sinters in the Temperature Range 23–600° C. *Materials* **2025**, *18*, 1405.

75. Kasalo, M.; Nayak, U.P.; MacLucas, T.; Suarez, S.; Bachmaier, A. Optimizing the Tribological Behavior of Nanocrystalline Inconel 718 by Solid Lubricant Reinforcements. *Tribol. Lett.* **2026**, *74*, 104.
76. Lin, S.; Xiong, W. Microstructure and Abrasive Behaviors of TiC-316L Composites Prepared by Warm Compaction and Microwave Sintering. *Adv. Powder Technol.* **2012**, *23*, 419–425.
77. Macit, C.K.; Aksakal, B.; Ayık, M.; Gürgenç, T.; Aslan, N. Thickness-and Binder-Chemistry-Dependent Structural, Mechanical, and Tribological Performance of HVOF-Sprayed WC-Co and WC-Co-Cr Coatings on High-Speed Steel. *Crystals* **2026**, *16*, 427.
78. Gürgenç, T.; Macit, C.K.; Sömer, M.; Aksakal, B.; Ayık, M.; Say, Y. Microstructure and Dry-Sliding Tribology of HVOF-Sprayed NiCrBSi/WC-Co Coatings on AZ91D. *Coatings* **2026**, *16*, 906.
79. Somer, M.; Gurgenc, T.; Ilkilic, C.; Macit, C.K. Investigation of Microstructure and Mechanical Properties of Magnesium Alloy Coated with Inconel 625/WC Composites by HVOF Method. *Surf. Rev. Lett.* **2023**, *30*, 2350077.
80. Mazahery, A.; Shabani, M.O. Sol–Gel Coated B4C Particles Reinforced 2024 Al Matrix Composites. *Proc. Inst. Mech. Eng. Part L J. Mater. Des. Appl.* **2012**, *226*, 159–169.
81. Choy, K.L. Chemical Vapour Deposition of Coatings. *Prog. Mater. Sci.* **2003**, *48*, 57–170.
82. Bolelli, G.; Berger, L.-M.; Börner, T.; Koivuluoto, H.; Lusvarghi, L.; Lyphout, C.; Markocsan, N.; Matikainen, V.; Nylén, P.; Sassatelli, P. Tribology of HVOF-and HVAF-Sprayed WC–10Co4Cr Hardmetal Coatings: A Comparative Assessment. *Surf. Coat. Technol.* **2015**, *265*, 125–144.
83. Mayrhofer, P.H.; Hörling, A.; Karlsson, L.; Sjölén, J.; Larsson, T.; Mitterer, C.; Hultman, L. Self-Organized Nanostructures in the Ti–Al–N System. *Appl. Phys. Lett.* **2003**, *83*, 2049–2051.
84. Mahmoudi, M.; Raeissi, K.; Karimzadeh, F.; Golozar, M.A. A Study on Corrosion Behavior of Graphene Oxide Coating Produced on Stainless Steel by Electrophoretic Deposition. *Surf. Coat. Technol.* **2019**, *372*, 327–342.
85. Torres, H.; Vuchkov, T.; Slawik, S.; Gachot, C.; Prakash, B.; Ripoll, M.R. Self-Lubricating Laser Claddings for Reducing Friction and Wear from Room Temperature to 600 C. *Wear* **2018**, *408*, 22–33.
86. Assadi, H.; Gärtner, F.; Stoltenhoff, T.; Kreye, H. Bonding Mechanism in Cold Gas Spraying. *Acta Mater.* **2003**, *51*, 4379–4394.
87. Hassani-Gangaraj, M.; Veysset, D.; Champagne, V.K.; Nelson, K.A.; Schuh, C.A. Adiabatic Shear Instability Is Not Necessary for Adhesion in Cold Spray. *Acta Mater.* **2018**, *158*, 430–439.
88. Owoseni, T.A.; Gupta, M.; Joshi, S.V.; Ingmar, M.; Varis, T. Wear and Corrosion of HVAF and HVOF-Sprayed WC-CoCr Coatings on Aluminum Alloy. *J. Therm. Spray Technol.* **2025**, *34*, 970–991.
89. MacLucas, T.; Schütz, S.; Suarez, S.; Müller, F.; Mücklich, F. Parametric Analysis of the Coating Thickness Development of Electrophoretically Deposited Carbon Nanotube Coatings. *Carbon Trends* **2023**, *11*, 100265.
90. German, R.M. *Sintering Theory and Practice*; John Wiley & Sons: Hoboken, NJ, USA, 1996.
91. German, R. Sintering: From Empirical Observations to Scientific Principles; Butterworth-Heinemann: Oxford, UK, 2014.
92. Kang, S.-J.L. *Sintering: Densification, Grain Growth and Microstructure*; Elsevier: Amsterdam, The Netherlands, 2004.
93. Atkinson, H.V.; Davies, S. Fundamental Aspects of Hot Isostatic Pressing: An Overview. *Metall. Mater. Trans. A* **2000**, *31*, 2981–3000.
94. German, R.M.; Suri, P.; Park, S.J. Liquid Phase Sintering. *J. Mater. Sci.* **2009**, *44*, 1–39.
95. Rybakov, K.I.; Olevsky, E.A.; Krikun, E. V Microwave Sintering: Fundamentals and Modeling. *J. Am. Ceram. Soc.* **2013**, *96*, 1003–1020.
96. Guillon, O.; Gonzalez-Julian, J.; Dargatz, B.; Kessel, T.; Schierning, G.; Räthel, J.; Herrmann, M. Field-assisted Sintering Technology/Spark Plasma Sintering: Mechanisms, Materials, and Technology Developments. *Adv. Eng. Mater.* **2014**, *16*, 830–849.
97. Canakci, A.; Varol, T.; Ertok, S. The Effect of Mechanical Alloying on Al_2O_3 Distribution and Properties of Al_2O_3 Particle Reinforced Al-MMCs. *Sci. Eng. Compos. Mater.* **2012**, *19*, 227–235.
98. Ramachandran, M.; Reddy, R.G. In-Situ Synthesis and Characterization of TiB 2 and Ti-Al-B Composites. In *Proceedings of the TMS 2014: 143rd Annual Meeting & Exhibition: Annual Meeting Supplemental Proceedings*; Springer: Berlin/Heidelberg, Germany, 2016; pp. 57–64.
99. Boesl, B.; Lahiri, D.; Behdad, S.; Agarwal, A. Direct Observation of Carbon Nanotube Induced Strengthening in Aluminum Composite via in Situ Tensile Tests. *Carbon* **2014**, *69*, 79–85.
100. Chen, B.; Li, S.; Imai, H.; Jia, L.; Umeda, J.; Takahashi, M.; Kondoh, K. Load Transfer Strengthening in Carbon Nanotubes Reinforced Metal Matrix Composites via In-Situ Tensile Tests. *Compos. Sci. Technol.* **2015**, *113*, 1–8.

101. Cançado, L.G.; Jorio, A.; Ferreira, E.H.; Stavale, F.; Achete, C.A.; Capaz, R.B.; de Moutinho, M.V.O.; Lombardo, A.; Kulmala, T.S.; Ferrari, A.C. Quantifying Defects in Graphene via Raman Spectroscopy at Different Excitation Energies. *Nano Lett.* **2011**, *11*, 3190–3196.
102. Williamson, G.K.; Hall, W.H. X-Ray Line Broadening from Filed Aluminium and Wolfram. *Acta Metall.* **1953**, *1*, 22–31.
103. Parker, W.J.; Jenkins, R.J.; Butler, C.P.; Abbott, G.L. Flash Method of Determining Thermal Diffusivity, Heat Capacity, and Thermal Conductivity. *J. Appl. Phys.* **1961**, *32*, 1679–1684.
104. Arsenault, R.J.; Shi, N. Dislocation Generation Due to Differences between the Coefficients of Thermal Expansion. *Mater. Sci. Eng.* **1986**, *81*, 175–187.
105. Vogelsang, M.; Arsenault, R.J.; Fisher, R.M. An in Situ HVEM Study of Dislocation Generation at Al/SiC Interfaces in Metal Matrix Composites. *Metall. Trans. A* **1986**, *17*, 379–389.
106. Monachon, C.; Weber, L. Thermal Boundary Conductance between Refractory Metal Carbides and Diamond. *Acta Mater.* **2014**, *73*, 337–346.
107. Trapp, J.; Semenov, A.; Eberhardt, O.; Nöthe, M.; Wallmersperger, T.; Kieback, B. Fundamental Principles of Spark Plasma Sintering of Metals: Part II–about the Existence or Non-Existence of the 'Spark Plasma Effect.' *Powder Metall.* **2020**, *63*, 312–328.
108. Yang, X.; Chen, W.; Yu, T.; Jiao, D.; Shao, H.; Elmarakbi, A.; Fu, Y. Thermal Conducting Mechanisms in Tungsten-Coated Diamond/Copper Composites. *Diam. Relat. Mater.* **2026**, *162*, 113287.
109. Kar, A.; Sharma, A.; Kumar, S. A Critical Review on Recent Advancements in Aluminium-Based Metal Matrix Composites. *Crystals* **2024**, *14*, 412.
110. Zhao, Q.; Liang, Y.; Zhang, Z.; Li, X.; Ren, L. Microstructure and Dry-Sliding Wear Behavior of B4C Ceramic Particulate Reinforced Al 5083 Matrix Composite. *Metals* **2016**, *6*, 227.
111. Macit, C.K.; Albayrak, M.G.; Tanyeri, B.; Gurgenc, T.; Ozel, C. Microstructure and Tribological Properties of Aluminum Matrix Composites Reinforced with ZnO–HBN Nanocomposite Particles. *Mater. Test.* **2024**, *66*, 1251–1266.
112. Bakshi, S.R.; Lahiri, D.; Agarwal, A. Carbon Nanotube Reinforced Metal Matrix Composites-a Review. *Int. Mater. Rev.* **2010**, *55*, 41–64.
113. Fang, B.; Li, J.; Zhao, N.; Shi, C.; Ma, L.; He, C.; He, F.; Liu, E. Boron Doping Effect on the Interface Interaction and Mechanical Properties of Graphene Reinforced Copper Matrix Composite. *Appl. Surf. Sci.* **2017**, *425*, 811–822.
114. Nix, W.D.; Gao, H. Indentation Size Effects in Crystalline Materials: A Law for Strain Gradient Plasticity. *J. Mech. Phys. Solids* **1998**, *46*, 411–425.
115. Archard, J. Contact and Rubbing of Flat Surfaces. *J. Appl. Phys.* **1953**, *24*, 981–988.
116. Prasai, D.; Tuberquia, J.C.; Harl, R.R.; Jennings, G.K.; Bolotin, K.I. Graphene: Corrosion-Inhibiting Coating. *ACS Nano* **2012**, *6*, 1102–1108.
117. Schriver, M.; Regan, W.; Gannett, W.J.; Zaniewski, A.M.; Crommie, M.F.; Zettl, A. Graphene as a Long-Term Metal Oxidation Barrier: Worse than Nothing. *ACS Nano* **2013**, *7*, 5763–5768.
118. Shchukin, D.G.; Zheludkevich, M.; Yasakau, K.; Lamaka, S.; Ferreira, M.G.S.; Möhwald, H. Layer-by-layer Assembled Nanocontainers for Self-healing Corrosion Protection. *Adv. Mater.* **2006**, *18*, 1672–1678.
119. Ward, L.; Agrawal, A.; Choudhary, A.; Wolverton, C. A General-Purpose Machine Learning Framework for Predicting Properties of Inorganic Materials. *npj Comput. Mater.* **2016**, *2*, 16028.
120. Dunn, A.; Wang, Q.; Ganose, A.; Dopp, D.; Jain, A. Benchmarking Materials Property Prediction Methods: The Matbench Test Set and Automatminer Reference Algorithm. *npj Comput. Mater.* **2020**, *6*, 138. Correction in *npj Comput. Mater.* **2020**, *6*, 159.
121. Wu, Y.-J.; Zhan, T.; Hou, Z.; Fang, L.; Xu, Y. Physical and Chemical Descriptors for Predicting Interfacial Thermal Resistance. *Sci. Data* **2020**, *7*, 36. Correction in *Sci. Data* **2020**, *7*, 61.
122. Xue, D.; Balachandran, P.V.; Hogden, J.; Theiler, J.; Xue, D.; Lookman, T. Accelerated Search for Materials with Targeted Properties by Adaptive Design. *Nat. Commun.* **2016**, *7*, 11241.
123. Raccuglia, P.; Elbert, K.C.; Adler, P.D.F.; Falk, C.; Wenny, M.B.; Mollo, A.; Zeller, M.; Friedler, S.A.; Schrier, J.; Norquist, A.J. Machine-Learning-Assisted Materials Discovery Using Failed Experiments. *Nature* **2016**, *533*, 73–76.
124. Santiago-Herrera, M.; Ibáñez, J.; De Pamphilis, M.; Alegre, J.M.; Tamayo-Ramos, J.A.; Martel-Martín, S.; Barros, R. Comparative Life Cycle Assessment and Cost Analysis of the Production of Ti6Al4V-TiC Metal–Matrix Composite Powder by High-Energy Ball Milling and Ti6Al4V Powder by Gas Atomization. *Sustainability* **2023**, *15*, 6649.

Disclaimer/Publisher's Note: The statements, opinions and data contained in all publications are solely those of the individual author(s) and contributor(s) and not of MDPI and/or the editor(s). MDPI and/or the editor(s) disclaim responsibility for any injury to people or property resulting from any ideas, methods, instructions or products referred to in the content.

https://doi.org/10.3390/inorganics14120303